UCT SHARC Buoy V3.0: Waves-in-ice measurement in the Antarctic MIZ

Inertial Measurement of waves-in-ice phenomena for the Targeted Observational Experiment with cost effective devices

Michael Noyce

Department of Electrical Engineering
University of Cape Town
Rondebosch, Cape Town
South Africa

Supervisor:
R. A. Verrinder

Co-supervisor:
Prof. M. Vichi

October 2023

MSc.(Eng.) thesis submitted in partial fulfilment of the requirements for the degree of MSc in Electrical Engineering Specialising in Electrical Engineering in the Department of Electrical Engineering at the University of Cape Town

Keywords: Marginal Ice Zone, waves-in-ice, sea ice, Antarctic, in-situ sensing

Declaration

I, Michael Noyce, hereby:

1. grant the University of Cape Town free licence to reproduce the above thesis in whole or in part, for the purpose of research;

2. declare that:

   (a) this thesis is my own unaided work, both in concept and execution, and apart from the normal guidance from my supervisor, I have received no assistance except as stated below:

   (b) neither the substance nor any part of the above thesis has been submitted in the past, or is being, or is to be submitted for a degree at this University or at any other university, except as stated below.

   (c) I know the meaning of plagiarism and declare that all the work in the document, save for that which is properly acknowledged, is my own. This thesis/dissertation has been submitted to the Turnitin module (or equivalent similarity and originality checking software) and I confirm that my supervisor has seen my report and any concerns revealed by such have been resolved with my supervisor.

Signed by candidate

Michael Noyce

Department of Electrical Engineering
University of Cape Town

Tuesday 24th October, 2023

Abstract

UCT SHARC Buoy V3.0: Waves-in-ice measurement in the Antarctic MIZ

Michael Noyce

Tuesday 24th October, 2023

The Antarctic Marginal Ice Zone is an area of key scientific interest as the climatic processes in the region affect the global climate. Sea ice in particular has been difficult to model due to its high variability, as a result there is a pressing need to collect in situ data to further develop and validate models of the annual and seasonal sea ice cycles. The UCT SHARC Buoy has been developed to collect and measure in situ wave data that characterises the interaction between ocean waves and sea ice. It aims to do this accurately and with a platform that is cost-effective enough to deploy at scale. To achieve this, the use of low-cost inertial measurement units (IMUs) to measure wave activity on a mock ice floe was validated in a controlled wave tank setting. Following this, the existing SHARC Buoy instrument was upgraded to collect and process high-frequency IMU data and tested for reliability. Finally, the devices were deployed and collected on the SCALE Winter Cruise 2022. The time series were analysed to verify that the instrument's measurements and local calculation of wave parameters were accurate. Several inertial phenomena were noted in the inertial time series and characterised, specifically the collisions between ice floes which are of importance in the region.

Acknowledgements

The work on the SHARC Buoy project has included many people, without whom this project would not have been possible. Thanks are given to the following people:

Firstly, to my supervisor Robyn Verrinder, whose guidance during the course of the project has been invaluable. In addition to the development of the updated PCB designs used on the buoy and the selection of the updated batteries for the buoy. Finally, for the enormous task of organising the logistics for the Sea Ice Observation group for the SCALE Winter Cruise 2022.

Prof. Marcello Vichi, for providing scientific input to the wave measurement and deployment pattern of the buoys. Additionally, for leading the SCALE Winter Cruise expedition 2022, making the deployment and retrieval of the buoys possible.

Lawrence Stanton, for being in the trenches with me during the final deployment period, debugging, assembling the PCBs, and developing the updated GPS driver for the buoy. The deployments would not have been successful without your help.

To Agoritsa Spirakis for providing the fantastic photography and stereo-photography data for use in analysing the deployments of the buoys and discussions about papers and sea ice.

To Jamie Jacobson, for developing the SHARC Buoy V2.0 which was used as the basis for the SHARC V3.0. It was a fantastic opportunity to contribute to the project.

To James Hepworth for designing the updated stand and enclosures for the SHARC Buoy which allowed it to survive the extreme conditions.

To Justin Pead for developing the updated power supply board for the buoy.

To Carl Wehlitz at the CSIR Coastal and Hydraulics Laboratory for the assistance in testing the IMU's used aboard the SHARC Buoy.

To Prof Amit Mishra, Jarryd Son and Marcello Vichi for kicking of the project with the SHARC Buoy V1.0.

To the people who were brave enough to stand on a basket over sea ice to deploy and retrieve the devices: Justin Pead, Robyn Verrinder, Jan-Victor Björkqvist, Safiyyah Moos, Agoritsa Spirakis, Lawrence Stanton and Jacques Welgemoed.

To the members of the African Robotics Unit (ARU) lab who made long days (and nights) much more tolerable in the lab. Thanks to Mike, Agi, Daryn, Chris, Amaan and Matt.

To my partner, Lisa van Dyk for the love and support for the during the project, especially during the difficult parts of the project. Also, for listening to me talk at length about sea ice.

To my sister, Olivia providing love and support and putting up with a secondary laboratory in the apartment.

Special thanks parents Lucinda and Simon, for supporting me through the project. I am grateful for your love and support during my university career.

The financial assistance of the National Research Foundation (NRF) towards this research is hereby acknowledged. Opinions expressed and conclusions arrived at, are those of the author and are not necessarily to be attributed to the NRF.

Figure 1: UCT Team Buoys SCALE Winter Cruise 2022. Left to right: Agoritsa Spirakis, Michael Noyce (Author), Robyn Verrinder, Lawrence Stanton. Image credit: Kurt Martin

Contents

List of Figures

List of Tables

Glossary

DSP Digital Signal Processing

FFT Fast Fourier Transform

FMI Finnish Meteorlogical Institute

GNSS Global Navigation Satellite System

I2C Inter-Integrated Circuit

IMU Inertial Measurement Unit

MCU Microcontroller Unit

MEMS Microelectromechanical system

MIZ Marginal Ice Zone

ROA Response Amplitude Operator

SBxx SHARC Buoy XX eg. SB01

SCALE Southern oCean seAsonaL Experiment

SCALE Southern OCean SeAsonaL Experiment

SD Secure Digital

SDIO Secure Digital Input Output

SDS Scientfic Data System

SHARC Southern Hemisphere Antarctic Research Collaborative

SIE Sea Ice Extent

TOE Targetted Observational Experiment

TRL Technology Readiness Level

UART Universal asynchronous receiver-transmitter

Chapter 1

Introduction

1.1 Project background and motivation

1.1.1 Brief history of Antarctic sea ice research

The Antarctic Continent is one of stark beauty and interest. It has been studied scientifically since at least 1839 for Ross's geomagnetic survey of the region using the polar vessels *Erebus* and *Terror* (Fogg 2000). However, its remoteness has made comprehensive study of the region difficult and expensive (Kennicutt et al. 2016). This can be contrasted with the importance the region has on global climate, as a key regulator of global climate and local variations have global impacts - such as reducing the Earth's albedo and increasing the absorption of heat (Barnes 2015).

The ubiquity of the sea ice around the continent likely contributed to the sparseness of scientific study of the region until the recent past. However innocuous sea ice coverage may appear - its importance becomes clear when it is ignored, crushing exploration and scientific vessels such as the *Endurance* captained by Sir Ernest Shackleton in 1915 (Thomas & Dieckmann 2003), emphasising the need to understand the properties - if for no other reason than the safety of seafaring in the region.

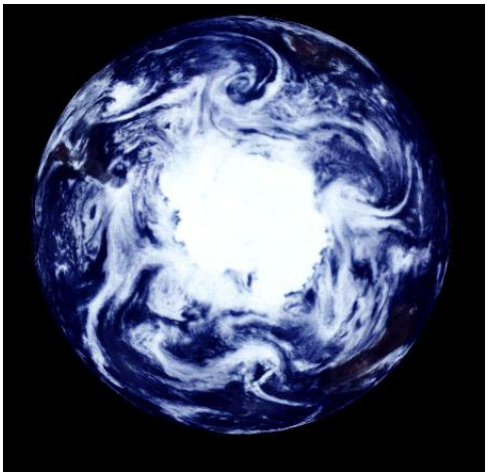

Figure 1.1: Image of the Antarctic continent from space surrounded by weather systems, highlighting the intensity of the weather around the continent. Image credit: NASA Jet Propulsion Laboratory (NASA Jet Propulsion Laboratory 1997)

Serious study of Antarctic sea ice began towards the end of the 19th century - during the so-called *Heroic Era of Polar Exploration*. Research outputs from the period included the classic book on ice: Glaciology (Wright & Priestley 1922). Since then, sea ice research has picked up significantly, as a result of increased scientific interest and technological development (Thomas & Dieckmann 2003). In addition, modern sea ice research has been driven by the concerns of the effects of anthropogenic warming of the region (Ludescher et al. 2019).

1.1.2 The Antarctic Marginal Ice Zone (MIZ)

The Antarctic Marginal Ice Zone (MIZ) is a dynamic transitional region of ice cover between multi-year sea ice and open ocean. It is traditionally defined as the region in which sea ice concentration varies between 15-80% (Strong et al. 2017) A more informal definition is the region of ice which is close enough to the ocean to be strongly influenced by its activity (Wadhams 1986). However, the definition of the MIZ is currently an area of contention with more robust definitions being proposed (Vichi 2022).

Over the course of the last few years, intense scientific interest has been developed around the phenomena and processes in the MIZ (Squire 2020). The MIZ could be viewed as the canary in the coal mine, it is a highly dynamic system whose processes influence key measures such as the sea ice extent (SIE) (Kohout et al. 2014).

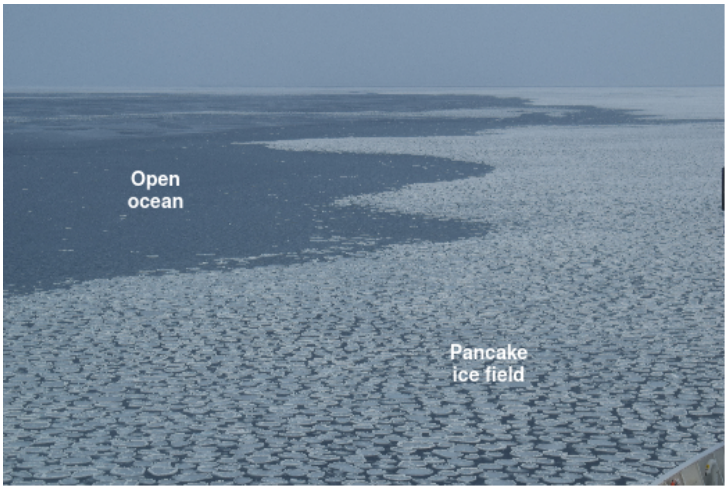

Figure 1.2: Photograph showing the edge of Marginal Ice Zone. Open ocean is giving way to pancake ice which will eventually give way to more consolidated ice. Image credit: Marcello Vichi

1.1.3 Waves-in-ice

One particular geophysical problem has been investigated in the polar regions since at least 1887 (Greenhill 1887) - the problem of waves propagating through ice. Complex models began to be developed in the 1950s and 60s such as the models of Evans & Davies (1968).

Figure 1.3: Waves-in-ice propagating through the outer region of the MIZ during the retrieval of SHARC Buoy SB01 (in foreground) in the SCALE Cruise 2022. Photo credit: Nicole Taylor

Waves-in-ice are of particular importance as they are a key driver of the mechanical breakup of ice. Massom et al. (2018), have shown that the MIZ acts as a protective buffer to ice shelves, which otherwise calve off due to the flexure caused by ocean waves.

In the late 1970s and 1980s, Wadhams et al. (1988) began the first experimental investigation of ocean waves in polar sea ice, using accelerometers to determine the attenuation of waves in Arctic sea ice in the Greenland and Bering Sea's. Insights from these models were also used to model Antarctic waves-in-ice and the resulting breakup of landfast ice (Crocker & Wadhams 1989).

Of particular interest in these investigations was that this marked an early use of in situ field measurements of wave activity to parameterise the waves-in-ice models of the polar region.

The key problem for modelling waves-in-ice phenomena is determining the parameters of the models. These parameters are determined by in situ field measurements such as the experiments of Wadhams et al. (1987). Key parameters of a waves-in-ice model generally include: attenuation of significant wave height as the waves propagate through ice, advection of waves onto ice and the breakage of ice by waves (Williams et al. 2013).

Despite decades of research, waves-in-ice has proved to be a difficult problem in many respects as the MIZ is heterogeneous and current parameterisations for wave forecasting (such as Wave Watch III) are not satisfactory in the Antarctic (Squire 2020).

A further problem is the stark difference between the behaviour of Arctic and Antarctic sea ice (Maksym et al. 2012, Serreze & Meier 2019). The primary driver of this difference is the exposure of the Antarctic sea ice to high energy wind and wave fields which is not the case in the Arctic, due to its protection by the surrounding land (Maksym et al. 2012). Thus, a different approach to data collection and modelling is needed for the different regions.

The general consensus is that empirical models based on field data may be a viable solution to this otherwise intractable problem (Squire 2020, Meylan et al. 2014, Ardhuin et al. 2017).

1.1.4 Overview of the Role of Technology

Technology, particularly in situ and remote sensing, has been identified as a primary vehicle through which science in the region will continue to develop (Kennicutt et al. 2015). Kennicutt et al. (2015) developed an "Antarctic Roadmap for 21st-century science" for the Scientific Committee for Antarctic Research (SCAR) and have identified that buoy networks (including open ocean buoy and ice tethered buoy networks) are key to collecting "big datasets" to answer geophysical questions in the region.

This approach has proven to be highly effective in capturing the large-scale variability in the Arctic. The Marginal Ice Zone (Lee et al. 2012) and Sea State (Thomson et al. 2018) missions used extensive autonomous Lagrangian (ice-tethered) platforms (Doble et al. 2017) to collect the large datasets needed for real-time forecasting in the Arctic (Lee & Thomson 2017). A similar approach is being implemented in the Antarctic through the Seasonal Climate observAtionaL Experiments (SCALE). However, there is much room for growth as data paucity is still a significant limitation, especially when compared to the Arctic (Maksym et al. 2012).

1.1.5 Contemporary Waves-In-Ice Research

Interest in the Antarctic MIZ increased in 2014, when Kohout et al. (2014) released their findings that waves propagated far further into the MIZ than previously thought - in some cases penetrating hundreds of kilometres into the ice (Kohout et al. 2014). Further, these waves were causing breakages in the ice even at these advanced distances due to ice flexure. This changed the understanding of the Antarctic MIZ and has resulted in research to re-parameterise exisiting waves-in-ice models (Mosig et al. 2015). These models had remained largely similar to the models first developed in the pioneering research by Wadhams in the 1980s (Wadhams 1986, Wadhams et al. 1987, 1988). These models assumed exponential attenuation of all waves - given the findings of Kohout et al. (2014) this appears to only hold for waves in the high-frequency regime whilst waves in the low-frequency regimes attenuate at slower rates.

After the release of a paper by Kohout et al. (2014) in 2014 there has been an increase in the

number of waves-in-ice instruments, due to improvements in the microprocessors (MCUs) and the inertial measurement units (IMUs) used in these instruments as well as their relative cost. These are devices that aim to collect in situ measurements of wave activity in the MIZ. The first of the new generation of these devices was the device used by Kohout et al. (2014), the Waves-in-Ice-Observation System or WIIOS. The WIIOS was designed to collect wave measurements to calculate attenuation in deployments of multiple buoys (Kohout et al. 2015).

A fundamental problem in Antarctic research is the paucity of data available to use as a reference for climate models. For example, the WAM model was updated for waves-in-ice modelling with the data from a single buoy (Doble & Bidlot 2013). Further, as missions to the MIZ in winter have, until very recently, been rare or non-existent - data collected does not necessarily represent the behaviour of the zone across seasonal variation (if such seasonal variation exists - with the lack of current data it is hard to tell). This data can be collected *in situ* or remotely (generally via satellite). However, in situ sensing has the potential to produce higher fidelity data.

This led to the next generation of buoys built using low-cost commercially available components. An example of such a buoy was Rabault et al. (2020)'s Waves-In-Ice-Buoy (Rabault et al. 2020). The WIIB indicated a fundamental shift in the economics of polar measurement. For the first time, low-cost commercial components such as microcontrollers and sensors had become accurate enough and reliable enough to deploy in the MIZ for scientific measurement. Waves-in-ice measurements for the WIIB were successfully retrieved for deployments in the Arctic and compared to models of the region.

The importance of the MIZ was highlighted by events in the Weddell Sea in 2017. The SIE reduced dramatically after increasing in extent for the previous 40 years - since records began (Turner et al. 2020). The decrease was not predicted by climate models, indicating gaps in the understanding of waves-in-ice coupled models and sea ice physics (Stopa et al. 2018).

Additionally, the wave climate in the Arctic is becoming more similar to the Antarctic as lower sea ice extents in the region result in larger wave fetches, which are present in the Southern Ocean (Maksym 2019). This result in larger waves and more ice fracture. The increasing similarity makes data from the Antarctic of even greater interest.

Thus, there is a pressing need to collect in situ data - particularly in situ waves-in-ice data of the Antarctic to anticipate how the climate is changing in the region.

1.1.6 The University of Cape Town's Southern Hemisphere Antarctic Research Collaborative (SHARC) Buoy Program

The University of Cape Town's SHARC Buoy project was initiated in 2018. It aimed to be a modular multi-sensor system capable of measuring a variety of environmental processes. These included temperature, pressure, location, acceleration and orientation. The overall goal was to develop a platform that was capable of collecting in situ data to parameterise and validate climate models of the region - specifically models of the MIZ. Additionally, it was considered desirable for the device to be developed on the African continent.

1.2 Problem Identification

The SHARC Buoy platform was initially developed to measure waves-in-ice phenomena. However, development of a reliable in situ sensing system for use in an extreme environment poses a range of difficulties from both a hardware and software point of view.

These difficulties include but are not limited to:

- The inability to access the device once deployed
- Failure of components due to the extreme conditions
- Unexpected behaviour of the device due to unplanned modes of failure
- Accurate measurement in extreme conditions
- Transmission of large datasets via satellite link
- Onboard processing of large datasets using limited computational resources
- Use of non-renewable power supplies for extended periods in extreme cold

These difficulties have resulted in the development of multiple iterations of the SHARC Buoy. A brief overview of each version is provided in table 1.1.

Given the previous development of the SHARC Buoy system, V3.0 aimed to be the first buoy to collect in situ waves-in-ice data in a large deployment. This was made possible by the previous development of the system.

Up to V3.0 the system did not have the ability to either collect high-frequency IMU data reliably, nor process the data locally to produce summary wave statistics to send via satellite link.

Thus, V3.0 sought to convert the SHARC Buoy to a full waves-in-ice instrument, capable of collecting data for scientific research.

Table 1.1: Overview of SHARC Buoy versions up to V3.0

Version	Year	Description
1.0	2018	Initial prototype proposed by Prof Amit Mishra, Jarryd Son and Marcello Vichi. Envisioned as a multi-sensor platform.
1.1	2019	First prototype developed by Robyn Verrinder, Jamie Jacobson and Justin Pead. Ice-drift and environmental sensor platform.
1.1	2019	First version tested on the SCALE cruise 2019. 2 units deployed. 1 lasted for ∼1 hour.
2.0 (1.2)	2019	Second prototype developed by Robyn Verrinder, Jamie Jacobson and Justin Pead. Integrated IMU (MPU6050) as proof of concept.
2.0	2021	Second version deployed on the SANAE summer relief mission and from the RV Polarstern. Deployment lasted ∼1 week.
3.0	2022	Third prototype developed by Robyn Verrinder, Michael Noyce, Lawrence Stanton and Justin Pead. Integrated waves-in-ice measurement and high-frequency local storage.
3.0	2022	Third version deployed on SCALE winter cruise 2022. 6 units deployed. 4 function as waves-in-ice devices, 2 as ice-drift devices.

Figure 1.4: SHARC Buoy Versions shown during the various deployments. From left to right, SHARC Buoy V1.0 deployed on deck before final deployment during the SCALE winter cruise 2019, V2.0 deployed during the summer 2020-2021 Polarstern expedition in the Weddell Sea and V3.0 immediately after a basket deployment during the SCALE winter cruise 2022.

1.3 Project Objectives

The objectives of the project were as follows:

1. To upgrade the hardware and firmware of the SHARC Buoy to store and process high-frequency wave IMU data
2. The development of a program to extract wave summary statistics in situ to reduce the size of Iridium data transmissions
3. The validation of the system measurements of waves-in-ice phenomena using both field measurements and wave tank testing

1.4 Project Scope and Limitations

The primary aim of the project was to upgrade the existing hardware and firmware to collect waves-in-ice inertial data and to validate the collected data. Previous hardware choices and firmware development was used to the extent possible with updates being made to overcome previous issues.

The use of low-cost commercial hardware and inertial measurement units was made intentionally so that the platform could be cost-effective in the Global South and deployed at scale. However, this means that the data collected required processing and validation to make sure that the system functioned as intended.

To determine the status of the SHARC Buoy as a useful waves-in-ice instrument, as opposed to a prototype, technology readiness levels can be used (Mankins 1995) (using the NASA definition and replacing 'space' environment/conditions with Antarctic MIZ environment/conditions). The goal is to deploy at a technology readiness level (TRL) of 5 - 6 ("System prototype demonstration in an laboratory environment" - "Technology demonstrated in relevant environment" through test and demonstration"). Following deployment, and using the data and testing from the cruise, a TRL of 7 ("Technology demonstrated in "*Antarctic MIZ* environment") constituted the final objective.

This thesis outlines the development, testing and validation of these updates and the data collected on the SCALE cruise 2022. It does not outline further development of the underlying firmware after the SCALE cruise. Additionally, it does include updates to the wave parameter extraction algorithm after the cruise. Analysis of the data collected is done to the extent that it validates the measurement of waves-in-ice phenomena.

The phenomena of interest are:

1. Wave frequency spectra derived from the inertial time series measured from the oscillation of the ice floe (on which the device is deployed) under wave forcing
2. The collision/rafting of ice floes identified in the time series
3. The attenuation of wave activity at specific frequencies measured by comparing the wave spectra at different locations, combined with knowledge of the location of different devices over the deployment duration.

The wave spectra are calculated for the uni-dimensional case. The directional spectra for the three-dimensional case are not calculated. This is due to the limitations in determining heading using commercial components close to the polar regions where magnetic interference is significant. Additionally, where possible, a small angle assumption is used to determine the wave height as this reduces error caused by the introduction of noise from several degrees of freedom on an inertial measurement device.

1.5 Plan of development

The project followed the following stages:

1. The analysis of the V2.0 platform and identifying the important areas of development. Waves-in-ice measurement was selected as the key area of improvement.
2. Wave tank testing with inertial measurement units to collect wave data to use to develop a measurement and storage system as well as a spectral analysis algorithm
3. The integration of wave measurement into the SHARC Buoy platform, including the update of the hardware and firmware of the system (V3.0).
4. The deployment of the system on the SCALE 2022 cruise for the collection of raw data to validate the instrument in the field
5. The analysis of the collected data to validate the instrument
6. Updating the final firmware for the handover of the project.

1.6 State of the Art

The SHARC V3.0 is state of the art in two key respects. Firstly, cost-effective waves-in-ice devices are a new development, with several prototypes and early commercial versions starting with the Waves-in-ice Buoy (Rabault et al. 2019). These instruments are extremely new to polar research and especially Antarctic MIZ research and so can be easily considered state of the art.

Secondly, the SHARC V3.0 was the first waves-in-ice device to be retrieved from the Antarctic MIZ with high-frequency inertial time series, allowing for novel analysis of the data to determine the reliability of the summary statistics that most devices transmit. In addition, it allows for the

analysis of high frequency phenomena of interest that have been observed but rarely measured for extended time periods such as the collision of ice floes.

1.7 Overview of thesis

Table 1.2: Thesis outline.

Chapter	Name	Overview
1	Introduction	An outline of the importance of the waves-in-ice research problem and how in situ sensing is an important approach to resolving several key scientific questions
2	Literature Review	Introduce the scientific and engineering background to the waves-in-ice measurement. Specific focus given to the hydrodynamics, waves-in-ice phenomena and the measurement of these phenomena. Issues relating to the design of polar instruments are discussed.
3	Waves-in-ice Measurement	A description of the approach used to measure waves-in-ice. Specific focus is given to potential sources of bias and the necessary corrections
4	Methodology	An overview of approach taken to update the SHARC Buoy for the SCALE cruise 2022.
5	Hardware Development	An overview of the hardware changes made for the SHARC Buoy for the SCALE cruise 2022.
6	Firmware Development	An overview of the firmware updates made for the SHARC Buoy V3.0 in preparation for the 2022 SCALE cruise.
7	Testing	The overview of the testing procedures used to validate the system prior to deployment.
8	Deployment	A description of the deployment during the SCALE cruise. The approach to deployment, the configuration of the instruments and the data collected.
9	Result and Discussion	The results collected from the SCALE cruise are discussed, with a particular focus on waves-in-ice but also including temperature and pressure and location data.
10	Conclusion	The SHARC Buoy V3.0 is evaluated as a platform and the findings in the 2022 SCALE data are highlighted.
11	Recommendations	Suggestions for further improvements to the SHARC Buoy platform to improve the reliability and longevity of the device in the field as well as the quality of data collected

Chapter 2

Literature Review

2.1 Ocean dynamics

The SHARC Buoy aims to measure waves-in-ice as an ice-tethered instrument. It uses the movement of the ice as a proxy measurement for the wave activity in Marginal Ice Zone. An overview of how the underlying ocean dynamics are characterised and measured is thus necessary. Firstly, how the ocean is modelled statistically with the random-phase amplitude model is given. Secondly, a description of the linear wave theory on which this statistical model is based is provided. A brief discussion of the dispersion relation in the ocean, which allows the distribution of waves in time and space to be related, is done as this relation is used later for wave tank testing. Thirdly, a discussion on the power spectral density (PSD) and how it is related to the wave spectrum is given along with the method used for calculation.

2.1.1 Random Phase - Amplitude Model

Ocean waves are measured using statistical models which describe the relationship between wave frequency and the random surface elevation of the ocean surface. Waves can be described mathematically as the superposition of a series of sinusoidal harmonics (Falnes 2002, Holthuijsen 2007).

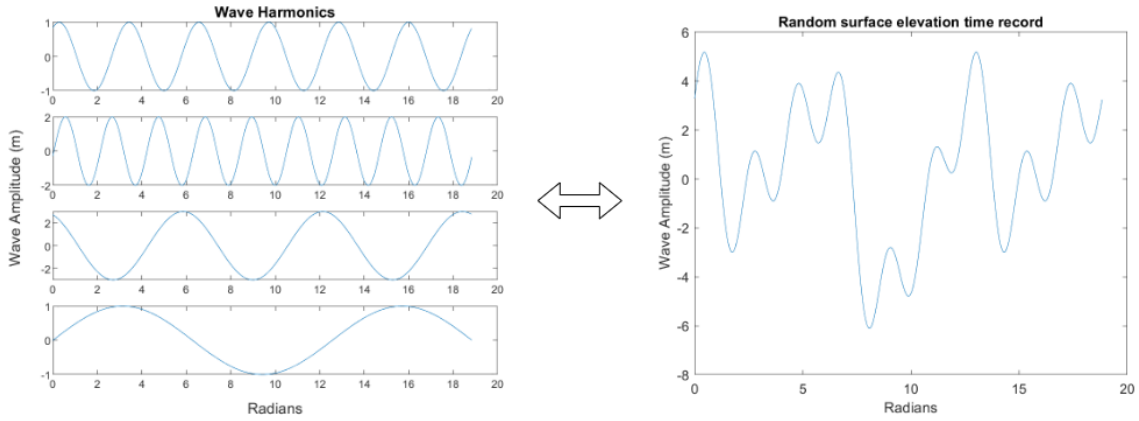

Figure 2.1: The surface elevation at any given instant is the result of the superposition of sinusoidal harmonics according to linear wave theory.

The dominant model used to describe wave activity is the random phase amplitude model. This model treats the surface elevation as a stationary stochastic (random) process (Holthuijsen 2007).

The following assumptions are necessary for the random phase amplitude model.

1. Stationarity (Gaussian process): The process is time-invariant. This implies that the mean and variance of the time series do not change. This assumption is approximately true over time series between 15 - 30 minutes.

2. Random phase: The phase of deep water ocean waves has a uniform probability distribution between 0 and 2π.

3. Independence of wave components: Wave components present at different frequencies are assumed to vary independently and is a consequence of the random-phase assumption. This is approximately true in deep water and for waves that are not steep.

Variance is used as a useful statistical measurement (the sum of variances at all frequencies is equal to the random surface elevation). Additionally, research has shown that the energy in waves is proportional to their variance (Holthuijsen 2007).

The surface elevation can thus be described as:

$$E(f) = \lim_{\Delta f \to 0} \frac{1}{\Delta f} E\{\frac{1}{2}\underline{a}^2\} \tag{2.1}$$

Where f is the wave frequency, $E(f)$ is the expectation function for the amplitude variance density (variance divided by frequency interval Δf), $\underline{a}$ is the random variable amplitude, $\frac{1}{2}\underline{a}^2$ is the variance of the amplitude. The unit of the wave spectrum are $m^2 s$ or alternatively $m^2 Hz^{-1)}$.

This results in a wave spectrum, which plots the distribution of the variance of the amplitude as a function of frequency. A wave spectrum from SHARC Buoy SB06 is shown below as a reference along with the amplitude time series.

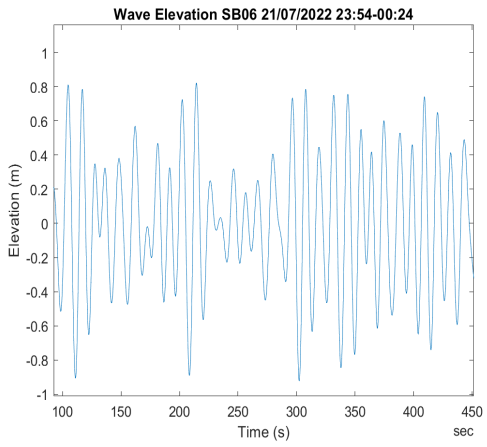

(a) A time series of the amplitude for SB06.

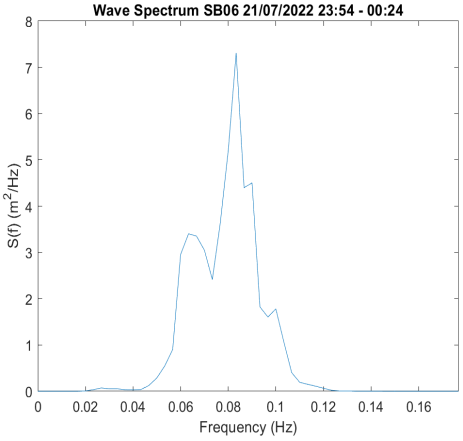

(b) The power/wave spectral density calculated from the amplitude time series from SB06.

Figure 2.2: Wave spectrum from the time series collected in the MIZ during the winter SCALE cruise 2022. Note the 12.5 s dominant period which is typical of the waves in the zone.

2.1.2 Linear Wave Theory

The random phase - amplitude model is based on linear wave theory. Linear waves imply that waves of different frequencies do not interact with one another.

Linear Wave Theory is based on the following assumptions:

1. Fluid is incompressible
2. Fluid has constant density
3. Fluid is a continuous body
4. Gravity is the only force acting on the system

Given these assumptions, particles on the wave follow an orbital motion, as shown in figure 2.3 .

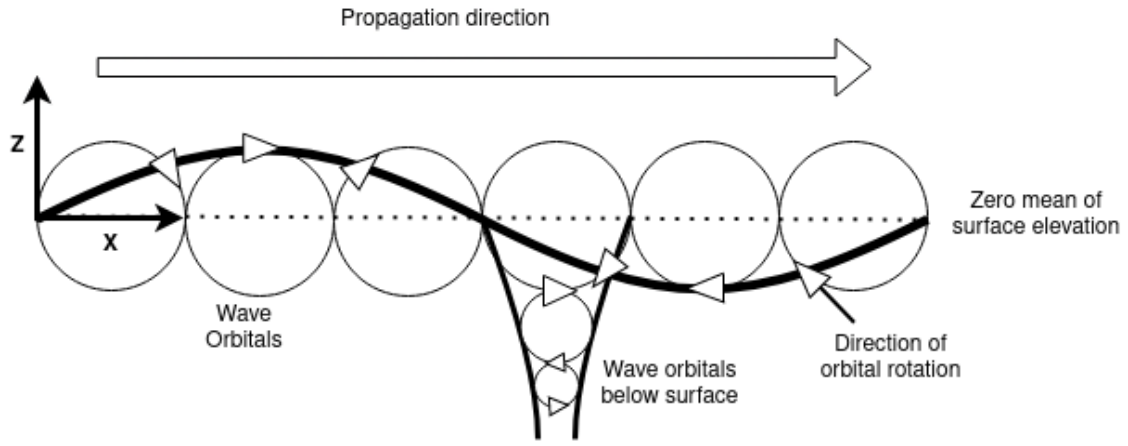

Figure 2.3: A result of linear wave theory is that waves have an orbital motion.

If the water is too shallow then the orbital paths shown in figure 2.3 are deformed. Linear wave theory is only approximately applicable for certain depths and wave steepness. The applicability of linear theory can be determined using the Ursell number (N_{Ursell}), which is a measure of the non-linearity of a wave.

$$N_{Ursell} = \frac{\text{steepness}}{(\text{relative depth})^3} = \frac{H/L}{(d/L)^3}, \tag{2.2}$$

where the steepness is given by the waveheight, H, divided by the wavelength, L, and the relative depth is given by the depth, d, divided by the wavelength cubed.

Linear Wave Theory or a Stokes correction of linear wave theory is applicable for $N_{Ursell} \leq 10$.

For deep water, wave steepness (H/L) alone must also be considered as it can indicate the applicability of linear wave theory. When the non-linear effects become sufficiently large, a Stokes correction must be used. For wave tank testing, N_{Ursell} is used as the maximum depth is shallow and an approximation of deep water is desired as these are the conditions of deployment in the Southern Ocean for the instrument. Finally, steep waves are not expected for instruments deployed sufficiently far into the sea ice (Toffoli et al. 2015).

2.1.3 The dispersion relation in deep water

Different frequency components of waves disperse as they propagate out from the area of generation (Holthuijsen 2007). Longer wavelengths (low frequencies) travel faster than shorter wavelengths (high frequencies) resulting in the disparity. This is known as dispersion. The dispersion

relationship in ocean gravity waves is given by the equation:

$$\omega^2 = gk\tanh(kd) \tag{2.3}$$

Where ω is the frequency, k is the wavenumber, a measure of the spatial distribution of waves, d is the depth and g is gravitational acceleration. In sufficiently deep water, $kd \to \infty$ and so $\tanh(kd) \to 1$ which results in:

$$\omega = \sqrt{gk} \tag{2.4}$$

This provides a relationship between the distribution of the waves temporally and spatially (Newman 1977) and so can be used to iteratively calculate the wave number given the depth and frequency.

This use of this relation is necessary for designing experiments in a wave tank setting - especially for floating bodies. The interaction between waves and floating bodies will be reviewed in section 2.2.

2.1.4 Power Spectral Density (PSD)

The wave spectrum and PSD

The wave spectrum can be defined in terms of wave variance (as discussed in section 2.1.1). An alternate approach is to describe waves in terms of signal processing theory.

The energy of a signal, $y(t)$ (wave amplitude in this case) is defined as:

$$E = \int_{-\infty}^{\infty} |y(t)|^2 \, dt \tag{2.5}$$

Using Parseval's theorem (roughly that the energy in the time domain of a signal is equal to the energy in the spectral domain) the energy in the time and frequency domain's can be related as:

$$\int_{-\infty}^{\infty} |y(t)|^2 \, dt = \int_{-\infty}^{\infty} |Y(f)|^2 \, df \tag{2.6}$$

Finally, the definition of signal energy requires that the energy is bounded, this is not the case for waves which are measured as a stationary stochastic process (i.e. have unbounded energy) (Topper 2013). Thus, the signal power is calculated. Using the Wiener-Khinchin relation the PSD is defined as the Fourier transform of the autocorrelation function. For an ergodic process the autocorrelation function (ϕ_{yy}) can be estimated as $\hat{\phi_{yy}} = \frac{1}{T}\int_{-\frac{T}{2}}^{\frac{T}{2}} y(t)y(t-\tau)\,d\tau$ where $\hat{\phi_{yy}} \to \phi_{yy}$ as $T \to \infty$. Thus, the PSD estimate, $\hat{P}$ can be defined:

$$\hat{P}(f) = \frac{1}{T}\int_{-\frac{T}{2}}^{\frac{T}{2}} \hat{\phi}_{yy} e^{i2\pi f\tau} \, d\tau \tag{2.7}$$

This can be further simplified to:

$$\hat{P}(f) = \frac{1}{T}|Y(f)|^2 \tag{2.8}$$

This is known as the periodogram estimator which is discussed in the next section for the discrete case.

Periodogram estimator

Practically, the spectrum is calculated from a discrete time series of measurements. The generally preferred method for PSD estimation for wave measurement being a variation of the *periodogram method* (Thomson & William, 2014) discussed below.

The two-sided periodogram estimate of the PSD of a signal y, $\hat{P}_{yy}$ of length N with K zero padding is given by:

$$\hat{P}_{yy} = \frac{1}{(N+K)\Delta t}|Y_k|^2 \tag{2.9}$$

Where Y_k is the Discrete Fourier Transform (DFT) of signal $y(t)$.

Note that the division by the sample period Δt turns the energy spectrum into a power spectrum.

Given that the random surface elevation time series is real-valued, the power spectrum is symmetrical and so a single-sided PSD estimate is given by:

$$PSD(f) = 2 * \hat{P}_{yy} = \frac{2}{(N+K)\Delta t}|Y_k|^2 \tag{2.10}$$

Where $\hat{P}_{yy}$ is the single sided periodogram estimate of a real valued time series. The SI units of $PSD(f)$ are $m^2 s$, the same as the wave spectrum $E(f)$ (equation 2.1). Thus, with proper scaling: $PSD(f) \equiv E(f)$.

The Welch Method

The periodogram method has several limitations. The limitations are caused by the truncation of the measured signal and a limited sampling frequency. The key limitation is the variance of the periodogram estimate. Unfortunately, this variance does not reduce by taking the periodogram of a longer time series. In fact the variance of the periodogram estimate of the PSD is approximately equal to the square of the variance of the true PSD, regardless of the length of the original truncated time series. This reduces the reliability of the PSD estimate.

Fortunately, the variance of the signal can be reduced by averaging several periodograms of a time series at the cost of spectral resolution (Bartlett's Method). It can be further reduced with windowing by a smooth window function (reducing spectral leakage) of each periodogram and by overlapping these periodograms to increase the number of periodograms taken of a time series (Welch's method). Note that windowing a signal reduces the power contained in the periodogram estimate. Thus a compensating factor should be used.

Welch's method can be represented as (Welch, 1967):

$$\hat{P}(f) = \frac{1}{K}\sum_{k=1}^{k} I_k(f_n) \tag{2.11}$$

Where I_k is the k^{th} modified periodogram estimate given by:

$$I_k(f_n) = \frac{L}{U}|A_k(n)|^2 \tag{2.12}$$

Where $A_k(n)$ is a FFT of the k_{th} windowed data segment, X_k of length L given by:

$$A_k(n) = \frac{1}{L}\sum_{j=0}^{L-1} X_k(j)W(j)e^{-2kijn/L} \tag{2.13}$$

And U is a normalisation factor for power given by:

$$U = \frac{1}{L}\sum_{j=0}^{L-1} W^2(j) \tag{2.14}$$

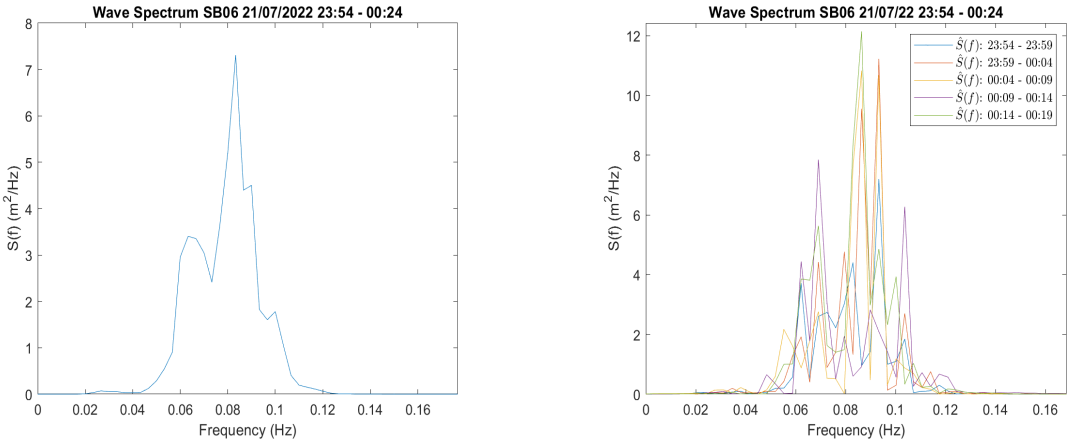

(a) Welch method estimate

(b) Periodogram estimates

Figure 2.4: Welch's method reduces the variance of PSD estimates. Shown above is the comparison between a series of different periodogram estimates within a single time series and the averaged PSD estimate.

Wave Parameters

The parameters of interest in wave measurement are statistical measurements of wave height and period. As the spectrum captures the behaviour of the wave (assuming a stationary Gaussian process) these can be calculated from the *moments* of the wave spectrum (Holthuijsen, 2007), these are defined as:

$$m_n = \int_0^\infty f^n E(f)\, df \tag{2.15}$$

Where m_n is the n^{th} spectral moment.

The definitions of interest for quantifying wave parameters are(Tucker & Pitt, 2001) given in Table 2.1. These parameters are key in defining the wave activity in a location.

Table 2.1: Wave parameters

Parameter	Equation	Description
T_{m01} or $\bar{T}$	m_0/m_1	The mean wave period.
T_{m02} or T_2	m_2/m_0	The average up-crossing period between waves.
H_{m0} or H_s	$4\sqrt{m_0}$	The significant wave height.

Confidence Intervals

The uncertainty associated with wave measurements is traditionally quantified with a chi-square distribution with confidence intervals of 90% (Earle 1996).

$$\frac{P(f)\cdot DoF}{\chi^2(DoF, \frac{1-\alpha}{2})}, \frac{P(f)\cdot DoF}{\chi^2(DoF, \frac{1+\alpha}{2})}, \tag{2.16}$$

Where $P(f)$ is the PSD estimate, DoF are the degrees of freedom and χ^2 are the percentage points of chi-squared probability.

The degrees of freedom, DoF, can be estimated using:

$$DoF \approx \frac{2K}{1+\frac{0.4(K-1)}{K}} \tag{2.17}$$

Where K are the number of data segments used in Welch's method.

2.2 Hydrodynamics of a single ice floe

The most recognisable feature of the Antarctic Marginal Ice Zone are a type of ice formation known as ice *pancakes*. A description of their formation is given in section 2.3. It is, therefore, necessary to discuss how floating bodies (in this case pancake ice), interact with waves as the SHARC Buoy platform acted as a Lagrangian (ice-tethered) instrument deployed on an ice pancake. Initially, a discussion of how waves *excite* a floating body is provided. Secondly, a discussion of how this excitation can be measured using response amplitude operators is given. Finally, the drift caused by wave *forcing* is discussed and how it affects the measurement of wave activity.

2.2.1 Floating bodies in water

The interaction between waves and floating bodies is generally described by the *excitation* force exerted on a body by incident waves and the *radiation* of waves from an oscillating system. Incident waves excite a floating body, causing it to oscillate. These oscillations in turn cause the body to radiate waves. A floating body in water can be modelled as a simple mass and damper system (Falnes 2002, Fossen 2011). If the system is assumed to be linear then the following linear *mass-spring-damper* model can be used:

$$[\mathbf{M}_{RB}+\mathbf{A}(\omega)]\ddot{\boldsymbol{\xi}}+\mathbf{B}(\omega)\dot{\boldsymbol{\xi}}+\mathbf{C}(\omega)=\mathbf{f}cos(\omega t) \tag{2.18}$$

Where $\boldsymbol{\xi}$ is the perturbation matrix representing the perturbation (small change in movement or position) of the body ($\{b\}$) relative to the equilibrium frame ($\{s\}$), $\mathbf{M}_{RB}$ is the inertial matrix of

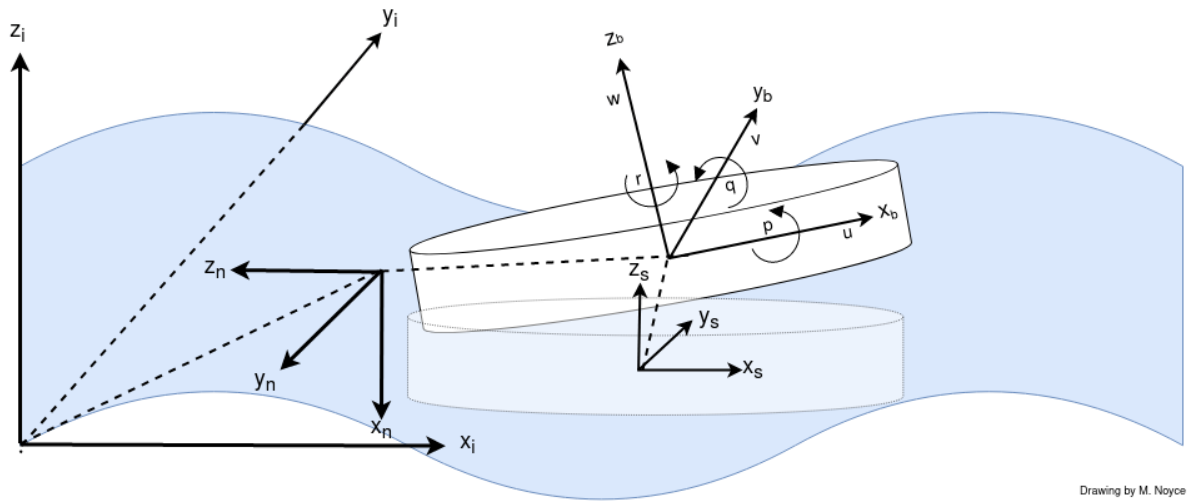

Figure 2.5: The frames of reference for a floating body. In this case a disk model of an ice pancake. The body frame ($\{b\} = \{x_b, y_b, z_b\}$) is a reference frame fixed to the body, inertial measurement occurs in this frame as inertial measurement units will move in this frame, with the addition of a vertical offset in the case of the SHARC Buoy. In this case the body frame is chosen to be located on the geometric centre of the disk but this need not be the case. The position and orientation of the body frame are described relative the Earth-centered Inertial (ECI) frame ($\{i\} = \{x_i, y_i, z_i\}$) which is approximated by the North-East-Down (NED) frame convention ($\{n\} = \{x_n, y_n, z_n\}$). Additionally, the convention for describing the velocities in the body frame is surge (u), sway (v), heave (w), roll (p), pitch(q) and yaw (r). Finally, if the system was assumed to be in equilibrium with no external wave excitation a set of ship-keeping coordinates are useful to define as $\{s\} = \{x_s, y_s, z_s\}$. These help to define the movement of the body relative to its equilibrium state under wave excitation. Note the direction of the axis as shown are considered positive in this thesis. Diagram adapted from Fossen (2011) p.85.

a rigid body, **A** is the added mass matrix, **B** is the damping matrix, **C** is the restoration matrix, f is the external force matrix, ω is the frequency and t is time.

The added mass matrix **A** and the damping matrix **B** model the radiation forces which carry away wave energy from the body. The added mass is caused by a standing wave being formed around the body as a result of the energy imparted to the surrounding water by the oscillation of the body (Journée & Massie 2001). The restoration matrix **C** represents the forces due to gravity buoyancy. these are the forces which tend to *restore* a floating object to the upright position.

Equation 2.18 can be expressed for the heave case shown in figure 2.6, although it is applicable in any of the 6 degrees of freedom about the body axis. In this case $z = z_b - z_s$:

$$(m+a)\ddot{z} + b\dot{z} + cz = F cos(\omega t) \tag{2.19}$$

In the heave case, each of the matrices can be simplified to one-dimensional vectors in the heave direction.

The above solution to the mass-spring-damper model in the heave direction is useful for deriving the response amplitude operators discussed in the next section (2.2.2).

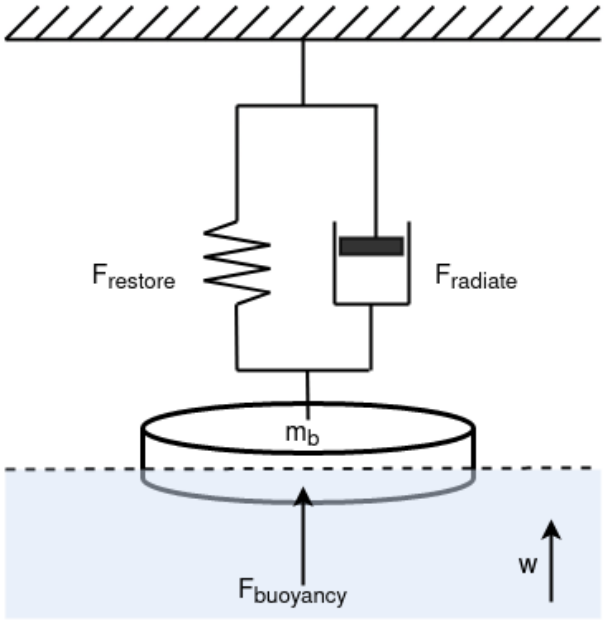

Figure 2.6: Floating bodies in water can be modelled as a mass and damper system. In figure 2.6, the pancake is shown as a mass damper system in heave (w).

2.2.2 Response Amplitude Operators (ROAs)

Assuming a linear system (linear wave theory and a uniform body), the response amplitude operators (RAO) are a series of transfer functions which map the motion (*response amplitude*) of a body to the amplitude of the exciting wave. For the heave case, where $z_a e^{i\omega\theta}$ is oscillating amplitude of the body in response to oscillating wave excitation $\xi_a e^{i\omega\theta}$, the RAO is:

$$H_z(\omega,\theta) = \frac{z_a}{\xi_a} \tag{2.20}$$

If the system is modelled as a mechanical oscillator (i.e. equation 2.19) the RAO can be calculated in terms of the various forces acting on the body. For the simplified case of a floating body being symmetrical about $x = 0$ and $z = 0$ axes (Newman 1977, p. 321) the heave RAO can be given as:

$$H_z(\omega,\theta) = \frac{F}{-\omega^2(a(\omega)+m)+i\omega b(\omega)+c} \tag{2.21}$$

Where F is the external input force caused by the wave input, $a(\omega)$ is the spring constant and $b(\omega)$ is the damping constant and c is the restoration force.

Two key results arise from this formulation (eq. 2.21). Firstly, as $\omega \to 0$ (i.e. long wavelengths and low frequencies) $H_z(\omega,\theta) \to 1$ (Newman 1977). This can be thought of as all the frequency-dependent terms in the denominator tending to 0, leaving only the restoration force c. This is similar to the body motion and the wave motion being equivalent with the common analogy being that of a cork bobbing on the ocean. Secondly, this is the model of a low-pass filter. The response of the body is a low pass filtered response of the input wave excitation. This result has been observed in the Antarctic MIZ with high-frequency waves being largely absent in ice-covered areas (Shen et al. 2001).

The first result is important for an ice-tethered system as it shows that such a system moves with the wave, and not relative to it, if the wavelength is sufficiently large and the wave frequency is

sufficiently low. This is a necessary precondition for the inertial measurement of the movement of waves through ice floes. However, this result only states that there is approximately relative motion between wave and body given the assumption of sufficiently low-frequency, it does not suggest that there is no drift, this will be reviewed in subsection 2.2.3.

The hydrodynamic response and ROAs of a disk model of a sea ice pancake in a wave tank setting have been investigated by Yiew et al. (2016) and Bennetts & Williams (2015). Yiew et al. (2016) found that the idealised floe had ROAs that were approximately unit values for $\lambda/D \geq 3$ (where λ is the wavelength and D is the diameter of the floating object).

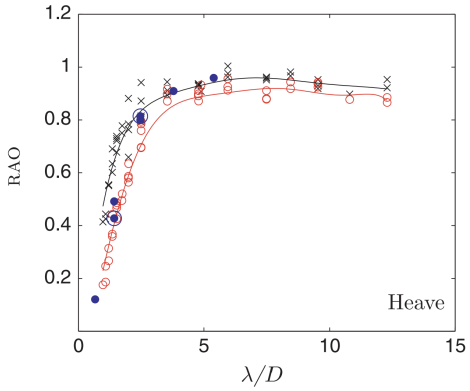

Figure 2.7: Heave Response Amplitude Operator (RAO) for a series of idealised floes. Note that the RAO tends to 1 for each curve at approximately $\lambda/D \geq 3$. Diagram credit: Yiew et al. (2016)

Using the dispersion relation (2.1.3) and the size of the pancake, an estimate of the highest measurable frequency for proxy wave measurement through the pancake can be determined. Given an estimate of pancake size in the Antarctic MIZ during the approximate period the SHARC Buoys were deployed, the winter expanse, a larger pancake (on which the buoys would be deployed) would be on average 3.1 m in diameter (with variation possible due to storm activity) (Alberello et al. 2019). Using 3.1 m as D and the finding of Yiew et al. (2016), $\lambda/D \geq 3$ solving for wavelength, $\lambda \geq (3.1)(3) = 9.3$ m. Finally, solving the dispersion relation for wave frequency:

$$f = \frac{1}{2\pi}\sqrt{g\frac{2\pi}{\lambda}} = \frac{1}{2\pi}\sqrt{g\frac{2\pi}{9.3}} \approx 0.4 \ Hz$$

Thus, a pancake of 3.1 m in diameter in the open ocean under wave excitation will be able to capture the wave information for waves with a frequency of approximately 0.4 Hz (a wave period of ≈ 2.5 $seconds$) or lower.

2.2.3 Wave forcing of floating bodies

Large bodies, relative to wavelength (the dimension of the body being the size of the wavelength or greater) will result in the reflection or scattering of the oncoming waves whereas a small body (its dimension being smaller than the wavelength) will be passively driven by the oncoming waves (Grotmaack & Meylan 2006). This follows from the mass-damper-spring model.

The drift of a floating object caused by wave activity is known as wave forcing. This poses a problem for measurement, as a measurement device would be moving relative to the waves it is

measuring, which would cause a Doppler effect. This can significantly affect the measurement of wave period in steep waves (Longuet-Higgins 1986). It should be noted that both current and wind forcing on a floating body can also cause Doppler shift.

The effect of Doppler shift on the measured wave period (of a Lagrangian instrument) can be calculated with the following equation (Longuet-Higgins 1986):

$$T_L = \frac{\lambda}{c - U} \tag{2.22}$$

Where the Lagrangian period T_L is equal to the wavelength, λ, divided by the drift velocity U subtracted from the phase speed, c. The Eulerian equivalent T_E, for reference can be expressed, $T_E = \frac{\lambda}{c}$.

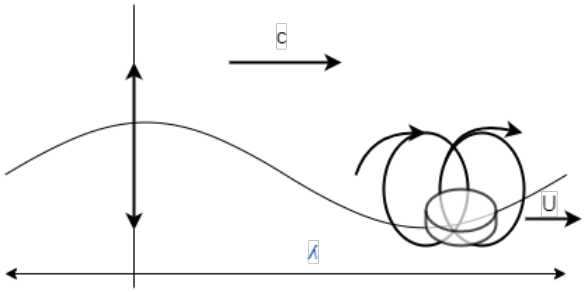

Figure 2.8: The difference between a Lagrangian (left) and Eulerian (right) frames in wave measurement, including the affects of drift (c). Buoy measurements are made in a Lagrangian (body axis $\{b\}$) frame. The fixed (equilibrium/ship-keeping axis) $\{s\}$) is the reference point about which a sensor oscillates in the Eulerian (fixed) frame if the device was tethered. Diagram adapted from Longuet-Higgins (1986)

The drift velocity of the ice relative to the wave thus can have significant impacts on wave measurement. The standard measurement period of 15 - 30 minutes is susceptible to drift-induced bias, particularly given the distance ice can drift within a short period, this should be noted with reference to drift data. This will impact the shape of the measured wave spectrum, especially if the spectrum is assumed to have been representative of a particular geographical coordinate as opposed to being interpolated between coordinates.

2.3 Waves-in-ice

The primary phenomenon investigated using the SHARC Buoy is the phenomenon of waves-in-ice. Thus an overview of the key climatic features of the MIZ that result in waves-in-ice and how this phenomenon is modelled is given. This provides context to the measurements on the SHARC Buoy.

This section starts with a discussion of the lifecycle of the ice in the MIZ, highlighting the interaction between waves (particularly wave frequency) during the processes of formation and recession. In particular, how the evolution of floes may affect the frequency response of a floe on which a Lagrangian device is tethered. A brief overview of the modelling of waves-in-ice from both an individual floe and climate perspective - showing where the measurements from the SHARC Buoy are useful and fit into the greater picture. Finally, an overview of individual processes is provided - to indicate how these processes either affect or can be identified from the SHARC data and their importance to models of the MIZ.

2.3.1 Lifecycle

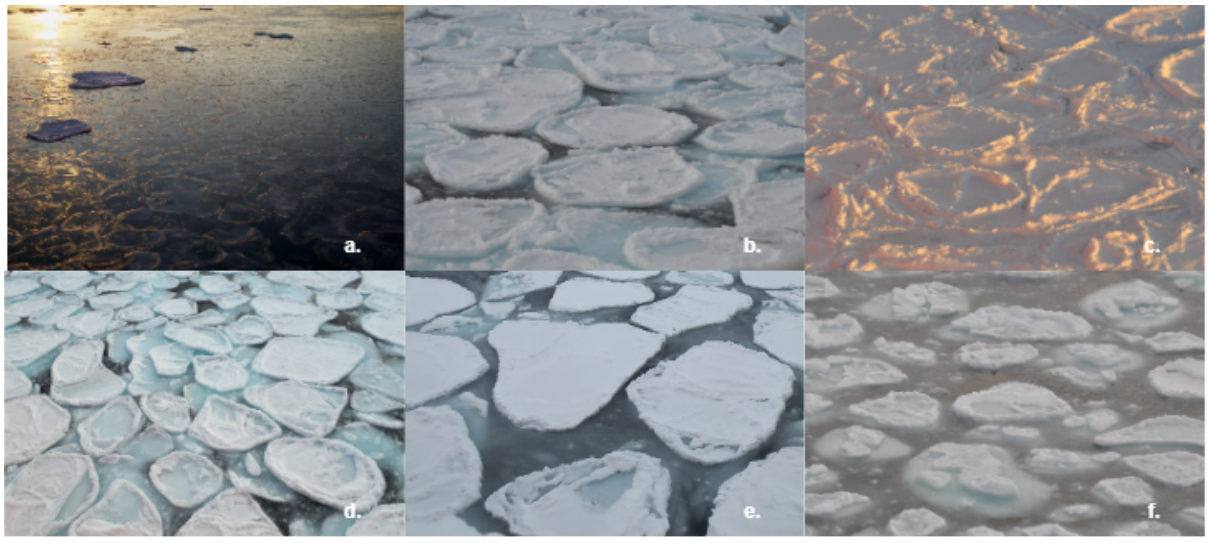

Figure 2.9: Ice type and processes from the SCALE Cruise 2022. Ice Types: (a) Grease ice with ice pancakes, (b) ice pancakes, (c) consolidated ice pancakes/composite ice, (d) larger ice floes made of composite pancakes with interstitial grease/frazil/brash ice (e) melting ice pancakes with interstitial ice. Image credit: (a) Kurt Martin, (b) Marek Marchow, (c, f) Nicole Taylor, (d, e) Marcello Vichi

The lifecycle of the MIZ undergoes periods of ice formation (advance) and recession (retreat). Shen et al. (2001) proposed a three-stage model for the formation of a pancake ice field. Firstly, when the ocean cools sufficiently, frazil ice begins to form, giving the ocean the reflective appearance of grease in water - this is known as grease ice (figure 2.9a). Following the *grease ice stage*, frazil crystals accumulate together, forming ice pancakes (figure 2.9a,b) - the *pancake formation stage*. The raised edges on the pancakes are thought to be caused by collisions with neighbouring pancakes (figure 2.9b,d). Wind and wave activity cause rafting of neighbouring pancakes onto each other (figure 2.9d). Finally, neighbouring pancakes fuse together forming composite pancakes/consolidated sheet (figure 2.9c,e) - the *composite pancake stage*. This model was validated in Arctic ice by (Roach et al. 2018)

It is important to note that the formation process has a strong relationship with wave activity. High-frequency wave components cause the accumulation of frazil ice into pancakes (Yue & Shen 2021) and lower-frequency components 'herd' pancakes together into composite pancakes/sheets (Shen et al. 2001).

A proposed mechanism for the thickening of ice pancakes is the rafting (figure 2.9d) of separate floes onto each other (Dai et al. 2004). The rafting and thickening of floes would change the hydrodynamic response of the individual floes by increasing their diameter or thickness. However, the SHARC Buoys were deployed on either consolidated (figure 2.9c) or large floes (figure 2.9e). Though it is possible that rafting occurred prior to the storm's arrival on the 22 July 2022.

Melt of sea ice generally occurs in spring. However, winter melt was observed during the deployment period on the SCALE Cruise during July 2022 (2.9f). The cause of the melt is currently unknown. However, it is known that, once the ice starts to melt, waves penetrate further into the ice and break up increases (Vichi et al. 2019).

The size of the floe, particularly the diameter of the floe, affects the hydrodynamic response of the floe (chapter 2.2). Thus, the evolution of the floes over time changes the response of the floes to waves and in particular - their response to high-frequency events such as collisions.

2.3.2 Attenuation

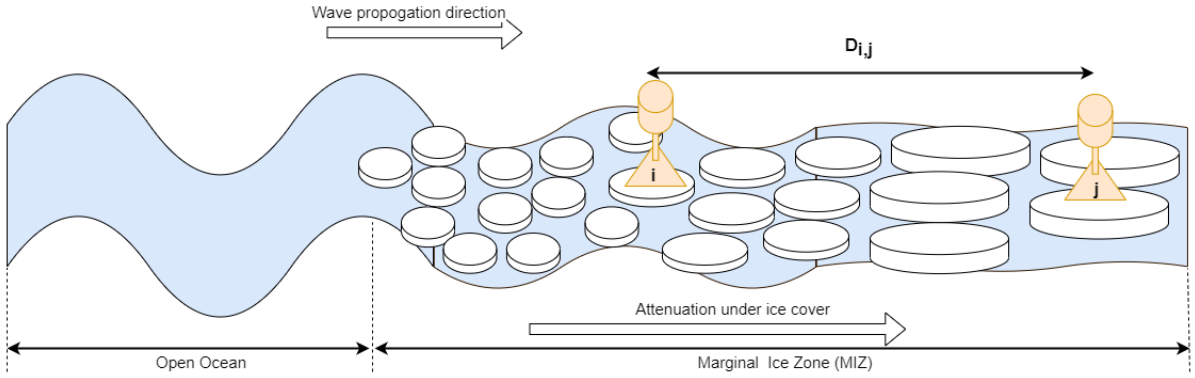

Figure 2.10: The propagation of waves through ice results in the attenuation of wave height. There are a variety of mechanisms proposed for the attenuation. Simple measurement of attenuation between two SHARC Buoy sensors (i, j) is shown.

A well known waves-in-ice phenomenon is the attenuation of wave height, generally as a function of frequency as waves propagate through the ice in the Antarctic MIZ(Thomson 2022). The frequency dependence has been shown through a variety of campaigns (Meylan et al. 2014, Kohout et al. 2020) in different ice conditions and in the modelling of the region (Meylan et al. 2018, Squire 2018). The ice cover generally acts like a low pass filter with exponential attenuation of high-frequency wave components with low frequency waves propagating far into the MIZ(Kohout et al. 2020). Attenuation rates have been shown to be sensitive to ice type (Rogers et al. 2016), floe size (Roach et al. 2019) and concentration (Doble & Bidlot 2013).

Meylan et al. (2014) calculated the attenuation coefficient in the Antarctic MIZ with the following equation:

$$\alpha(T) = \frac{In(S_i(T)/S_j(T))}{D_{i,j}} \tag{2.23}$$

Where S_i and S_j are the wave spectra at sensors separated by distance $D_{i,j}$. S_i is assumed to be further North if the *North-South assumption* is used. Many studies have assumed that waves enter the ice cover, refract and proceed to travel meridionally South (Meylan et al. 2014, Kohout et al. 2020, Brouwer et al. 2022). This is likely due to the difficulty in determining wave direction as a result of the magnetic interference experienced by magnetometers (which are generally used to determine heading) - this will be discussed in chapter 2.6.

2.3.3 Ice floe collisions

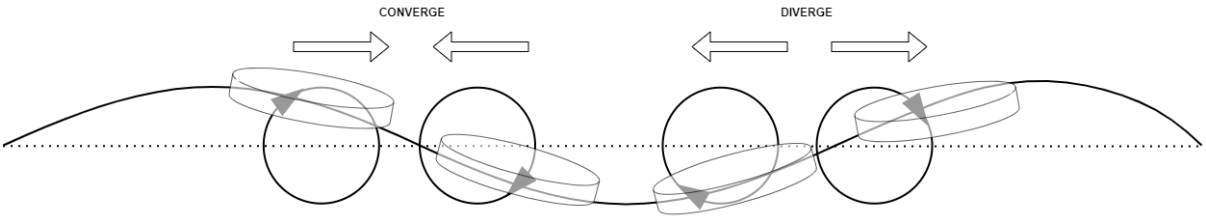

Figure 2.11: Impacts between floes can be caused by the orbital motion of the individual floes relative to each other - resulting in a regular periodic impact pattern. In this diagram waves are propagating from left to right.

Collisions between ice floes have been proposed as a mechanism for the attenuation of waves-in-ice. The interaction between floes has been modelled, in the simplest case, using wave orbits (Rottier 1992) as depicted in figure 2.11.

These impacts have been investigated in a wave tank setting. Bennetts & Williams (2015) investigated the transmission of waves through an array of floating disks and it was determined that wave impacts became a significant cause of wave attenuation at higher concentration arrays which was under-predicted by modelling - likely caused by collisions between the disks. In the experiment, an acceleration threshold was set in the x-axis facing towards the incident waves.

Yiew et al. (2017) investigated the waves induced impacts between two floes. They found that disks collide regularly in the intermediate to long wavelength regime (≥ 3 times disk diameter) and that, for long wavelengths, collisions are caused by the relative surge motion which can be predicted by the surge motion of a solitary disk. It is interesting to note that wavelength to disk diameter to achieve a ROA of 1 (≥ 3 disk diameter) is the same ratio which is associated with the transition to a frequent collision regime (see section 2.2.2).

Finally, collision events have been measured in the Antarctic MIZ by Smith & Thomson (2020). They found that the relative velocity of floes predicted the frequency of impacts. The impacts result in a transfer of momentum between floes. Assuming disk-shaped floes, the transfer of momentum can be expressed by the following equation from Shen et al. (1987):

$$\Delta M = \rho_s (V_A - V_{A*}) \frac{\pi D^2}{4} \tag{2.24}$$

Where the change in momentum, ΔM is equal to the density of the ice floe, ρ_s, multiplied by the change in velocity of floe A before and after the collision, $V_A - V_{A*}$, multiplied by the volume of the disk-shaped floe with diameter D, $\frac{\pi D^2}{4}$.

The relative velocity of floes can also be used to estimate the dissipated energy as a result of the collisions. The original formulation of the energy dissipation between floes is given by Shen et al. (1987) as the change in kinetic energy before and after a collision:

$$e_c = \frac{1}{2} \rho_s ({V_A}^2 - {V_{A*}}^2 + {V_B}^2 - {V_{B*}}^2) \frac{\pi D^2}{4} \tag{2.25}$$

Where the energy dissipated by a collision of identical floes is equal to the mass of the individual floes given by the density of the floes, ρ_s, multiplied by the volume of each floe with diameter, D,

given by $\frac{\pi D^2}{4}$, multiplied by the change in velocity of each floe summed together.

This requires measurements from both the floes immediately before and after the collisions. Thus, in situ measurements can only practically measure the intensity and frequency of floe-floe collisions as the transfer of momentum cannot be fully measured unless there is an instrument placed on all floes involved in a collision. This is still of significant interest in characterizing the floe dynamics, both from an inertial measurement perspective as it contaminates wave measurement and because it has not been measured for a long duration (multiple days on a single floe) to the author's knowledge.

The contamination of wave data was noted by Doble et al. (2017) in the transmitted raw data from the Novel Directional Wave Buoy (NDWB) platform. They reported outputs from the Kalman filter onboard the system became unrepresentative with root mean square values of displacement outputted by the Kalman filter exceeding 20 times the displacement calculated from the z-acceleration (heave). Thus, for an accurate measurement of wave height, either the raw data must be collected or a filtering system should be designed to remove the contamination of ice-impacts.

2.4 Inertial Measurement Units

The instrument used to measure waves-in-ice phenomena on the SHARC Buoy was a low-cost IMU. It is therefore necessary to discuss the advantages and limitations of such an approach. This section starts with a description the principles of operation of the IMU. A discussion of the error characteristics of IMUs is then given, with references provided as to how this may affect wave measurements. Finally, the calibration of IMUs is discussed.

2.4.1 Theory

Inertial Measurement Units (IMUs) utilise a microelectromechanical (MEMS) system to measure acceleration and angular velocity on a small integrated circuit (IC). These are used on the SHARC Buoy to measure wave activity. They are strapdown devices meaning that they operate in the body frame ($\{b\} = \{x_b, y_b, z_b\}$), assuming that the IMU measurement axes and the body are orthogonal. A 6 degree of freedom (DOF) IMU will measure acceleration and angular velocity values in three orthogonal axes. A 9 DOF device includes a magnetometer to determine heading.

The devices are susceptible to several sources of error, particularly drift of integrated acceleration and angular velocity measurements, which needs to be accounted for in processing of the measurements of the device.

2.4.2 Error characteristics

IMUs are susceptible to multiple types of error. The main types of error are:

- Scale error (s_g, s_a)
- Bias (b_g, b_a)
- Random noise (u_a, u_g)

The scale factor is a multiplying factor used to convert between the output and the input. In this case, the conversion between a raw accelerometer or gyroscope output. Thus the scale error is the difference between the actual scale factor and the used scale factor.

The bias is the offset of the measured output when there is no angular velocity or acceleration

acting on the device. This bias should be removed before integration.

The random noise is the Gaussian (white) noise in the measured output. This is often quoted in terms of noise density which is the noise divided by the square root of the sample rate.

The general model for measurement noise in an IMU is given by (Chao et al. 2010). The error model for the gyroscope is given as:

$$\hat{\boldsymbol{\omega}} = (1 + \boldsymbol{s_g})\boldsymbol{\omega} + \boldsymbol{b_g} + \boldsymbol{u_g} \tag{2.26}$$

Where the measured value of angular velocity, $\hat{\boldsymbol{\omega}}$, is given by one plus the scaling factor, s_g multiplied by the true value of angular velocity, ω, plus the addition of white noise, μ_g.

And the error model for the accelerometer is given as:

$$\hat{\boldsymbol{a}} = (1 + \boldsymbol{s_a})\boldsymbol{a} + \boldsymbol{b_a} + \boldsymbol{\mu_a} \tag{2.27}$$

Where the measured value of acceleration, $\hat{\boldsymbol{a}}$, is given by one plus the scaling factor, s_a multiplied by the true value of angular velocity, a, plus the addition of white noise, μ_a.

The error for the devices resulting from bias can be determined by removing the measured bias from the IMU after determining it from a sufficiently long time series measured while the device is stationary. The scaling factor can be determined using the multi-position method of calibration (subsection 2.4.3).

For Kalman filtering of IMU data (subsection 2.8), a key parameter of the filter is the drift due to the integration of noise, known as angle random walk (ARW) for the gyroscope or velocity random walk for accelerometers. These error terms are determined using the Allan Variance method, which is a method for determining the stochastic noise terms from a time series (see Appendix D).

2.4.3 Calibration

The calibration of IMUs can be done before measurement, for low-cost applications this is generally done with a multi-position method, where the IMU is rotated between a number of static positions, which allows for the angular velocity to be integrated between positions described by a gravitational vector. This allows the gyroscope to be calibrated. Accelerometer readings are generally determined by a comparison between the gravitational vector and the measurement in each axis. The approach initially used in the thesis was the approach of (Tedaldi et al. 2014).

In wave applications, if linear wave theory is assumed, the device is assumed to oscillate about a point, thus - detrending acceleration data is an effective means to determine the acceleration in the body frame (without drift) assuming the scaling factor is accurate.

2.4.4 Validation

For wave measurement applications, IMU's are validated with wave tank testing. This is done by feeding a known set of wave measurements with a known frequency and wave height and comparing this to the measured wave height. An example of this approach can be found in Rabault et al. (2016).

2.5 Wave measurement

The IMU data collected on the SHARC Buoy is processed into wave data. The section discussed how the vertical acceleration in the inertial axis is calculated from the 6 DOF (degree of freedom) IMU measurements. Following this, an outline of the approach to integrating the vertical acceleration to displacement is given.

2.5.1 Determination of vertical acceleration

The fusion of the inertial data collected in the body frame to determine the acceleration in the vertical axis (z_i) of the inertial frame ($i = x_i, y_i, z_i$) is necessary to measure waves in the unidimensional case. The vertical acceleration values are used to calculate displacement after a double integration. Thus, the method of fusing the IMU data from a multiple DOF measurement to a single DOF is needed.

The easiest method of determination of the vertical acceleration is to assume that the heave experienced by the body is approximately the true vertical acceleration. This assumption is true assuming that the wave slope is small (i.e. $\leq 10°$, see figure 2.12) as the small angle assumption ($\leq 10°$) for pitch (θ) and roll (ϕ) will hold in this case. This is generally the case in the Antarctic MIZ. The advantage to this method is that it simplifies calculation (not a trivial requirement on embedded systems), and reduces noise (each measurement DOF introduces noise), and so is used widely. For example, the Waves-in-ice Observation System (Kohout et al. 2014) and the Novel Directional Wave Buoy (Doble et al. 2017) both used the heave acceleration only to calculate wave height. However, if the waves become steep or there is a sustained tilt of the platform it will overestimate the wave height. Alternatively, if there is no tilt it will underestimate wave height (Bender et al. 2010). This approach can be represented as (Bender et al. 2010):

$$\hat{\mathbf{A}}_z^{\,i} \approx \hat{\mathbf{A}}_z^{\,b} \approx \mathbf{g} - Z_s \tag{2.28}$$

Where the estimate of the true vertical acceleration $\boldsymbol{A}_z^i$, is approximately equal to the vertical acceleration of the platform, $\hat{\boldsymbol{A}}_Z^b$, is given by the gravitational acceleration, g, multiplied by 1 subtracting the acceleration measurement of the sensor, Z_s, measured in m/s^2.

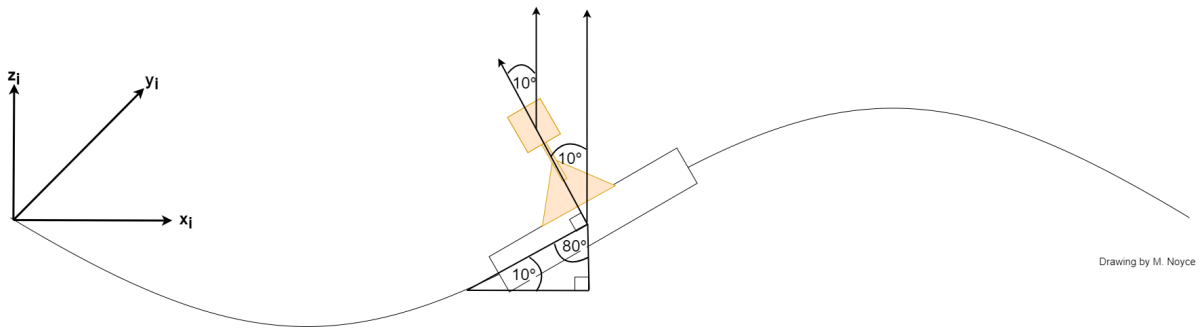

Figure 2.12: A small angle assumption is necessary to use only the heave acceleration measurements to measure wave activity for the unidimensional case.

The true acceleration of the platform is given by using pitch and roll information to accurately determine the component of gravity acting on the z axis of the accelerometer (Bender et al. 2010):

$$\mathbf{A}_z^b = (\mathbf{g}cos(\theta)cos(\phi) - Z_s)cos(\phi)cos(\theta) \tag{2.29}$$

The true vertical acceleration (acceleration in the z_i direction) can be calculated by determining the true vertical acceleration of the platform and transforming it into the inertial frame. This is given by the following equation (Bender et al. 2010, Kohout et al. 2014):

$$\hat{\mathbf{A}}_z^i = \mathbf{g} - (sin(\theta)X_s + sin(\phi)cos(\theta)Y_s + cos(\phi)cos(\theta)Z_s) \tag{2.30}$$

For the directional case, the heading of the device is needed to determine the directional measurements. This requires an accurate measurement of yaw, this is generally measured by a magnetometer as the drift in the gyroscope is too great for the mission duration of instruments (generally not an acceptable error within a few minutes of operation). Unfortunately, magnetometers do not function accurately in the Antarctic MIZ (Kohout et al. 2014).

2.5.2 Integration of acceleration data

The integration of the vertical acceleration into vertical displacement is necessary to determine wave amplitude. This is generally done using a double integration in the frequency domain (Rabault et al. 2020, Alari et al. 2022, Kohout et al. 2014) with a high pass filter used to remove low frequency drift introduced by the white noise and spreading from other frequencies within the spectrum (Lang 1987). The following function describes both the high pass filtering (note the removal of frequencies below f_1 and the cosine taper between f_1 and f_2) as well as the double integration (note the multiplication by $\frac{1}{\omega^2}$).

$$r(f) = \begin{cases} 0 & f \leq f_1 \\ \frac{1}{2}(1 - cos(\frac{f-f_1}{f_2-f_1}))(\frac{-1}{2\pi f})^2 & f_1 \leq f \leq f_2 \\ \frac{-1}{(2\pi f)^2} & f \geq f_2 \end{cases} \tag{2.31}$$

The frequencies f_1 and f_2 are chosen based on the expected wave period. The Waves-in-ice Observation system (Kohout et al. 2014) and the waves-in-ice buoy (Rabault et al. 2020) both used $f_1 = 0.02Hz$ and $f_2 = 0.03Hz$ which is selected for waves with periods ranging from 4 to 20 seconds. (Alari et al. 2022) selected $f_1 = 0.08Hz$ and $f_2 = 0.10Hz$ which they deemed to be sufficient for their measurements in the Baltic, noting that a lower cut-off would require validation.

2.6 Waves-in-ice instruments

A comprehensive overview of the current waves-in-ice instruments is given by Jacobson (2021). However, some recent developments have occurred after this review that will be discussed here, as well as a focus on the specific wave measurement capabilities of each of the devices. The section starts with a discussion of the general requirements of the SHARC buoy system to provide context to the updates that were made to the system for the V3.0 model. Then a discussion of the sensor fusion techniques used by the most recent systems is provided.

2.6.1 Embedded System

The waves-in-ice instruments have several common requirements for their embedded systems. These are discussed in table 2.2. Fundamentally there is a trade-off between power consumption, with low-power MCUs being ideal and processing power with Linux System-on-a-Chip (SoCs) generally being more powerful.

New platforms such as the OpenMET Buoy V2021 (Rabault et al. 2022) and systems based off its design such as the open source ice tracker (Rabault 2022) have shifted away from a Linux SoC and towards a central MCU with sufficient memory (both flash and RAM) for onboard digital signal processing (DSP). This trend is followed by the LainePoiss Buoy which also uses a central MCU (Alari et al. 2022). This is a revision from alternative devices such as the revised Waves-in-ice-Observation-System (Kohout et al. 2020) which uses an Intel Edison SoC (along with a MCU to control low-power modes) and the open source waves-in-ice buoy (Rabault et al. 2020) which used a Raspberry Pi. These older devices make use of the large RAM and more powerful DSP libraries available.

The STM32 series of MCU's as well as other ARM MCU's based on the Cortex-M processor have the CMSIS DSP library available for use (ARM 2022). The library includes the following functions necessary for developing a wave measurement pipeline on the buoy:

- Finite Impulse Response (FIR) filtering
- Real Fast Fourier Transform (RFFT)
- Real Inverse Fast Fourier Transform (RFFT)

These can be leveraged to have a more power and cost efficient solution for the onboard signal processing required for the estimation of wave parameters as these functions have been optimised to perform on the Cortex-M hardware. It is important to note that the length of the operations is generally constrained to arrays of 256, 512 or 1024 in length.

Table 2.2: The general requirements of the embedded systems for waves-in-ice instruments.

Requirement	Description
Interface with multiple sensor packages	The central embedded system must be able to interface with several sensor packages over a variety of communication protocols. Specifically: I2C, SPI and UART/USART interfaces
High-frequency IMU interface	In particular, each instrument contains an IMU device. This sensor package is sampled at a high-frequency (approx. 100-640 Hz). Further the interface must function reliably for extended periods.
Onboard digital signal processing (DSP)	The devices must have the ability to process large stored inertial datasets with DSP functions such as the Fast Fourier Transform (FFT), Finite Impulse Response (FIR) filtering. Furthermore, the length of the DSP operations on the system should be sufficient (eg. 512, 1024, 2048) to process segments of the signal without causing significant distortion.
Random Access Memory Size	The local processing of data is done using the random access memory on the embedded system. This memory must be sufficiently large to store and operate on the the maximum number of numerical arrays used concurrently during the onboard processing.
Program memory size	The memory storage for the embedded system must be large enough to store the full program implemented on the system. Generally implemented in Flash memory on MCUs, this requirement is an important requirement for a smaller system - especially when the system grows in size. On larger Linux SoC systems, this is not a significant requirement.
Storage memory	The storage memory must be large enough to store the raw data logged during deployment for local processing or in case of retrieval. The hardware storage type and interface must be highly reliable in extreme conditions.
Power consumption	The type of embedded system (MCU, SoC etc.) selected and the implementation of the program has significant impacts on the power consumption of the device. Long-duration missions are the ultimate goal for waves-in-ice devices and so an appropriate embedded system must be selected.

2.6.2 Sensor Fusion

The determination of wave height from inertial measurements requires the calculation of vertical acceleration using information from all the axes present on the IMU (with the exception of yaw for the uni-dimensional case). IMU measurements are generally filtered using a Kalman filter. This filter fuses the information from multiple raw measurements along with a model of the system to produce an estimate of the system's behaviour (e.g. orientation). Kalman filtering has been used in the Waves-in-ice Buoy (Rabault et al. 2020), the LainePoiss Buoy (Alari et al. 2022) and the Novel-Directional Wave Buoy (Doble et al. 2017).

The Kalman filter is an optimal state estimator that aims to minimize the error covariance.

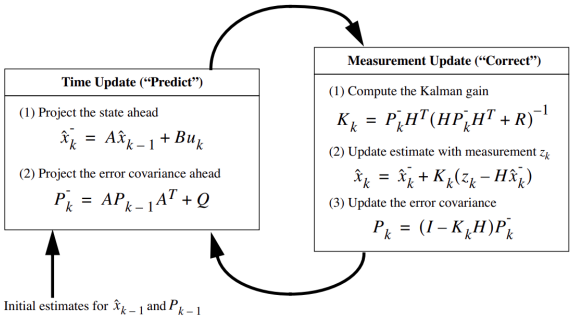

Figure 2.13: Overview of the operation of the Kalman Filter. Diagram credit: Bishop & Welch (2001).

In this thesis, Kalman filtering is treated as a black box, with the IMU error values being used as parameters of a generic filter used to determine the orientation of the buoy. This orientation is used to determine the vertical acceleration using the methods outlined in subsection 2.5.1

2.7 GPS wave measurement

GPS wave measurement is an alternative to the IMU based wave measurement given described above. Herbers et al. (2012) have developed a GPS based platform that used the differential measurements in Doppler shift of GPS signals to determine the orbital velocities of waves. Alternatively, positional GPS measurements can be used with post-processing techniques (Raghukumar et al. 2019). GPS based Spotter buoys, developed by Raghukumar et al. (2019), showed good agreement with Datawell rider inertial measurement based buoys in deployments on the California coast. SWIFT Buoys, which are also capable of GNSS based wave measurement, have collected waves-in-ice data in the Arctic (Hošeková et al. 2020). GPS based minibuoys have been deployed in the Antarctic for waves-in-ice measurement (Ardhuin et al. 2020).

GNSS based wave measurement was not implemented on the SHARC Buoy as there was a concern that GNSS based wave measurement has not been validated in the Antarctic against IMU wave data to the authors knowledge. However, GNSS measurement should be considered for future buoys (see 11).

2.8 Literature review summary

An overview of linear wave theory was provided along with the limitations of this theory, as this is the dominant theory used to describe waves in deep water such as the Antarctic MIZ. The dispersion relation and the relationship between wavelength and frequency in gravity was described.

The mathematics used to describe linear waves in the open ocean was outlined, specifically wave spectra, with a focus given on how variance is reduced between power spectra estimates using the Welch method. The calculation of wave parameters from these spectra is described along with the calculation of the uncertainty in the statistical estimates calculated from the wave spectra.

The hydrodynamics of wave flows is given as justification for the proxy measurement of waves through ice with ice-tethered instruments. Additionally, the various sources of error introduced by the proxy measurement were described.

The error characteristics, calibration and validation of IMUs for wave measurement was given with a focus on wave measurement applications.

The various approaches for wave measurement (for the uni-dimensional case) were investigated with the applicability of the small angle assumption being outlined. The integration of vertical acceleration was described with different frequency ranges between devices noted.

Considerations for wave measurement using embedded systems were investigated with the use of Kalman filtering for sensor fusion briefly discussed.

Finally, GNSS based wave measurement was discussed with reasoning given as to why it was not used.

Chapter 3

Waves-in-ice measurement

The SHARC Buoy V3 measured wave activity through ice. This required the validation testing of the IMUs used to measure the wave activity. Wave tank testing was used to validate the wave measurement by verifying that wave frequency and height could be extracted from the raw IMU data. Additionally, the frequency response of the IMU measurement on a pseudo-ice pancake was investigated. A signal processing pipeline was implemented, both on MATLAB and in a more resource-constrained form for the STM32 microcontroller (MCU) for local processing of wave data. The MCU implementation is discussed in detail in chapter 6.4. Finally, the necessary corrections in the wave measurement are considered. These include determining the true vertical acceleration, correcting for the stand dynamics and finally the Doppler shift introduced by drift.

3.1 Wave tank testing

3.1.1 Experimental Setup

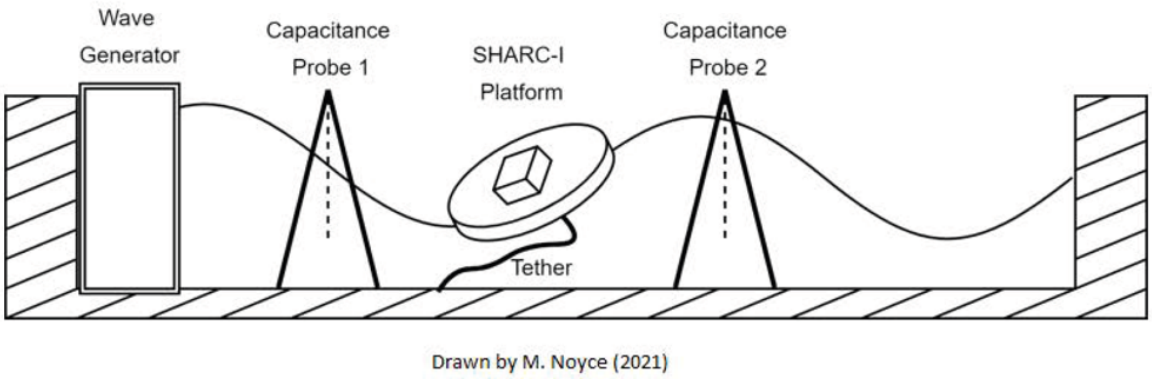

Figure 3.1: The setup included a pancake tethered 7 m from a wave generator, with a capacitance probe placed 1 m in front and 1 m behind the pancake. The pancake was made of polypropylene which has a density of 0.905 g/cm^3 which is approximately equivalent to the density of ice 0.91 g/cm^3 (not accounting for variation in sea ice). The pancake was 30 cm in diameter and 4 cm in height. An IMU data logger was placed on the centre of the pancake in a waterproof housing. The wave height was calibrated using capacitance probe 1, with probe 2 there to detect attenuation at various frequencies. For the full setup and experimental planning, refer to Appendix A.

The validation of IMU wave measurement was done in the wave tank at the CSIR Coastal and Hydraulics Laboratory, in Stellenbosch, South Africa. The waves were generated in a 32 m x 1 m

2D glass wave flume with a piston paddle wave-maker designed by HR Wallingford. The experiment was designed to generate a series of waves which could then be measured by a floating IMU logger which would have similar inertial characteristics to an ice pancake floe. This was done by constructing a scaled-down plastic disk 30 cm in diameter with a thickness of 4 cm. A disk shape was selected to approximate the shape of ice pancakes in the MIZ (see figure 2.9) The plastic used was polypropylene which has a similar density to ice at 0.905 g/cm^3 (Rochling 2021) which is similar to the density of sea ice which varies widely but has an average density of 0.91 g/cm^3 (Timco & Frederking 1996). This was constructed to try and mimic the inertial response of pancake ice. The generated waves were measured by two capacitance probes. The waves were calibrated from the measurements of probe 1 with probe 2 being used to determine if significant attenuation of waves occurred between probe 1 and the logging platform (SHARC-I) which would bias the validation. A longshore was created on the opposite side of the wave tank to dampen waves and reduce reflection. As the tank was 32 m, no detectable reflection was measured by the probes deployed at 7 m and 9 m from the wave generator respectively.

The ideal wave series would emulate the waves measured in the MIZ. However, the use of the wave tank imposes constraints. The primary constraint is the depth of water in the tank (0.8 m), which is lower than the height of the tank (1.0 m), meaning that a smaller wave height with longer wave length is necessary to assume linear wave theory. Additionally, the wave height cannot be too small relative to the wavelength of the wave else surface tension will become a significant force relative to gravity (cnoidal waves). The wavelength should be several times the length of the platform to allow the platform sufficient response time to the individual waves (see subsection 3.1.3). Finally, the drift should not be sufficiently large that the tether introduces additional dynamics into the measurement.

1. The tank depth (1m in the CSIR Lab) is sufficient (i.e. $kd < 2$) to assume deep ocean assumptions (no reflection off tank bathymetry)

2. That scaling the waves relative to the size of the floe will yield result that can approximate real world conditions

3. That wave steepness, $ka < 0.08$, allows for linear wave theory (or an n^{th} order Stokes correction) to be used.

Given these constraints, waves with accelerations in the range that would be measured in the MIZ were generated and used to validate the IMU. A table of the wave parameters is given (table 3.1). Higher and steeper waves could be used for frequency identification but for calculating wave parameters, the restrictions above were necessary.

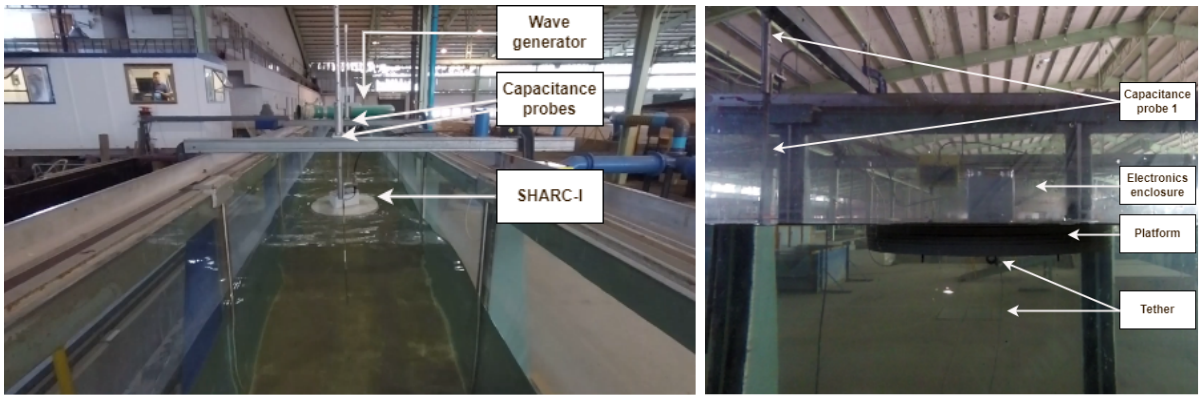

(a) Front perspective **(b)** Side perspective

Figure 3.2: Wave tank testing

3.1.2 IMU Validation

To validate the IMU used in the buoy, wave tank testing of the selected IMU was performed. The ICM20689 (InvenSense 2021*b*) was initially used as the selected IMU. This was replaced with the ICM20649 (InvenSense 2021*a*) as a result of silicon supply shortages.

A logger was developed using the Arduino Due board powered by a compact portable power supply with the selected IMU. The logger was placed in a waterproof enclosure fixed to the center of the top surface of the pancake. The IMU was located in the center of the pancake. The IMU logged at a frequency of 100 Hz. The ICM20689 experiments lasted for a duration of 5 minutes whilst the ICM20649 experiments were 30 minutes in duration.

The IMU measurement was compared to the measurement of the capacitance probes within the wave tank. These probes were calibrated before the start of an experiment and are accurate to within 0.5 mm.

Table 3.1: Wave parameters for IMU validation experiments

Experiment Description	Tm01 (s)	Hm0 (mm)	IMU	Wave Spectrum	Relative depth (kd)	Steepness (ka)	Ursell Number
IMU validation: Identify dominant frequency	0.875	61	ICM20689	JONSWAP	4.21	0.16	0.17
IMU validation: Identify dominant frequency (repeat), measure wave parameters	0.889	54	ICM20689	JONSWAP	4.07	0.14	0.16
IMU validation: Identify dominant frequency	1.997	32	ICM20649	Regular (sinusoidal)	1.04	0.02	1.47
IMU validation: Measure wave parameters	1.713	44	ICM20649	JONSWAP	1.28	0.04	1.33

The simplest validation tests determined if the measured vertical acceleration (heave acceleration) correlated to the acceleration measured using the capacitance probe. This is shown in figure B.3. It is important to note that if the waves imparted too much lateral drift, dynamics would be introduced by the tether, resulting in phase shifts and or a reduction in the measured acceleration amplitude as can be seen in the time series (figure 3.3a) beyond $t = 7$ seconds. The dominant frequency ($f \approx 1$ Hz) can also clearly be identified.

The ICM20649 was validated using two time series a series of regular waves and a series of irregular waves. The regular waves were used to determine that the correct elevation was measured and that a specific frequency could be accurately measured. The irregular waves were used to validate the estimation of wave parameters. This allowed for the calculation of wave height to be more accurate as the calculation of the significant wave height involves the integration over the wave spectrum (subsection 2.5.2). As a regular wave (sinusiodal wave with a single frequency) has a wave spectrum which in the ideal case has a Dirac delta function at the wave frequency (a function

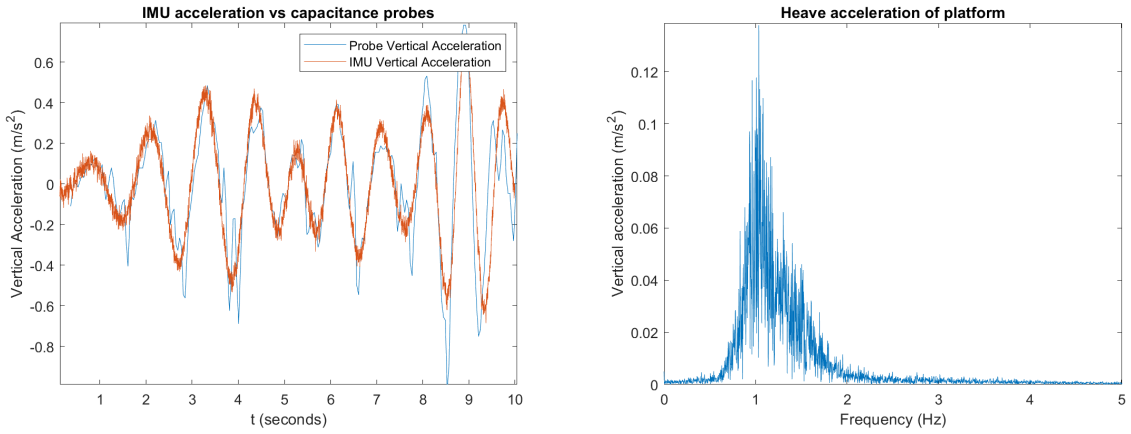

(a) Acceleration time series **(b)** Raw FFT

Figure 3.3: Figure 3.3a acceleration time series of the heave measurement of the ICM2089 IMU (orange) vs the measured displacement of the capacitance probe differentiated (blue) to determine measured acceleration (Wave Spectrum: JONSWAP, Wave Frequency: 1.14 *Hz*, Hm0: 61 *mm*). Figure 3.3b, FFT to determine the frequencies present in the acceleration signal.

which is zero for all frequencies except at the wave frequency). Practically, there is some frequency spread which allows an estimate of wave height. However, the accuracy of the estimates is reduced as a result.

Another consideration was the integration of the data, double integration in the frequency domain specifically the frequency cutoff defined the cosine taper (subsection 2.5.2). The use of the platform and a strapdown accelerometer introduced low-frequency noise in the range $0-0.1$ *Hz*. This noise is known to be introduced by the floating platform itself, thus during the wave tank testing integration was done for the range $0.15-4$ *Hz*. For the system itself the cutoff of 0.03 *Hz* was used as there has not been a quantification of the low frequency noise introduced by the ice floe onto which the device is deployed. 0.03 *Hz* is the frequency threshold below which there is no significant wave energy and so is used in many buoys (Rabault et al. 2020, Kohout et al. 2015).

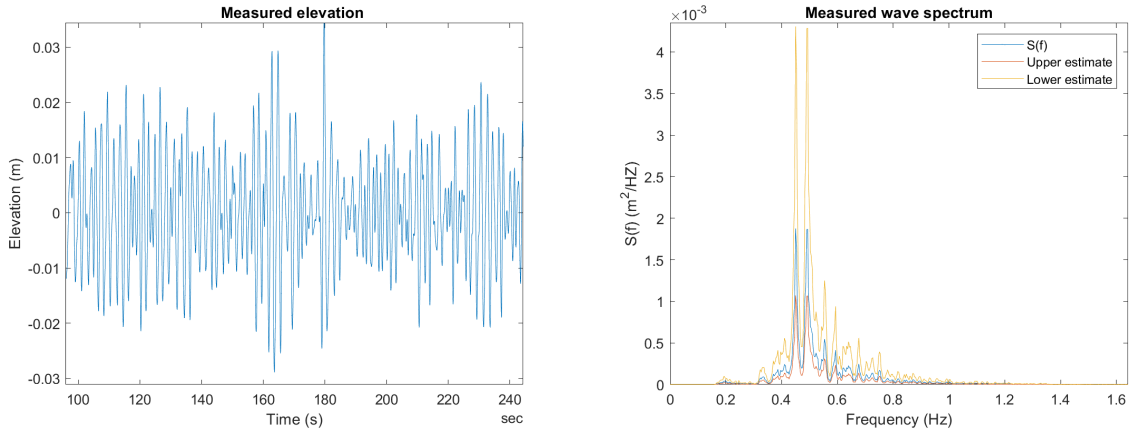

(a) Elevation time series **(b)** Wave spectrum (Welch estimate)

Figure 3.4: Figure 3.4a elevation time series calculated from the heave measurement for the ICM20649. Capacitance probe wave spectrum shown in Appendix B.2a. Figure 3.4b IMU measured wave spectrum.

Table 3.2: Wave parameters measured by the capacitance probes vs. IMU measurements

Parameter	Capacitance Probe	IMU
Hm0	0.044 m	0.042 m
Tm01	1.713 s	1.857 s

The significant wave height was chosen to be approximately 5 cm to increase the size of the acceleration signal relative to the noise of the sensor (see chapter 5.3.2). The dominant wave period was chosen to be approximately 0.5 Hz (see Appendix B for datasheets). This allowed for a test that did not introduce the dynamics of the tether as it resulted in minimal drift as the wavelengths were sufficiently long relative to the size of the platform. Additionally, as the waves were irregular, the different wave frequencies in the spectrum would correspond to different wave elevations, allowing the lower frequency range and wider acceleration range to be validated.

The measured significant wave height was within 2 mm of the value measured by the capacitance probes in the wave tank. The difference in mean wave period can be accounted for the "spectral spreading" (see Lang (1987)) introduced by the platform itself causing higher frequency components to shift to lower frequency bins, which are then removed by the high pass filter described above (frequency cutoff of 0.1 Hz), The removal of the low frequency components during the integration from acceleration to displacement integration results in a marginally higher mean wave period calculated from the spectral moments of the wave spectrum.

The measured acceleration range can be calculated using (Rabault et al. 2016):

$$A_z = a\omega^2 \tag{3.1}$$

Where A_z is vertical acceleration, ω is the angular frequency (given by $\omega = 2\pi f$) and a is amplitude. The frequency range being $0.30 - 1.0$ Hz. The peak acceleration is given by equation 3.1 as 0.5 m/s^2. For an expected wave period in the MIZ of 10 s, this would correspond to approximately 1 m wave height.

Note that the peaks of the spectrum (figure 3.4b) are not as high as measured in appendix B.2a, this is due to spectral spreading as a result of the platform of the peak amplitudes into neighbouring frequencies (see subsection 2.5.2 and Lang (1987)). This is in addition to the loss of spectral resolution caused by the use of the Welch method.

The experimental testing validated the cost-effective IMU for the dominant acceleration range that would be measured in the MIZ during storm activity (i.e. significant wave height > 1 m). The validation of smaller acceleration measurements was determined by measuring the noise floor of the sensor (subsection 5.3.2). For further validation or for updating the IMU, lower wave amplitudes should be selected. Validation of lower frequencies and was done in the field by comparison with FMI instruments.

3.1.3 Frequency Response

The frequency response of the pancake platform was investigated to see if there was a significant effect on the measured wave height of the pancakes. This was done as data was collected on the SCALE cruise to determine the size of the pancakes, and thus the maximum wave frequency that could be measured in situ.

This was done in a wave tank setting (figure 3.1). A series of regular waves of the same amplitude (20 *mm*) with a range of frequencies (0.5 *Hz*, 0.75 *Hz*, 1.0 *Hz*, 1.5 *Hz*, 2.0 *Hz*) were used to excite the pseudo ice pancake used. The results are shown in figure 3.5.

Table 3.3: Wave parameters for frequency response investigation experiments

Experiment Description	Tm01 (s)	Hm0 (mm)	IMU	Wave Spectrum	Relative depth (kd)	Steepness (ka)	Ursell Number
Frequency response (1)	2.000	22	ICM20689	Regular	1.04	0.014	1.01
Frequency response (2)	1.333	20	ICM20689	Regular	1.89	0.024	0.27
Frequency response (3)	1.000	20	ICM20689	Regular	3.23	0.040	0.09
Frequency response (4)	0.667	20	ICM20689	Regular	7.23	0.090	0.0188
Frequency response (5)	0.500	32	ICM20689	Regular	12.86	0.26	0.0095

The waves used exceeded the steepness and depth assumptions used in section 3.1.1 as it was necessary to use a broader range of measurements. However, it should be noted that the non-linearities introduced have an impact on measurements where linear wave theory is assumed.

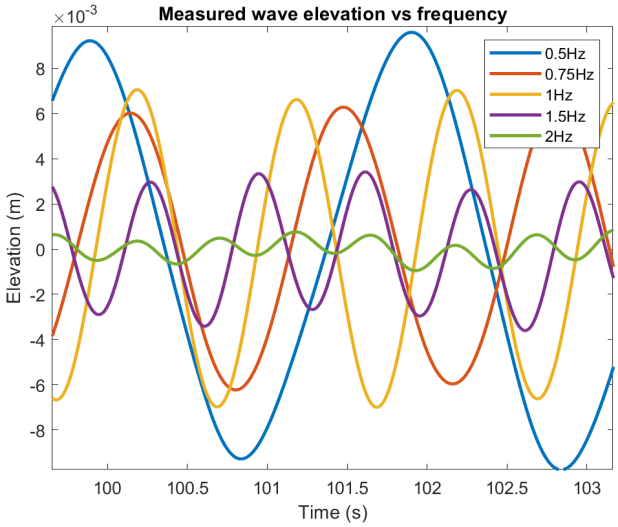

Figure 3.5: The IMU measured elevation of the pancake vs wave frequency for a series of waves with a significant wave of height of 20 *mm* generated at different frequencies.

The frequency response can be characterised by determining the response amplitude operators (ROA) measured in heave on the pancake (see section 2.2.2).

The heave ROA can be calculated as follows:

$$RAO_{Heave} = \frac{a_H}{a} \tag{3.2}$$

Where a_H is the measured heave amplitude response and a is the amplitude of the incident waves. The results were nondimensionalised by determining the ratio of the wavelength to the disk diameter.

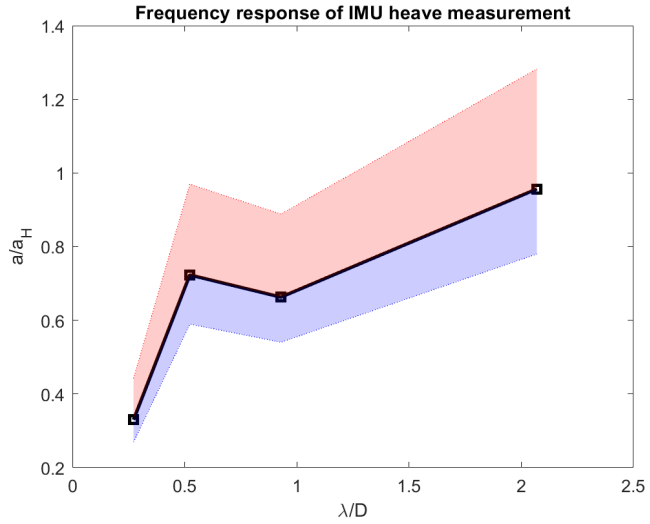

Figure 3.6: The measured frequency response of the floating disk nondimensionalised. A polynomial fit is shown.

The results from wave tank testing corroborate Yiew et al. (2017) results that the heave response approaches 1 as the wavelength relative to the diameter of the platform increases. This result is important as it shows that if the wavelength is sufficiently large relative to the ice, IMU-based measurement is accurate. The results show more variation than Yiew et al. (2017) (see figure 2.7) due to the use of regular wave as opposed to irregular, resulting in a smaller wave spectrum which is more susceptible to variance in measurement, as opposed to a larger spectrum which when integrated over will not be as susceptible to smaller variations in the spectrum.

3.2 Signal Processing Pipeline

To extract wave parameters, a signal processing pipeline was developed. The key parameters of interest are the significant wave height, $Hm0$ and the mean wave period, $Tm01$ (see subsection 2.1.4). Figure 3.7, shows the general process of obtaining wave height estimates.

The pipeline in figures 6.7 and 6.9 was used in on the embedded system of the SHARC Buoy. A pipeline utilising MATLAB's *pwelch* function was developed for use as a golden standard. The typical outputs for the reference program are shown in figure 3.7.

The pipeline follows the following process:

1. The heave raw acceleration data is recorded at 100 Hz (fig. 3.7a)
2. The vertical acceleration is scaled (fig. 3.7b). In fig. 3.7b the data is detrended for clarity. This is not necessary as the high pass filter will detrend the elevation time series.
3. The acceleration series is converted to the frequency domain (FFT) and multiplied by the response function $r(f)$ (subsection 2.5.2).
4. The response function removes low frequency trends and performs a double integration in the frequency domain. It is then converted back to the time domain (IFFT). This double integration results in spectral leakage, causing transients to be introduced at the ends of the elevation time series, these are truncated as shown in figure 3.7c, these become more pronounced the shorter the given time series is as they are the result of taking a finite record of an infinite signal.
5. The elevation time series is separated into a series of overlapping windowed segments (Welch's method). Periodogram estimates are then performed on each overlapped segment. Fig. 3.7e shows the individual periodogram estimates of the separate windows. The chi-square distribution is used to estimate the uncertainty of the spectrum (90% certainty), producing the upper and lower estimates.
6. The individual estimates are averaged and the final wave spectrum is shown. The wave parameters can be calculated by calculating the spectral moments over this time series.

The trapezoidal rule is used to integrate over the wave frequency spectrum (figure 9.6f) as in the SWASH Model (Pés 2013). Uncertainty is estimated by the chi-square distribution. The final wave parameters for the wave sample (SB06 22 July 2022 06:32 - 07:32 UTC) are shown in in table 3.4.

Table 3.4: Wave parameters for SB06 22 July 2022 06:32 - 07:32 UTC

Parameter	Result	Lower Estimate	Upper Estimate
Hm0 (m)	1.40	1.12	1.90
Tm0 (s)	13.1	-	-

For simplicity figure 3.7 excludes the correction of the acceleration to the vertical. The small angle assumption is used and heave measurement is assumed to be approximately equal to the vertical acceleration (see subsection 2.5.1). A correction for vertical acceleration is discussed in section 3.3.

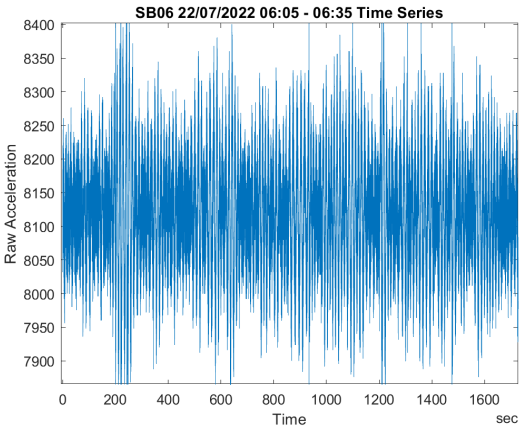

(a) Raw heave acceleration

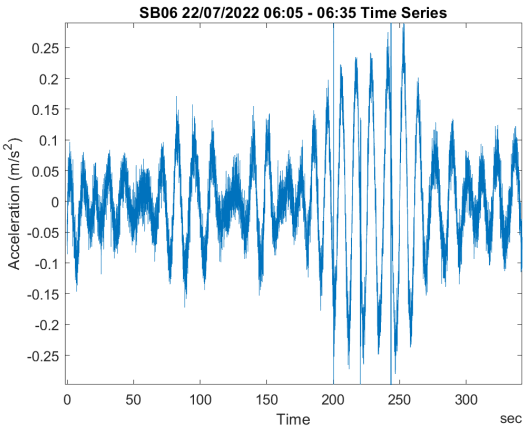

(b) Heave acceleration scaled

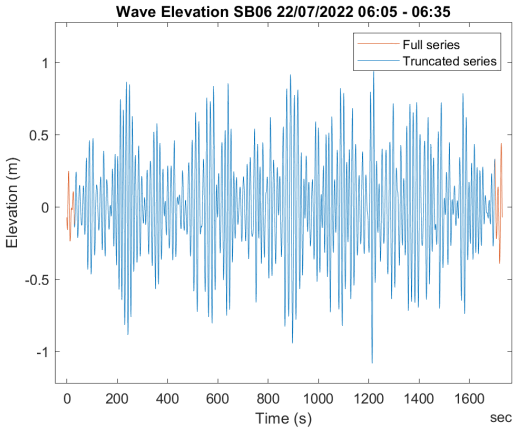

(c) Elevation

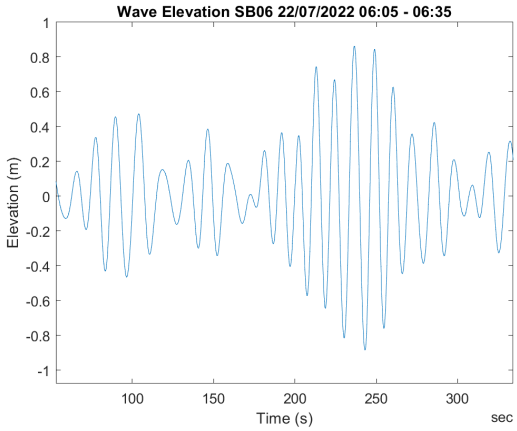

(d) Elevation zoomed

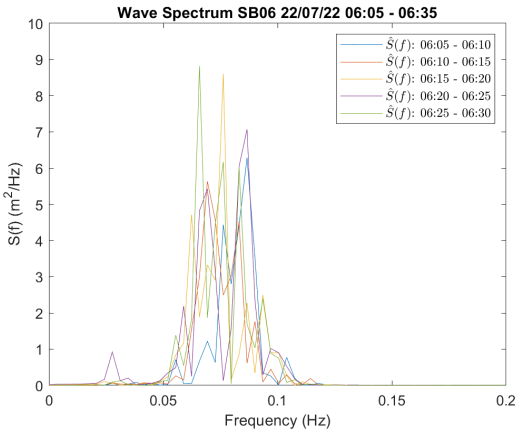

(e) Periodogram estimates

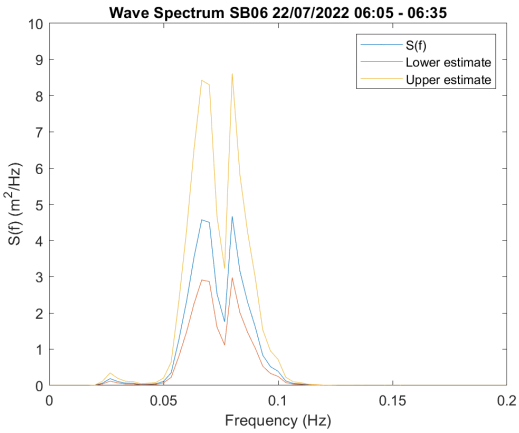

(f) Welch estimate

Figure 3.7: The signal processing pipeline used to calculate the wave spectrum ($E(f)$), measured by the SHARC Buoy. Pipeline shows processing of data collected during deployment. Two wave fields were present, resulting in a bimodal spectrum.

3.3 Correction to vertical

A correction to the vertical is needed to determine the vertical acceleration if the waves are sufficiently steep. This is shown by comparing the vertical correction in calm conditions such as in figure 3.7 above to a more extreme case (once the sensor experienced a polar cyclone). A full graph of the orientation

The orientation of the device was determined using a Kalman filter (MATLAB's *imufilter* function). Once run this filter took approximately 30 seconds to converge due to the initial estimation error. Following this, the true vertical acceleration was calculated as (see section 2.5.1):

$$\hat{\mathbf{A}}_z^i = \mathbf{g} - (sin(\theta)X_s + sin(\phi)cos(\theta)Y_s + cos(\phi)cos(\theta)Z_s) \tag{3.3}$$

From this, a comparison between the heave estimate and the true vertical is shown. On the buoy the heave was used as an estimate of the vertical acceleration as an onboard Kalman filter was not implemented. This is due to the unknown dynamics of the ice (particularly floe impacts which are prevalent in the x-y axis) and so the error introduced by the fusion of sensor data is not quantified. Thus, it was deemed prudent to use heave for in situ data processing as opposed to a filtering technique. This choice is justified by the examples shown in figure 3.8.

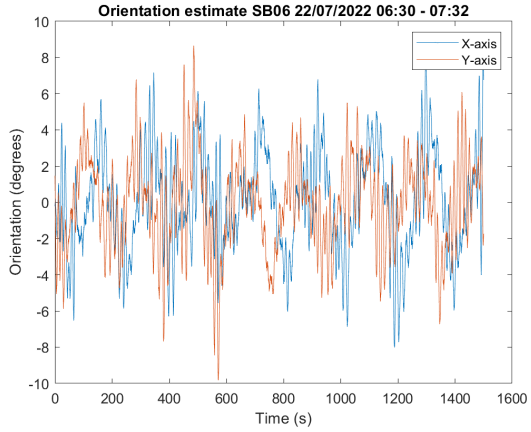

(a) Orientation in moderate waves

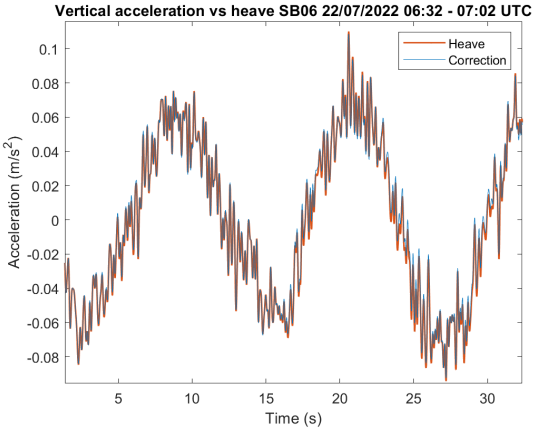

(b) Correction for moderate waves

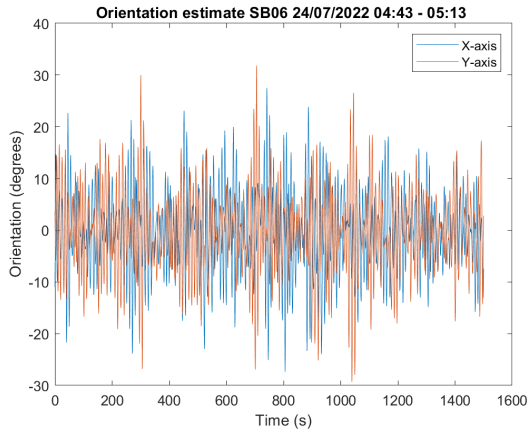

(c) Orientation for high waves

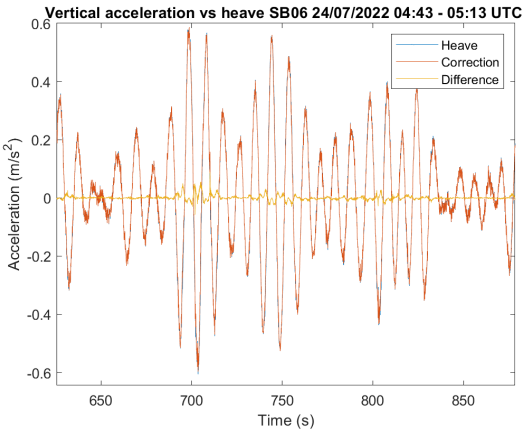

(d) Correction for high waves

Figure 3.8: Investigation of correcting vertical acceleration of buoy as opposed to using using the small angle assumption assumption

The moderate wave conditions result in orientations that do not warrant concern as non exceed

the small angle assumption. However, the higher wave conditions (figure 3.8c result in orientation values for pitch and sway that exceed the 10° threshold for the small angle assumption. However, upon closer inspection (see figure 3.8d), these errors are especially small. The root mean square error (RSME) of the high wave dataset (SB06 24/07/2022 04:43 - 05:13 UTC) was $1.5004e-17 m/s^2$! The full difference between the corrected data and the heave assumption is shown in the results section. However, the small angle assumption on the buoy is considered a reasonable assumption given the conditions in the MIZ as shown in this case study.

3.4 Stand Correction

The IMU on the buoys was deployed $\sim 90\ cm$ above the ice pancake (with variation possible due to the spikes used to keep the buoy in place). The reasons for this are discussed in section 5.1. This introduces the dynamics of the stand to the wave measurement which needs to be accounted for. Importantly the "strapped down" assumption of the IMU onto the pancake as the vertical accelerations will be multiplied by the distance of the IMU above the pancake, r.

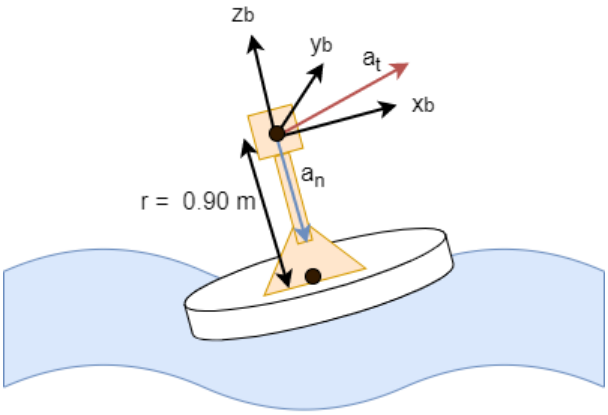

Figure 3.9: The buoy stand with additional dynamics shown. Note the reference frames will generally rotate together and so the roll and pitch angles should be approximately equivalent.

These dynamics introduced a rotational (a_n) and translational (a_t) acceleration component to the measured by the IMU placed 90cm (accounting for variation in penetration of spikes into the ice at the base of the stand) above the pancake. Given the bulk of the mass, the base of the stand is considered to be approximately equivalent to the centre of gravity of the pancake.

The corrections can be given by the following equations:

$$\mathbf{a}_p = \mathbf{a}_b - \mathbf{a}_{b/p} \tag{3.4}$$

Where the acceleration of the pancake $\mathbf{a}_p$ is given by the acceleration of the body $\mathbf{a}_b$ subtracting the relative acceleration vector of the buoy relative to the pancake. This vector is calculated as:

$$\mathbf{a}_{b/p} = \boldsymbol{\omega} \times (\boldsymbol{\omega} \times \boldsymbol{r}) + \boldsymbol{\alpha} \times \boldsymbol{r} \tag{3.5}$$

Where the acceleration of the buoy relative to the pancake, $\mathbf{a}_{b/p}$, is given by the sum of the rotational component, $a_n = \boldsymbol{\omega} \times (\boldsymbol{\omega} \times \boldsymbol{r})$, and translational component of acceleration, $\boldsymbol{\alpha} \times \boldsymbol{r}$. The angular velocity, ω and angular acceleration, α, are about the base of the stand.

The effect of the stand on the dynamics on heave measurement is negligible. The effect on surge and sway can be significant and so should be taken into account. This is shown in fig 3.10. The importance of the sway and surge correction is dependent on orientation as discussed in section 3.3 as a more substantial tilt increase the value of the surge or sway value in the vertical acceleration calculation (equation 3.3).

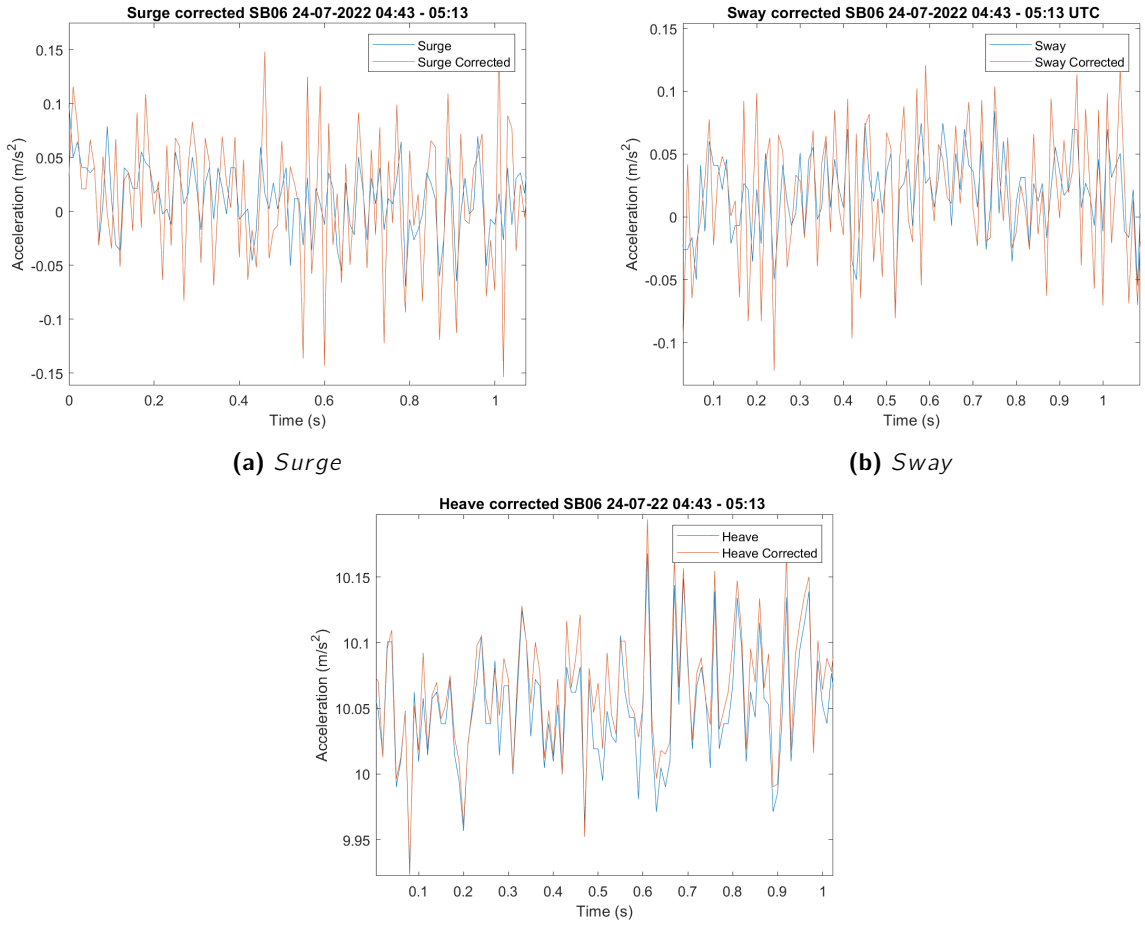

(a) *Surge* **(b)** *Sway*

(c) *Heave*

Figure 3.10: Comparison of acceleration time series for measured values and corrected values for surge, sway and heave on a small timescale (1 second) to show introduction of dynamics. Acceleration taken from longer wave time series with differences only obvious over shorter (higher frequency) time frames.

3.5 Doppler Shift Correction

The measured wave spectrum of the buoys was shifted by the drift of the ice creating a Doppler shift relative to the actual wave spectrum. To account for this a correction is applied to the wave spectra. The following equation from Collins et al. (2017) was used:

$$f_{in} = f_{obs} - \frac{g + 4\pi f_{obs} U \cos(\theta_r) - \sqrt{g^2 + 8\pi g f_{obs} U \cos(\theta_r)}}{4\pi U \cos(\theta_r)} \tag{3.6}$$

where the intrinsic frequency f_{in} is given by the observed frequency f_{obs} subtracting a correction consisting of the drift velocity U, and the relative angle between the buoy heading and the wave

direction is given by θ_r. It is necessary to assume that the drift in the buoys is induced by wind and wave forcing in the direction of the predominant drift. Thus, the relative angle, $\theta_r = 180^\circ$ as the buoy is moving away from the waves (using the 'coming from' convention). This results in a frequency downshift as the buoys drift away from the oncoming waves. This is shown for a time series from SB04 with a high drift velocity. It is noted that the correction is minimal given the typical drift of sea ice is $<<$ 1 m/s^2. Additionally, the above correction assumes that the drift relative to the waves is caused only by wind as opposed to current forcing, a worst case scenario as waves move with the reference frame of the current.

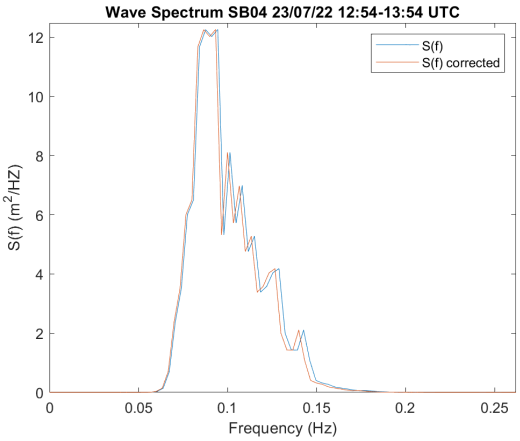

Figure 3.11: The drift of the buoys results in a Doppler shift which is shown for a high drift case for SB04 ($U = 0.21$ m/s)

3.6 Summary

The experimental setup used to validate the selected IMUs, the Invensense ICM20689 and ICM20649 was described. Using this setup, the results used to validate the IMUs were discussed with correlation between the measurements floating platform and the capacitance probes discussed. The variation in measurement caused by using a floating platform was discussed, in the particular the tendency of a floating platform to introduce *spectral spreading*. The strong correlation of measurements allowed for the validation of the ICM20649 which was subsequently integrated into the SHARC V3.0 for deployment.

A brief investigation into the frequency response of the floating platform was performed. The finding corroborated the findings of Yiew et al. (2016) that when the wavelength approaches three times the diameter of the platform, the response amplitude operator in heave approaches a unit value which is a necessary prerequisite for waves-in-ice measurement.

The method used to calculate wave spectra is outlined with an example case from data collected from device SB06.

Three potential sources of error that are introduced by the buoy are investigated. The accuracy of using the small angle assumption was shown to be acceptable in the example given. The dynamics introduced by using a raised platform (used to increase survivability) were investigated using data from SB06 during high was conditions, these were shown to predominantly affect the surge and sway measurements with this effect only being noticeable over short time frames (≤ 1 s). Finally, the phase shift introduced by drift was investigated for a high drift case from the data collected on SB06, this was shown to be relatively small but notable.

Chapter 4

Design Methodology

4.1 Project requirements

The project aimed to develop and update an existing device to collect waves-in-ice data as stated in section 1.3. To do this an updated set of requirements and specifications for the SHARC V3.0 were developed. Additionally, a series of acceptance test procedures were developed. The device was developed during an accelerated time period (6 weeks) after final confirmation of the deployment time frame. Thus, an agile methodology was used consisting of several sprints. These sprints allowed the development of an updated firmware, updated hardware (chapter 5) and an accelerated testing process (chapter 7) that allowed the devices to perform in the field.

The following sprints were performed:

1. Design and selection of the V3.0 hardware
2. Development of a high-frequency sampling subsystem
3. Development of a wave parameter extraction pipeline
4. Integration of a new MCU, IMU and GNSS into the system
5. Accelerated testing of the subsystems
6. Accelerated system level testing in the field

The requirements and specifications used to update the device during these sprints are outlined in C.1. The requirements, specifications and testing and development of the previous device is discussed by Jacobson (2021).

4.2 User requirements

The SHARC V3.0 aimed to collect waves-in-ice data in the Antarctic MIZ, this was an upgrade to the SHARC V2.0 which operated as a GPS drifter and environmental sensor. This upgrade meant that the system had to be upgraded to meet the requirements involved by collecting and processing high-frequency data reliably for extended durations in a harsh environment.

The user requirements were developed by reviewing the SHARC Buoy V2.0. The deployment of the SHARC V2.0 was successful, with the final device lasting approximately 1 week while deployed on ice in the Weddell Sea. The following issues were noted on the V2.0:

1. The MCU was prone to brownouts during the transmission of Iridium packets as the power supply (even with the addition of large capacitors) occasionally did not meet the required current draw of the Iridium modem.

2. The DuraClik connectors used between PCBs, although designed for high impact automotive applications required specialist experience to use and so were prone to connection faults.

3. The operational duration of the buoy was short (5-7 days) despite the power saving measured implemented in firmware.

Additionally, the following capabilities were desired for the new SHARC Buoy:

1. Wave measurement

2. Operational lifetime lasting the full duration of a deployment.

The SHARC V3.0 was expected to last the duration of the SCALE Winter Cruise 2022 deployment (approximately 1 week) whilst collecting waves-in-ice measurements.

An important user requirement was that the system must be cost effective as it is deployed at SCALE (7 units planned to be deployed in the SCALE Winter Cruise 2022). Thus, each unit should not be too expensive as this may restrict the number deployed.

The user requirements are outlined in table C.1 in Appendix C.

4.3 Functional requirements

To measures waves-in-ice the system needed the ability to collect acceleration and orientation measurements at a high-frequency. To provide the user with waves-in-ice measurements. these should be stored in an accessible manner for retrieval and analysis. In addition to this, the local data should be processed into summary statistics and sent via satellite, as the transmission of raw data is prohibitively expensive, to the end user for further analysis.

To meet the user requirements, the buoy will have to operate in extreme cold temperatures for 1 week. Additionally, it will have sufficient memory to store the high-frequency IMU measurements. These measurements will need to be stored in an organised file system in external memory to allow the retrieval of the data, or for the firmware to perform an in situ analysis.

To perform the in situ analysis, the system must have the ability to perform DSP operations on large datasets.

The battery capacity must also be increased to last the operational duration of the deployment, taking into account the increased power consumption as a result of the wave sampling and pro-

cessing.

Finally, the system is operating in an extreme environment, on large datasets. Therefore, it should have the ability to recover from an unexpected firmware fault and continue operation. Furthermore, if the power supply becomes unstable or fails unexpectedly, even while the buoy is actively reading or writing to the memory, the memory should retain previously sampled data.

The full functional requirements are in sections C.1.2 and C.1.2 in Appendix C.

4.4 Specifications

The buoy hardware was updated to include an updated 6DOF IMU (3DOF accelerometer, 3DOF gyroscope), first the Invense ICM20689 (InvenSense 2021*b*) and then the ICM20649 (InvenSense 2021*a*) which was capable of sampling 6DOF at 100 Hz to with error characteristics capable of measuring waves-in-ice (see section 5.3.1). In addition the IMU was capable of operating reliably within the desired temperature range (extreme cold operation in temperatures of up to $-40\ ^{\circ}C$).

The power supply should be increased from 20 Ah to $\geq 50\ Ah$, to meet the power consumption requirements of the buoy. The buoy should last at least one week with the worst conditions assumed with additional redundant capacity. The SHARC V2.0 operated for approximately 1 week with an average current draw of 100 mA when not in sleep mode. The updated buoy would have an increased current draw as a consequence of sampling the IMU at high-frequency for a 30 minute sampling period with an additional data processing period after sampling. Additionally, the device will be expected to operate continuously during operation as it will be deployed into storm conditions of interest. In addition the power supply should be able to provide 2 A maximum current to meet the current draw requirements of the Iridium modem which will transmit twice as often. A highly conservative 50% derating of the batteries is done to assume the worst conditions for a lithium battery based on the standard derating for polar instruments (Doble et al. 2017).

Table 4.1: Operational duration estimate

Individual battery capacity (Ah)	14
Individual voltage (V)	3.6
Number of batteries	8
Number in parallel	4
Number in series	2
Total battery capacity (Ah)	56
Derating (%)	50
Derated capacity (Ah)	28
Average device current consumption (mA)	130
Estimate operational duration (days)	approx. 9 days

The chosen MCU should be able to perform DSP operations on large datasets. Therefore, it requires sufficient RAM memory ($\geq 150\ kB$). The MCU should have access to efficient libraries that are able to perform DSP operations (FFT, FIR filtering etc.) on the chosen chip. In addition the MCU should have a floating point unit (FPU) to make development of the DSP pipeline easier.

The external memory should have sufficient capacity to store the IMU logging 6DOF at 100 Hz for 2 weeks. It should support the FATFS library (ChaN 2023) to allow the organisation of the sampled data for access and retrieval. The data should be stored in timestamped logs with separate files for each log.

The wired connections between separate PCBs should be replaced by a PCB stack joined with

male to female headers to prevent the mechanical failure of the electrical connections. This should additionally help the device to survive the mechanical shocks resulting from ice floe impacts, deployment onto the ice and high winds.

The communication interface for the IMU should be an I2C interface running in fast mode (400 kHz) with errors resulting in a reset of the I2C interface. The external memory should make use of an SDIO/SDMMC interface as it is more reliable (as it has custom circuitry) than the SPI SD interface. The data should be stored using FATFS with separate folders for each sensor log. The IMU data should be partitioned into individual files within each 30-minute log to prevent the loss of a full log in the event of an error encountered during the reading from or writing to a log file.

The CMSIS DSP library for ARM MCUs will be used as it is efficient and operates in the MCU hardware. The 32-bit point floating point operations will be used in the pipeline.

In the event of a system response the system reset function will be triggered by the nested vector interrupt controller (NVIC) on the ARM MCU and the firmware will resume operation.

The specification are outlined in sections C.1.3 and C.1.3 in Appendix C.

4.5 Acceptance test procedures (ATPs)

Before the deployment of the buoys several ATPs were performed to ensure the operation of the systems would be reliable.

Firstly the high-frequency logging subsystem will be operated for a duration of 12 hours in a freezer. The collected data will be analysed to see if data corruption occurred during logging.

The assembled buoy will be tested in an accelerated setup with shortened wave sampling intervals to determine if memory storage and logging was reliable. In addition, the Iridium transmission should be tested in the accelerated testing to determine if the system has a robust power supply able to provide the maximum current draw required during transmissions over an extended duration. This should be done in a cold environment ($\leq -10°C$) over a period of at least 12 hours.

During testing the power supply should be switched off during read and write operations and the stored data analysed to see if the filing system has been corrupted.

Each SHARC Buoy V3.0 should run several sampling intervals before deployment, with transmissions and stored data analysed for validity.

Finally, firmware faults should be intentionally created to trigger a hard-fault error (an error after which the firmware cannot recover) on the system. The system response should be an automatic reset of the firmware and re-entry into the RESET state.

The specifications are outlined in sections C.2 in Appendix C.

Chapter 5

Hardware Development

The hardware on the SHARC V3.0 was updated to allow for continuous operation and high frequency IMU logging. Previous hardware issues such as faulty connectors were revised and the power supply was updated to increase the operational period of the devices. The updated user requirements, functional requirements and specifications for the hardware are provided. The hardware subsystems are then discussed individually.

5.1 Mechanical Design

The SHARC Buoy V3.0 was larger than the V2.0. This was due to the larger size of the power supply and embedded system on the buoys. The use of the Nucleo-144 package (STMicoelectronics 2023) on the buoy resulted in a larger diameter for the enclosure (see size comparison in fig. 5.2) as the development boards were used on the device to shorten development time as opposed to using a custom embedded system. The stand was designed to endure the environmental conditions of the Antarctic MIZ by elevating the system above the ice surface which is susceptible to overwash from ocean waves and freezing into the ice as a result of ice production on the top of ice pancakes.

(a) *V2.0* **(b)** *V3.0*

Figure 5.1: Changes in stand design between SHARC Buoy V1.0 and V3.0 Design credit: V2.0 Keith MacHutchon, Robyn Verrinder, V3.0 James Hepworth

Table 5.1: Comparison between the SHARC V2.0 MCU and the V3.0 MCU

MCU	Flash (MB)	SRAM (kB)	FPU
STM32L476RG	1	128	Yes
STM32L4R5ZIT6P	2	640	Yes

5.2 Embedded System

The embedded system hardware was updated with several upgrades. The primary upgrade being from the STM32L476RG MCU (STMicroelectronics 2019) to the STM32L4R5ZIT6P MCU (STMicoelectronics 2020). The primary reason for this was the increased RAM and flash memory available on the devices. This was particularly important for handling the large arrays of data used by the wave parameter extraction program running on the buoy. The increased flash memory size allowed for a larger firmware size, which was needed to incorporate the new GPS driver.

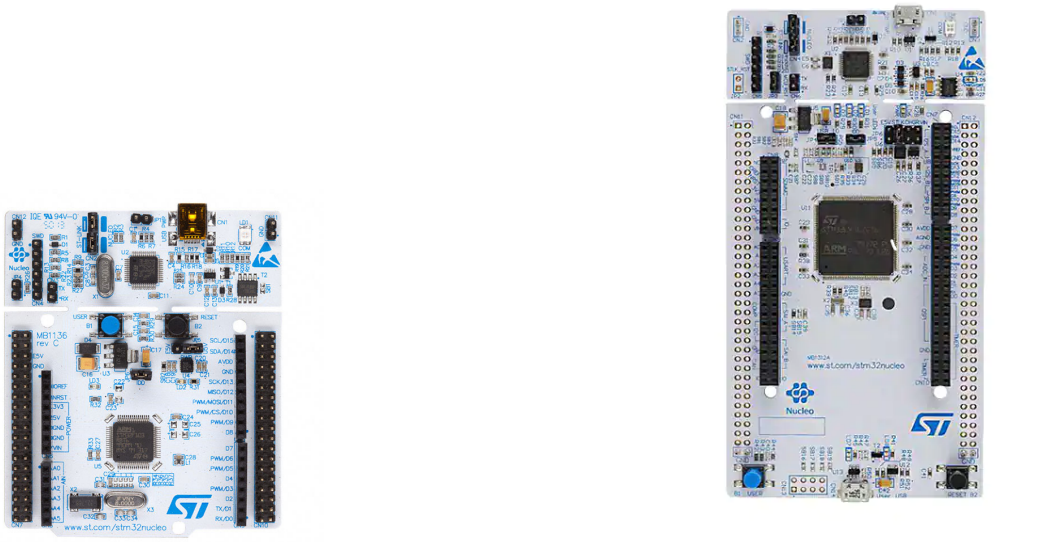

(a) *STM32L476RG* Nucleo-64 **(b)** *STM32L4R5ZIT6P* Nucleo-144

Figure 5.2: Comparison of the STM32 Nucleo-64 and Nucleo-144 development boards used in the individual packages. Image credit: STMicroelectronics

The second upgrade was to the memory on the system. Previously flash chips had been selected for their reliability. However, the memory size of the chips was too small to be used for storing long time series. They were replaced by SD cards. Industrial SD cards were chosen as they could function reliably at low temperatures. Commercial SD cards generally function down to a temperature of -20°C whilst industrial SD cards function at temperatures of -40 °C. This is due to the differences in the NAND flash memory used on SD cards, with industrial cards using more reliable single level cell (high cost, high reliability) or multilevel cell (lower cost, high reliability) in comparison to triple-level cell generally used in commercial chips which has a poorer temperature performance and lower reliability.

A 16 *GB* ATP industrial SD card (ATP Electronics 2017) was chosen as it had the appropriate temperature range for the Antarctic winter. The performance of the SD card was confirmed in testing (see chapter 7).

The size of the SD card was determined by the sampling rate over the operational duration of the device. This was an important consideration as industrial SD cards are about a factor of 10 more expensive than commercial SD cards. The main use of memory was the storage of the 6DOF IMU data. The deployment was expected to last 5-7 days. The sampling rate of the IMU was 100 Hz and it was assumed to operate continuously during the period. Each raw value was stored as a 32 bit integer on the SD card. For a one week deployment this could result in a maximum of 12 GB of data and so a 16 GB memory card was sufficient.

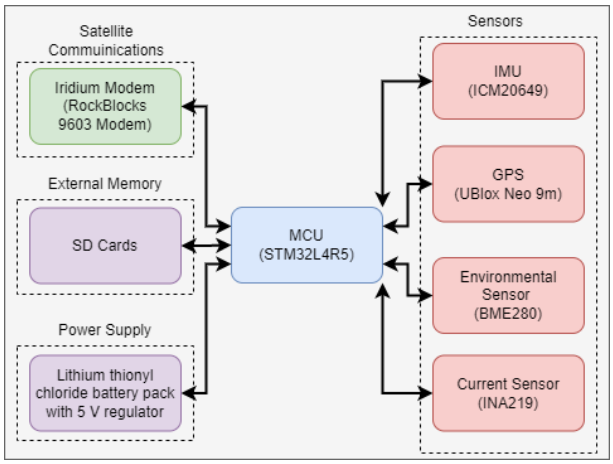

Figure 5.3: The updated embedded system for the SHARC V3.0

5.3 IMU

The IMU used on the SHARC Buoy V1.0 and V2.0 was the Invensense MPU6050. This IMU has been deprecated. The successor model was the ICM20689. This was used for wave tank testing in 2021. Due to the component shortage, the ICM20689 was not available in 2022 and the replacement selected was the ICM20649. A comparison of the IMUs is given in tables 5.2 and 5.3.

The onboard IMU was validated by verifying the reliability of the IMUs both at room temperature and at -20°C (see section 7.1.5).

5.3.1 Error characteristics

Specifications

The IMU selection was considered based on the error characteristics and specifications of the devices. The initial selection of the ICM20689 was due to the cost effective and relatively high accuracy of the IMU in comparison to high cost devices such as the VectorNav VN100 (VectorNav 2020) or the XSens MTi-100 series (XSens 2020) which cost in the range of $ 800 - 1200 USD (R14000 - R22000 @ R17.95/USD) which is similar to the cost of a full SHARC Buoy (approximately R 20000).

Thus, to deploy multiple instruments, it was preferable to use a more cost effective IMU. To select this device the error characteristics were assessed. The most important characteristics are the accelerometer error characteristics in heave with the gyroscope characteristics being important for the accuracy of sensor fusion in determining the orientation of the IMU.

The IMUs were first determined to have sufficient bandwidth (for a sampling rate of 100 Hz) and full-scale range (waves are in the region of $< 1\ m/s^2$ with other phenomena of interest such as

floe-floe collisions being up to 4 g). Following this the noise density was reviewed to see if it would be too high relative to small wave heights. Finally, the temperature variation was determined to be sufficiently low so as to not bias the wave measurement.

The heave measurement of the VectorNav VN100 is quoted as within 5% or 5 cm (VectorNav 2020). This reference is used as to what a reasonable expectation for accuracy for cost effective sensors should be. The total error as a result of noise and the variation as a result of temperature is analysed below.

Table 5.2: Accelerometer characteristics

Accelerometer Specification	**MPU6050**	**ICM20689**	**ICM20649**
Noise Density ($\mu g/\sqrt{Hz}$) (@ 10 Hz)	400	150	289
Sensitivity Change vs. Temperature (%/°C)	+/- 0.02	+/- 0.016	+/- 0.026
Initial Calibration Tolerance (%)	+/-3	+/- 2	+/- 0.5
Full Scale Range (g)	2 - 16	2 - 16	4 - 32
Bandwidth (Hz)	4000	4000	4500

Table 5.3: Gyroscope characteristics

Gyroscope Specification	**MPU6050**	**ICM20689**	**ICM20649**
Noise Density (°/$s/\sqrt{Hz}$) (@ 10 Hz)	0.005	0.006	0.0175
Sensitivity Change vs. Temperature (%, $[-40, +80]°C$)	+/- 2	+/- 2	+/- 2
Full Scale Range (°/s)	250 - 2000	250 - 2000	500 - 4000
Bandwidth (Hz)	8000	8000	9000

5.3.2 Noise analysis

The noise floor of the IMUs determined the minimum possible wave height that could be measured by the system. This was determined by placing the IMU on a stable surface for a 4-hour duration and measuring the noise characteristics for the given configuration (100 Hz, 4 g range) The power spectrum of the noise was taken for the heave axis. The noise was then integrated by multiplying the noise power value by $(2\pi f)^{-4}$ to integrate the noise from acceleration to displacement (Rabault et al. 2020, Alari et al. 2022).

The error was found to be high at the lower frequencies. Applying the high pass filter used in the double integration revealed the noise "height" to be approximately 5 cm at the lowest measured frequency (0.03 Hz), as a result of using a lower cost IMU). However, the noise decreased exponentially to 12 mm at 0.04 Hz which was the lower end of the frequency range in the measured wave spectra from the deployed buoys. At the dominant frequency range of approximately $0.06 - 0.08$ Hz, the noise height was less than 3 mm.

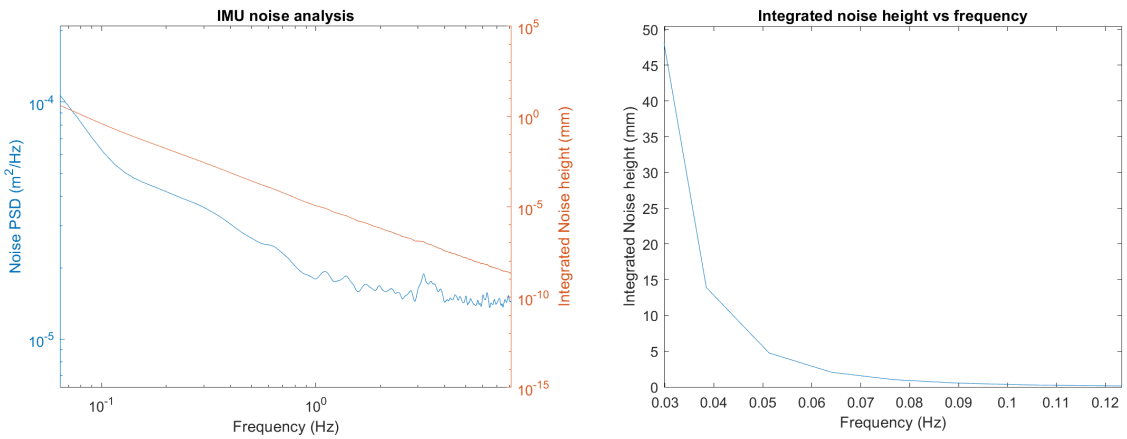

(a) Noise PSD **(b)** Noise height

Figure 5.4: Noise floor analysis for the ICM20649

The ICM20649 had a significantly higher noise density than the ICM20649. However, this is a result of the sensor being designed to withstand and measure impacts in a sport setting. This proved to be advantageous as it was able to measure the floe collisions during the deployment period without saturating whilst functioning reliably.

An additional reason to characterize the noise of the IMU is to determine that "spurious noise" is not affecting the wave measurement at different frequencies (Thomson et al. 2021). In particular high frequencies ($f \geq 0.5\ Hz$), where the noise of the instrument may increase the measurement of waves at high frequencies. If any high frequency wave measurements approach the noise floor above, they should be viewed with suspicion.

5.3.3 Temperature variation

The error caused by temperature variation on the IMUs is another parameter of concern. The MEMS system on the ICM20649 is temperature sensitive and so a characterisation of the error at low temperatures is necessary.

The quoted accelerometer sensitivity change vs temperature is 0.026 $\%/°C$ (InvenSense 2021*a*). At $-20\ °C$ this would correspond to a 1.04 % and to a maximum of 1.56% at the extreme temperature range of $-40\ °C$. For an expected waves-in-ice measurement value of 0.1 m/s^2, this would correspond to a measurement error of 0.00104 m/s^2 at $-20\ °C$. At an expected wave period of 0.1 Hz, this corresponds to a displacement measurement error of 3 mm. At lower wave frequencies the error becomes more pronounced ($\sim 1\ cm$ for the above case at 0.05 Hz). However, at the dominant wave frequencies and heights, the error due to temperature is minimal.

Figure 5.5 shows the displacement error caused by temperature for two acceleration values typical of the higher and lower end of measured waves in ice values (0.05 m/s^2 being the lower end and 0.1 m/s^2 being the upper end). At extreme temperatures $-\ 40\ °C$ and low frequencies ($< 0.05\ Hz$) the error is significant relative to the measured wave height. However, the temperatures experienced during deployment (see section 9.4) were less than $-12\ °C$. This resulted in a maximum error of $\sim 2\ cm$ at 0.03 Hz which is lower than the noise floor (see temperature graph in subsection 9.4).

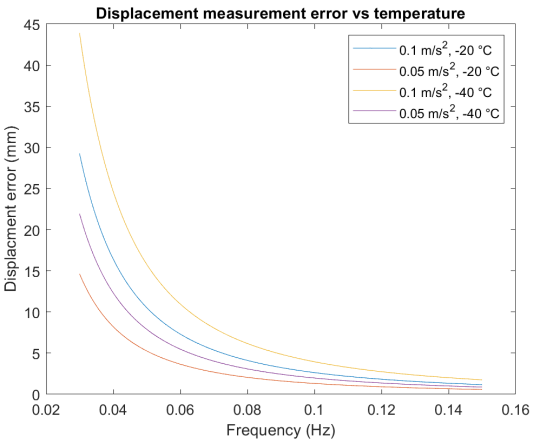

Figure 5.5: The displacement error caused by temperature variation on the MEMS based ICM20649.

5.4 GPS

The previous GPS selected for the SHARC V1.0 and V2.0 was the UBlox Neo-7m. This device has since been deprecated. The successor NEO 9m (ublox 2022) was chosen. Both were run in continuous mode. This indicates that the GNSS (Global Navigation Satellite System) device was kept on to reduce the lock on time and the potential to not get a fix. The continuous operation was allowed by the increased battery capacity discussed in section 5.5.

5.5 Power Supply

A key limitation in cold environments is the need to derate the capacity and voltage provided by batteries. Conservatively, the voltage and capacity of batteries in polar environments is generally derated by 50% (Doble et al. 2017). This may be too conservative in some environments. However, it functions as a good guideline. There are two approaches to this problem. Firstly, to reduce power consumption, which has already been done on the buoy by including introducing sleep states and selecting low power electronics (MCU, IMU and GPS). Secondly, to increase the battery capacity.

Another consideration was the changing characteristics of the cells due to temperature. Lithium thionyl chloride batteries were selected for their high capacity and temperature tolerance.

- A high voltage (3.6 V) which remains highly stable during the operational lifetime of the battery
- Able to withstand low temperature operation
- High capacity relative to size (14 Ah)
- Low self-discharge rate

More specifically the Minamoto ER34615M lithium thionyl chloride cells were selected (Minamoto 2022). The stainless steel housing of these batteries offered additional protection from environmental corrosion.

The batteries were configured into a 4 by 2 cell array with 4 parallel sets of 2 cells in series. This resulted in a 7.2 V battery pack with a capacity of 56 Ah. This was significantly higher than previous SHARC Buoy which used 4 lithium thionyl chloride cells with a lower capacity.

The voltage regulator and power management board circuit was designed to have an initial soft start to prevent an initial inrush current.

The batteries were tested in accelerated testing outlined in chapter 7.

Chapter 6

Firmware Development

The firmware for the SHARC V3.0 was based on the firmware developed for SHARC V2.0. In this regard it used the STM32 hardware abstraction layer (HAL) and a modified version of the original firmware. However, it included high frequency IMU logging and a wave parameter extraction algorithm which calculated wave statistics based on the raw IMU data stored on the buoy.

6.1 System Overview

6.1.1 System Architecture and Overview

The integration of a larger external SD memory system as well as the onboard processing necessitated by the wave parameter extraction algorithm meant that new hardware capabilities were needed. A brief overview was given in chapter 5.

The main considerations were the need to perform power spectral estimates from the collected time series and the ability to sample an IMU at high frequency.

The firmware was updated from V2.0 by simplifying the firmware state machine. This was done as the increased battery capacity allowed for continuous operation over the course of the SCALE winter 2022 deployment. This meant that intermittent operation with sleep periods was not required and so the system functioned continuously. This was useful as the entire period of operation was of interest and so increasing the time over which sampling occurred was a priority, provided the power supply could sustain continuous operation.

The updated and simplified algorithmic state machine (ASM) used for continuous operation is shown below in figure 6.1.

The SHARC Buoy V3.0 operates as follows (R_x indicates routine x):

1. R_{reset} : The buoy is initialised in a reset state . This state functions as an entry and debugging point for the program.

2. R_{smple} : The buoy begins a sampling period of 30 minutes

3. R_{TX} : A transmit state begins with a processing period to extract wave parameters. Upon completion of the processing period, the processed data is sent via Iridium link.

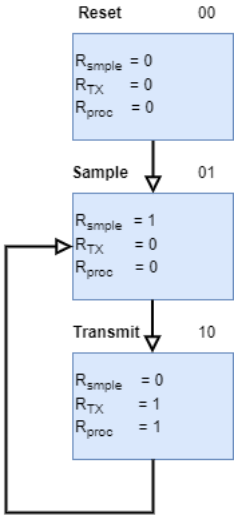

Figure 6.1: Updated Algorithmic State Machine for the SHARC Buoy V3.0

The sampling period on the buoy consisted of the following process:

1. GPS location fix determined (1)
2. Environmental temperature and pressure sampled (1)
3. IMU sampling period of 6 contiguous 5-minute sampling periods (30 minute total)
4. GPS location fix determined and logged (2)
5. Environmental temperature and pressure sampled (2)

This is depicted in figure 6.2. The structure of the sampling period was based on the following considerations. The sampling of wave activity is susceptible to the Doppler Effect as the device is not fixed to a particular location during measurement (see 2.2.3). This necessitates the determination of GPS location both before and after the wave measurement period so that an estimate of the velocity of the buoy can be determined and an interpolation of the location. The environmental measurement was taken at both points to increase the sampling period of these parameters.

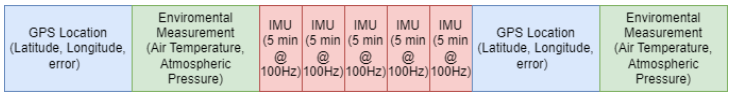

Figure 6.2: Structure of the sampling period.

6.1.2 Hardware Abstraction Layer

The hardware abstraction layer (HAL) on the STM32 devices continued to be used. The HAL drivers for communication to the external interface, interrupts (NVIC - Nested Vector Interrupt Controller) and real time clock (RTC) module.

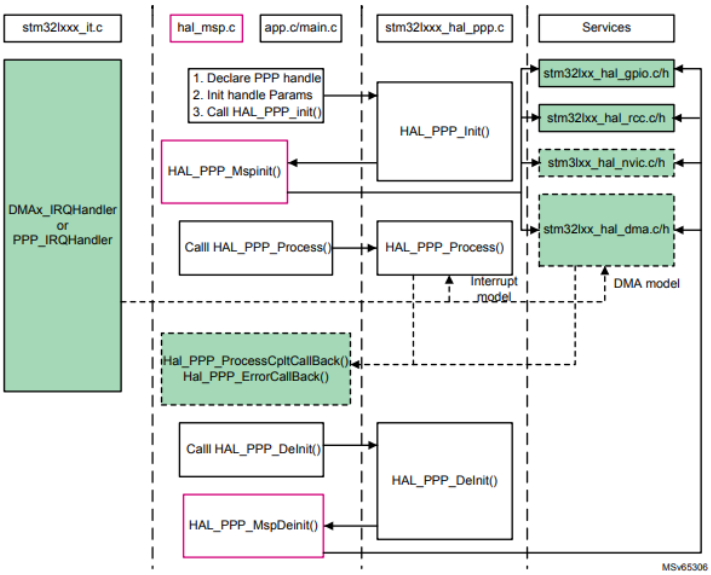

Figure 6.3: Structure of the STM32 HAL

6.1.3 Digital signal processing

The digital signal processing on the embedded firmware was done using the CMSIS DSP library. CMSIS (Common Microcontroller Software Interface Standard) is an abstraction layer for ARM MCUs. The CMSIS DSP library was used for signal processing on the buoy as it contained functions that were optimised for the ARM Cortex M4 processor on the STM32L4R5. It is important to note that these functions are limited in size (256, 512 or 1024 elements) with the number of elements being constrained to power 2 values to improve the efficiency of the processing.

6.1.4 Toolchain and Firmware Version

The firmware used on the buoy made use of global variables, which is a legacy from the V1.0 and V2.0 of the buoy. V3.0 still makes use of global variables and so uses GCC9 toolchain.

6.1.5 Conversion between STM32L4 and STM32L4R5

The primary difference between the STM32L476RG and the STM32L4R5 is the size of the RAM (random access memory) and the flash memory. Thus to port the firmware between the previous and current version the linker scripts must be updated to reflect the changed memory sizes.

In particular, the minimum stack size had to be increased for the DSP. The maximum size array that was operated on was 1024 floating point array. This necessitated the stack size to be increased to $\sim 20\ kB$.

6.1.6 Error Handling

The processing of large arrays of data on the MCU meant that memory leakage or segmentation faults were a possibility. Memory faults typically result in a hardfault on the system. This was accounted for by resetting the system with the Nested Vector Interrupt Controller (NVIC). In such a case the system would re-enter the state machine in the reset state. Thus, if a stack overflow, memory leak or segmentation fault occurred the system would reset and continue to function.

6.1.7 Memory management

Limited memory required decisions to be made about the way data was processed in RAM. To maximise the available memory arrays were preferably declared *locally* in functions. This results in the automatic allocation of memory on the stack when the function is entered, releasing the memory when the function execution is complete. An input and output array were passed to each processing function by reference. The use of local arrays was possible as the length of the arrays were fixed for the duration of their lifetime as the length of the FFT operation (1024). It was not necessary in this case to use dynamic memory allocation for the signal processing pipeline. This reduces the chance of failed memory allocation due to the lack of available heap memory or memory fragmentation. This is a concern for the long operation of the embedded system as there is no resetting of the system (in the ideal case), and so may reduce the reliability of the system over time, eventually resulting in a segmentation fault.

Additionally, the GPS driver utilised dynamic memory allocation out of necessity as the *NMEA* strings are of variable length which is not known ahead of time. Thus, to reduce the potential interaction between the GPS driver's memory usage in the heap, the DSP pipeline was processed in the stack memory.

The STM32L4R5 has 3 RAM memory partitions: RAM (192 kB), RAM2 (64 kB) and RAM3 (384 kB). In the C language, variables or variable sections cannot be split over multiple RAM partitions. Thus, the full program is located in the largest RAM (RAM3) and this is updated in the linker script. To simplify development, a single RAM partition is used. If desired, more RAM can be utilised to allow for a larger stack or heap for future development.

6.2 Subsystems

6.2.1 Inertial Measurement Unit Interface

Initially, the IMU MCU communication was designed to use DMA transfer. However, the I2C (inter-integrated circuit) DMA program on the STM32 HAL did not function reliably. As a result a polling interface was used. This interface functioned reliably in testing and so was used for the final system. It had the disadvantage of using the processor resources during the duration of the IMU sampling period.

6.2.2 External Memory Interface

The system utilised high capacity industrial SD cards. To store and access data in a logical manner, the File Allocation Table (FAT) file structure is included in middleware. The middleware is based off FatFs system(ChaN, 2023).

To use FatFs with an SD card, low level drivers need to be instantiated in the firmware. A file structure was created for the data with separate files and subfolders created for each sensor system.

The disadvantage of running FatFs on SD cards is if there is an interruption of a read or write process the resulting file will be empty. Therefore to reduce the potential for data loss, several files were created for each sampling instance.

Another concern for reliable data logging is that if a write operation is interrupted, the entire FAT on the SD card can become broken. This requires the careful use of interrupts on the system. Thus, all interrupts were disabled before the SD I/O operations were performed.

The sampling method was as follows:

1. Mount SD card and open file for sampling period
2. Write data to file as it is acquired through the duration of sampling period
3. Close file at end of sampling period
4. Dismount SD card

A driver was developed to read and write to the file system. The driver handled the file operations of opening, closing reading and writing to individual files for ease of use.

6.2.3 GPS Interface

The GPS interface operated continuously. This has the significant advantage of reducing the potential lock on time resulting from a cold or warm GPS start. This delay would likely result in increased error in location measurement or in the worst case result in no location measurement as the GPS was not able to determine a fix at the time the measurement is requested.

The driver was configured to continuously log the GPS NMEA strings in a circular buffer. This was done using DMA interrupts using a UART interface. At the moment that the data was requested by the main program, the most recent data in the buffer was used as the location measurement. Careful use of the interrupts was performed so as to not occur simultaneously with the read/write of the SD cards.

The driver was in the region of 1 MB. This necessitated the use of the larger flash memory on the STM32L4R5 (2 MB).

6.2.4 Iridum Interface

The Iridium interface functioned by sending AT commands (Iridium 2014). These are simple text commands used to interface or send instructions to the modem. The interface was tested by verifying that the interface responded to the necessary AT commands. The commands were sent on a UART interface. The length of the transmission was in the region of 100 bytes. The structure of the Iridium packets used for the deployment are shown in Appendix F. The general format for wave logging consisted of a drift log storing GPS and environmental data, followed by wave data followed by a second drift log sampled after the wave measurement so that Doppler shift could be accounted for.

6.3 Operational Modes

6.3.1 High Frequency Sampling Mode

The high frequency sampling mode was developed for the Targeted Observational Experiment (TOE) proposed for the SCALE cruise 2022. The system needed to be able to reliably collect and store a high frequency inertial time series.

This was done by polling the IMU for six five-minute consecutive sampling periods (30 minutes total). Following this sampling period, the signal processing pipeline (section 6.4 would run to calculate the summary wave statistics by reading in the IMU data recorded on the SD card.

An implementation of non-blocking communication was developed using the direct memory access controller (DMA)) on the STM32. However, it did not function reliably. Using the HAL DMA implementation allowed for data to be recorded without blocking the CPU for the duration of the sampling period. However, using the DMA for the IMU I2C communication to a buffer in memory

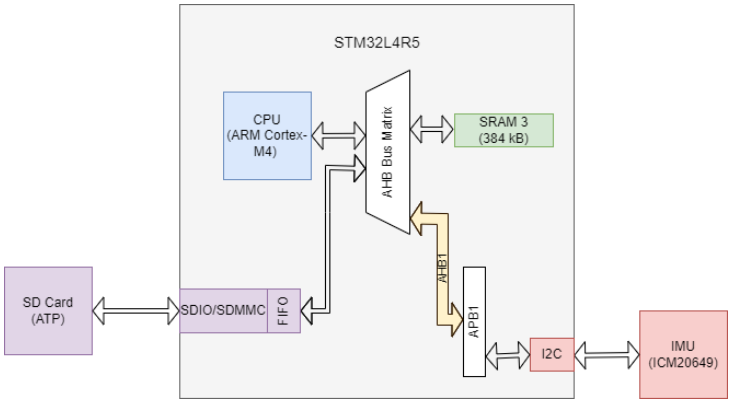

Figure 6.4: Block diagram of the STM32l4R5 showing the internal components involved in the high frequency data transfer.

(peripheral to memory transfer) followed by transferring this buffer to a file on the FAT on the SD card, using the DMA to control the SDMMC communication (memory to peripheral), resulted in unreliable results that may have to do with known issues in the low-level I2C drivers.

An additional concern was triggering interrupts for memory transfers regularly whilst writing to the SD may result in the corruption of the FAT volume on the SD card. This would result in the loss of all data collected to the point at which the error occurred. Thus, for reliability a polling interface was used (figure 6.4).

When the sampling period was concluded the current log and directory number was stored in the RCC backup registers to allow sampling to continue in order in the case of a brownout.

The sampling method for the IMU is shown in figure 6.5. The effective sampling rate on the SHARC Buoy devices was 104 Hz. This was the result of an integer rounding error in the calculation of the sample rate divider register (SMPLRT_DIV) in conjunction with the synchronisation between the accelerometer and gyroscope done by the output data rate synchronisation function (ODR_SYNC register). This was corrected in the firmware after retrieval and the processing accounted for the change in sampling rate which was easily determined using the timestamps in the data.

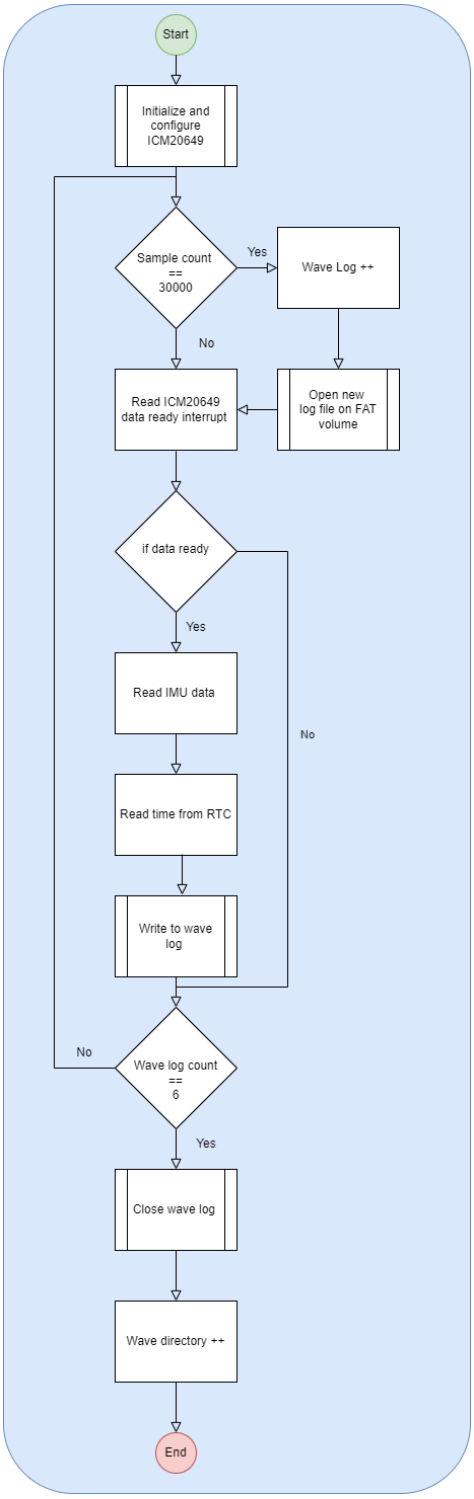

Figure 6.5: Flow diagram showing the process for recording and storing the IMU data using SD cards. A 30 minute sample is recorded by storing six five minute wave logs of 30000 samples each.

6.4 Signal Processing Pipeline

The signal processing pipeline on the buoy followed the structure specified in figure 6.7 and 6.9. The main difference between the onboard processing and the processing in MATLAB was the constrained memory of the STM32L4R5. The constrained memory meant that the processing

pipeline needed careful consideration. The pipeline was done using floating point arithmetic, this is less efficient than fixed-point alternatives. However, it significantly simplifies the development of the pipeline at the cost of a loss of efficiency.

The raw data was stored in external memory in text files. This data was then read in. Note, that it would be significantly quicker to use binary files (this was not done due to short development time). Specifically the heave data (z axis of accelerometer) was read in (see subsection 3.3). The data was read in as segments the length of the FFT operation (1024) and pre-processed by scaling and detrending the measured heave data. The scaling coefficient was determined from the ICM20649 specifications (InvenSense 2021*a*), with finer corrections using collected calibration datasets also possible.

The primary consideration is the maximum length of the FFT that can be performed on the MCU. In this case the maximum length FFT that can be performed on the cortex M4 with the floating point unit (FPU) enabled using the CMSIS DSP library on the ARM Cortex M4 is 1024. Thus, the raw stored data must be decimated and low pass filtered (to remove the higher frequency harmonics) to fit the constrained length. This is done using a finite impulse response (FIR) filter and decimation function *arm_fir_decimate_f32()*. The function implements the FIR filter using a series of multiply and accumulate operations. This implementation requires the calculation of the filter coefficients which is done using MATLAB's *fir1()* function.

The acceleration data is decimated by a factor of $M = 16$ (chosen as 1024 is an integer multiple of 16) and so the filter was designed such that the cutoff frequency would be less than half the decimated sampling frequency of 6.25 Hz in order to meet the Nyquist sampling criterion. It should be noted that the frequency cutoff ($f_{cutoff} = 1.12$ Hz) is still significantly above the expected frequency range of wave activity in the MIZ. The decimated segments (16 in total) are then concatenated into a wave sample of $n = 1024$. This sample has a duration of 163.84 s, which is sufficient to capture wave information considering that the high pass filter used removing drift when integration the data (see figure 6.6) sets a cutoff of $f_{cutoff} = 0.03$ Hz, corresponding to a period of approximately 33 seconds. For the final filter the decimation factor was increased to $M = 32$ (for an sampling rate of 3.125 Hz) which was allowed by the increase from 30 000 to 32 768 samples per segment, allowing each segment to be 327.68 seconds. The examples segments shown here will be 163.84 s, (as in the firmware deployed on the SCALE Cruise 2022 logged 30 000 sample segments). However, the final pipeline will calculate statistics based on 327.68 second segments.

The decimated data is then detrended using a RC high-pass filter implemented in software. The filter followed the design of Tucker & Pitt (2001), Kohout et al. (2015) and had a time constant of 100 s, which is the lowest value that should be used. This value is chosen to ensure the 163.84 s segments are detrended (that the low frequency drift is removed). The filter constant k is calculated using:

$$\frac{\Delta t}{1-k} = 100 \tag{6.1}$$

Where Δt is the sampling period and k is the filter constant. With a sampling period of $1/6.25 = 0.16$ s and a time constant of 100 s, the filter constant used is $k = 0.9986$.

After the detrending operation, the preprocessed acceleration is transformed into the frequency domain using a 1024 point FFT and multiplied by a high pass filter and double integration response function (see subsection 2.5.2). The high pass filter removes the low frequency drift from the series and it is also double integrated from acceleration to displacement. As this operation is performed

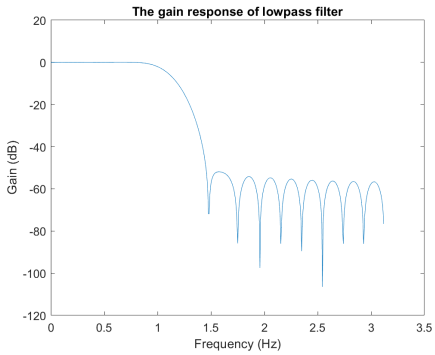

Figure 6.6: Gain response of the FIR implemented on the buoy. Cutoff frequency chosen to remove aliasing and to preserve waves-in-ice information.

on rectangular windowed series, higher frequency noise is introduced from spectral leakage. Thus, the displacement data is lowpass filtered again to removed the undesired frequency components.

The displacement series is then multiplied by an energy conserving Hanning window function (energy correction factor = 1.63) to reduce the effect of spectral leakage caused by using a windowed signal when the spectral averaging method is performed.

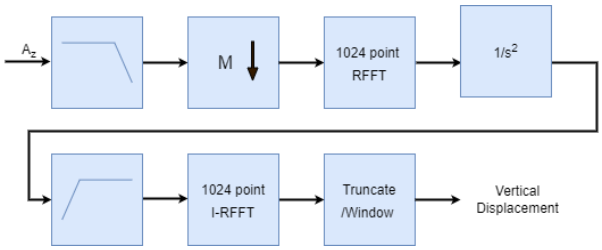

Figure 6.7: Pipeline to calculate displacement on the SHARC Buoy

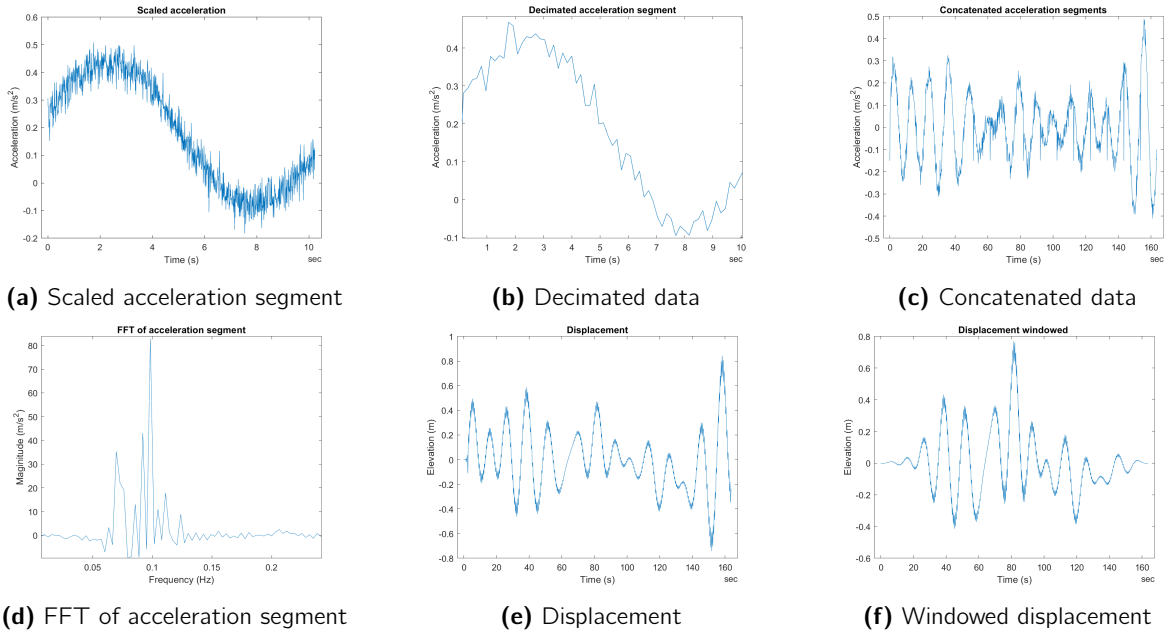

(a) Scaled acceleration segment **(b)** Decimated data **(c)** Concatenated data

(d) FFT of acceleration segment **(e)** Displacement **(f)** Windowed displacement

Figure 6.8: Plots of locally processed acceleration data on the buoy. Note that impacts between floes have been preserved in the dataset and can be observed, even after filtering and decimation in figure 6.8c.

A periodogram estimate must then be performed on the displacement arrays, using either Welch's or Bartlett's method to reduce the variance of the estimate.

Six 2:44 minute segments ($N = 6$) are averaged using Bartlett's method on the buoy with modified periodograms. To increase the number of periodograms and to reduce the loss of information resulting from the use of windowing, a 50% overlap should be used. However, as 6 time segments are used, with a total length of 16:20 minutes it is sufficient to use Bartlett's method (with modified periodograms). The windowing on the buoy performs two functions. Firstly, to reduce the spectral leakage by using a smooth window. Secondly, to reduce the effect of the transients introduced by integration which are present at the start and end of each segment which are less significant after windowing.

With the current implementation of Bartlett's method the variance of the calculated PSD is reduced by a factor of $N = 6$ when compared to the PSD estimation of a single segment using the periodogram estimate. Real FFT operations are used to reduce the calculation overhead of the FFT operations (as the acceleration signal is real valued). The PSD normalisation is complex (shown as $\frac{1}{K}$ in figure 6.9), with different FFT implementations using different normalisation values. The scale factor on the buoy is (see Solomon (1991, p. 9 - 10)):

$$1/K = 2 * \frac{1}{(\frac{1}{Fs/M})(1024)} \tag{6.2}$$

Where the spectrum is initially scaled by 2 to account for the energy of the full spectrum as the RFFT only accounts for half the spectrum (negative frequency spectrum is neglected). The spectrum is then scaled by the sampling duration to conserve energy (Parseval's theorem) and express the values in terms of m^2/Hz. This is calculated by multiplying the updated sampling period ($T = 0.16\ s$), given by the inverse of the initial sampling frequency ($Fs = 100\ Hz$) divided by the decimation factor ($M = 16$), by the length of the full FFT ($n = 1024$).

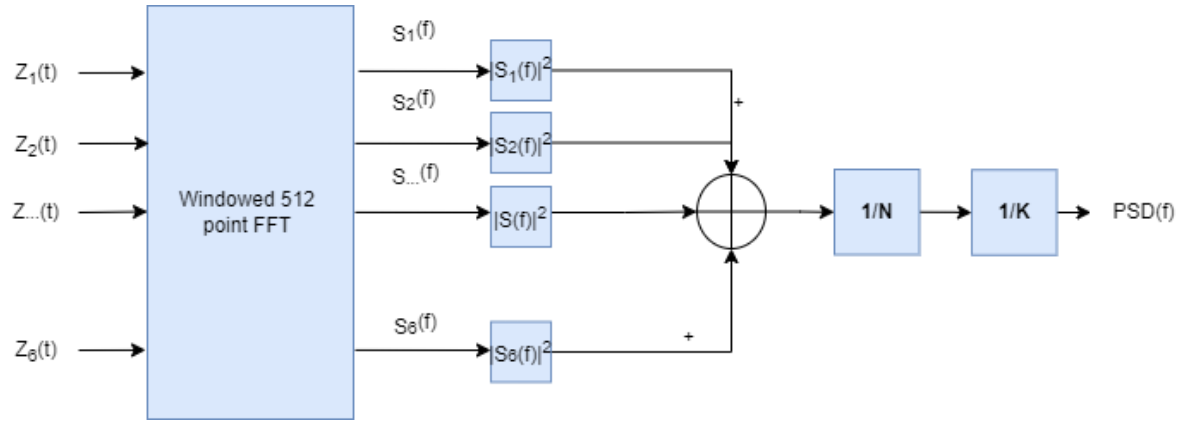

Figure 6.9: Pipeline to estimate the PSD from displacement segments. $Z_i(t)$ are displacement segments and $S_i(t)$ are periodogram estimates.

With additional development the Welch method could be used. This would require additional testing to ensure the accuracy of the estimates as well as the memory usage of the new pipeline implementation. The segments could be overlapped by 50% and increased in number to $N = 6 + 5 = 11$ segments. This would further reduce the variance of the PSD estimate by approximately a factor of: $\frac{9N}{11} = \frac{9(11)}{11} = 9$ (as opposed to the factor of $N = 6$ currently).

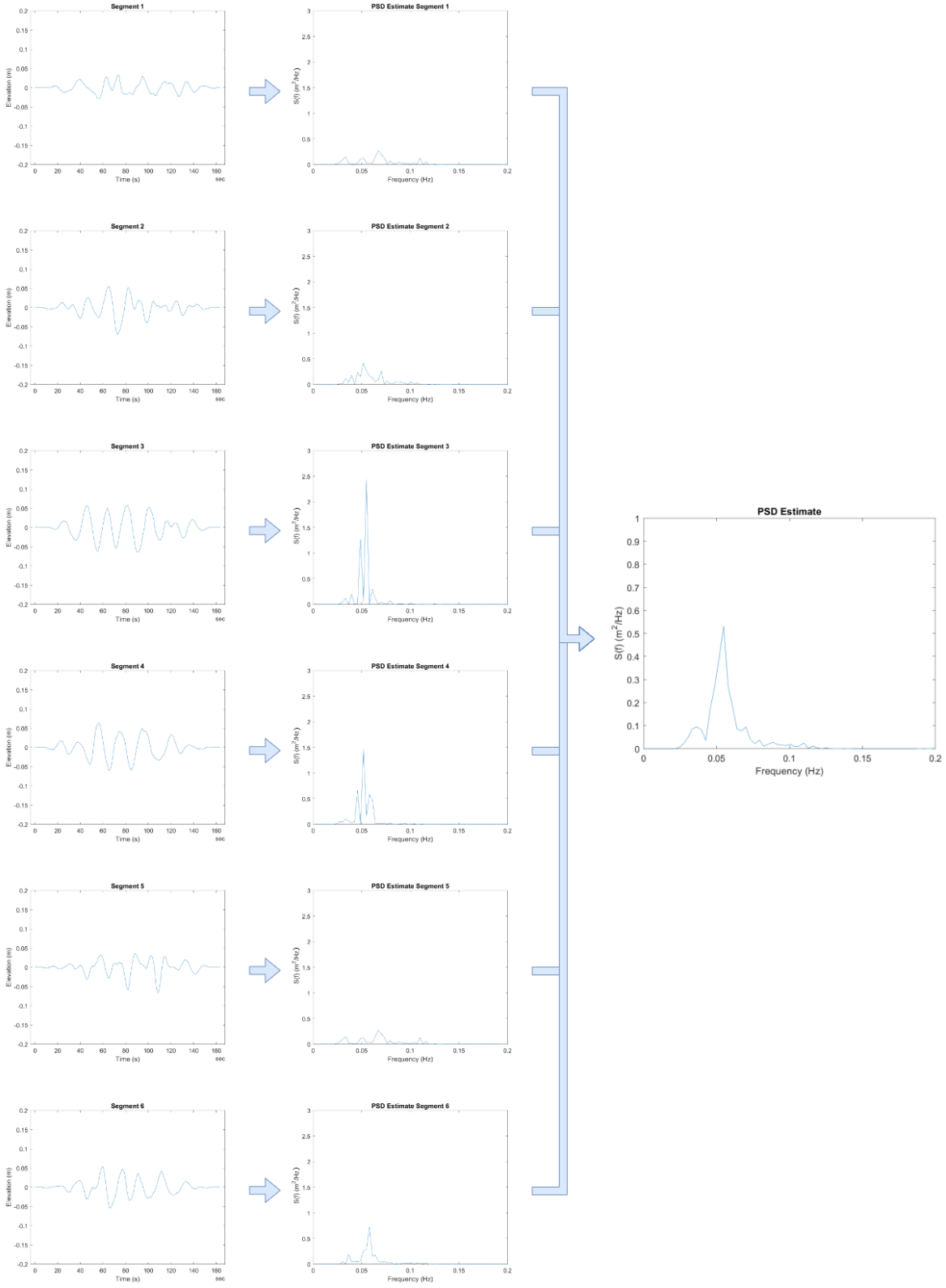

Figure 6.10: Locally calculated PSD estimates from individual windowed segments. Six segments are averaged to produce a final spectrum estimate.

Chapter 7

Testing

Before being deployed in an extreme environment the hardware and firmware of the SHARC Buoy underwent an extensive testing process. These tests were done in a controlled lab environment and immediately prior to deployment. Subsystem testing of each of the individual devices was done to confirm the reliability of the system.

7.1 Subsystem Testing

7.1.1 Inertial measurement unit

The ICM20649 was configured with an I2C interface. The device was configured to sample at 100 Hz with a full scale range of 4 g and then sampled for a period of 22 hours (approximately one day). No data corruption was found to have occurred in this period or in subsequent sampling periods. The testing was repeated in a freezer to validate reliability in cold temperatures

7.1.2 External memory

The external memory was first tested by opening, writing and reading to a file. This confirmed the functionality of the SDIO interface on the buoy. Following this several tests recorded large IMU datasets using the high frequency No data was found to have been corrupted and was stored in the correct folders and sub-folders on the FAT volume.

7.1.3 GNSS

The GNSS receiver and firmware was tested by confirming that the GNSS was to get a fix of the coordinates. This was done prior to deployment on the *SA Agulhas II*. The Ublox Neo 9M (ublox 2022) was able to give realistic location data that tracked the location data recorded of the Scientific Data System (SDS) onboard the ship.

7.1.4 Satellite communication

The Iridium 9603 modem uses AT commands. The Iridium modem was checked by confirming the response of the modem to specific commands. The modem recognised and interfaced reliably with the MCU using a UART interface.

7.1.5 Temperature testing

A primary concern for the buoy was its ability to function reliably and accurately in cold temperatures. Thus, the high frequency subsystem consisting of the ICM20649, the external memory and the STM32L4R5 were placed in a chest freezer set at $-20°C$ for a full day. The remainder of the buoy's interfaces had been tested at cold temperatures during previous deployments and so were considered validated already.

The IMU die temperature was logged. The IMU die quickly drops to the temperature of the freezer which was set at $-20°C$. No data was corrupted during the test, validating the performance of the subsystem at cold temperatures. The effect of temperature on the MEMS IMU can be determined using its error characteristics (see subsection 5.2).

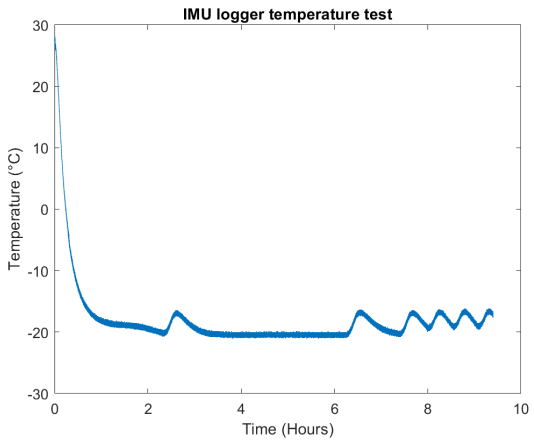

Figure 7.1: Temperature testing of the logger setup. The die temperature quickly reaches the air temperature inside of the freezer. Oscillations are caused by opening the freezer.

7.2 System Level Testing

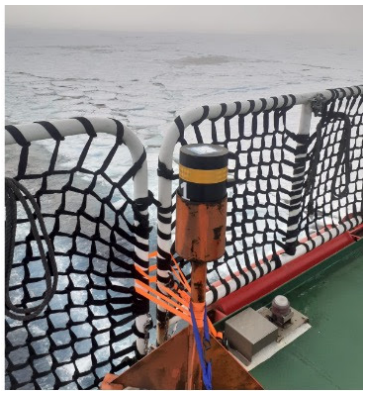

Figure 7.2: SB01 pre-deployment testing

7.2.1 Full System Operation and Remote Deployment

Prior to deployment on the SCALE winter cruise 2022 a SHARC Buoy was deployed on deck and tested for a duration of three days. The logged data was analysed to see if data corruption had occurred and if the environmental data tracked the measurements of the Scientific Data System (SDS) on the *SA Agulhas II*. This was done to validate the reliability and accuracy of the devices prior to deployment.

7.2.2 Accelerated power testing

To determine the operational lifespan of the system in its operational environment, the system was run in an accelerated test. This involved reducing the wave sampling period to 10 s which would result in the device processing a fixed set of wave data (dummy data collected from wave tank testing) and transmitting every few minutes. This allowed the testing of the new power supply's response to the large (2 A) current draw from the modem. The new supply did not suffer brownouts and functioned reliably for the duration of the test.

When running the buoy has a power consumption of approximately 120 mA. This corresponds to an operational duration of approximately 3 weeks (without a 50 % derating which appears to be overly conservative (Doble et al. 2017)). The primary concern for the power supplies is operation in cold temperature, in conjunction with the high instantaneous current draw from the Iridium modem. Thus, accelerated testing at low temperature was performed on the buoy. The wave sampling period of 30 minutes was reduced to 5 minutes. The SHARC Buoy was run for $\sim$700 sampling instances, this resulted in $\sim$ 700 Iridium transmissions. The locally stored data was analysed for data corruption. As the device performed reliably with no power management issues, this was considered to be a validation of the device's power supply and operation.

Chapter 8

Deployment and Retrieval

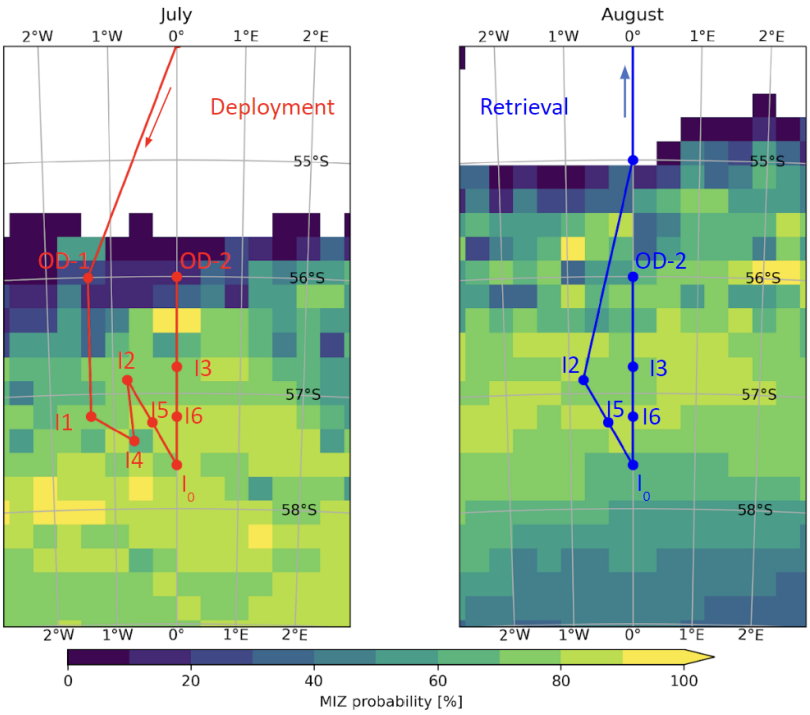

Figure 8.1: The planned deployment pattern for the SCALE WC22. Diagram credit: Marcello Vichi

8.1 Deployment plan

The Targeted Observational Experiment (TOE) aimed to collect data from an array of observational devices (measuring waves-in-ice, air temperature, drift etc.). The SHARC Buoys were deployed in conjunction with buoys from the Finnish Meteorological Institute. These included open ocean LainePoiss buoys (Alari et al. 2022) and an ice-tethered "box" buoy based on the work of Rabault et al. (2022). These systems would provide both additional information and act to validate the measurement of the SHARC Buoy V3.0.

The deployment (fig. 8.1) was designed such that it would coincide with a polar cyclone passing through the region. Additionally, it consisted of a fan shape, with the outer region being the ice stations (where systems were deployed), I1, I2, and I3. The inner region was of the fan were the

stations I4, I5 and I6 with I0 being the inner most point. This was designed to capture the wave activity both close to the open ocean and in consolidated ice.

The deployments were performed by hand from a personnel basket lowered onto the sea ice from the SA Agulhas II. The deployment procedure (see appendix E) of the SHARC buoys was planned to optimise the measurement of the buoy. The following considerations were taken in the selection of the deployment location:

1. Ice types
2. Stage of ice formation
3. Wave activity
4. Floe size

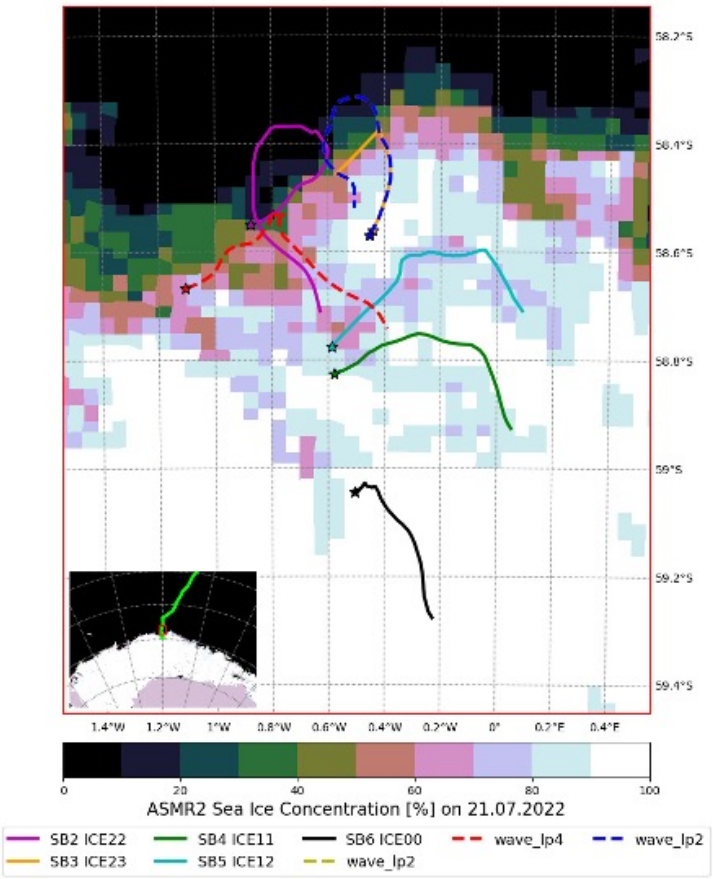

Figure 8.2: Buoy drift tracks for the duration of the experiment. Image credit R. Audh. SB01 path excluded.

The ice types and stage of formation (subsection 2.3.1) determined whether the device would have a possibility of lasting the full duration of the experiment. Ice that appeared to be in a consolidated state with the potential for lasting longer periods was selected. The stage of formation was guessed by determining whether the ice appeared to be in a state of growth and not melt. The wave activity was generally preferred to be smaller with the exception of SB02 which was deployed in high wave conditions next to the FMI box buoy and subsequently lost. Larger floe sizes were selected with the selected pancake being identified by the small ridges in the ice that define the individual pancakes before they were consolidated into the larger flow (see figure 8.4 D4.1, D4.2, figure 8.3 D6.2).

The device was deployed onto these pancakes as if the consolidated sheet then proceeded to undergo a mechanical break up, the device would still be located on a pancake. It was assumed that the failure of the ice would likely occur along ridges were the previous pancakes had fused. The final consideration was that the device should be placed as close to the centre of the pancake as possible to reduce the introduction of additional dynamics, resulting from the oscillation of the floe, into the IMU measurement.

8.2 Deployment description

Seven SHARC Buoy V3.0 systems were planned to be deployed. During the actual deployment six systems were deployed (SB01(Ice Station 21), SB02 (ICE22), SB03 (ICE23), SB04 (ICE11), SB05 (ICE12) and SB06 (ICE00)). Four systems were retrieved (SB01, SB04, SB05, SB06) with two losing GPS signal (SB02 and SB03). These systems likely were submerged in water and stopped transmitting as a result of water damage. This is a result of the sudden and unexpected collapse of the ice field resulting in devices sinking. Of the four retrieved, two had complete datasets (SB04 and SB06). The remaining two systems had data that was stored asynchronously as a result of a firmware bug which was corrected during the deployment period. The buoys were numbered SB01 - SB06 (**S**HARC **B**uoy 0X) with the associated deployment location (ICEXX) shown in figure 9.8. The actual deployment pattern is shown in figures 8.2 and 8.2.

The large variability in conditions during the deployment is shown for buoys SB04 (figure 8.4) and SB06 (figure 8.3). During the course of the experiment the consolidated ice on which the buoys were deployed collapsed. The larger floes fractured into their composite pancake floes due to mechanical breakup of the ice from waves and increases in atmospheric temperature resulting in change in the structure of the ice field.

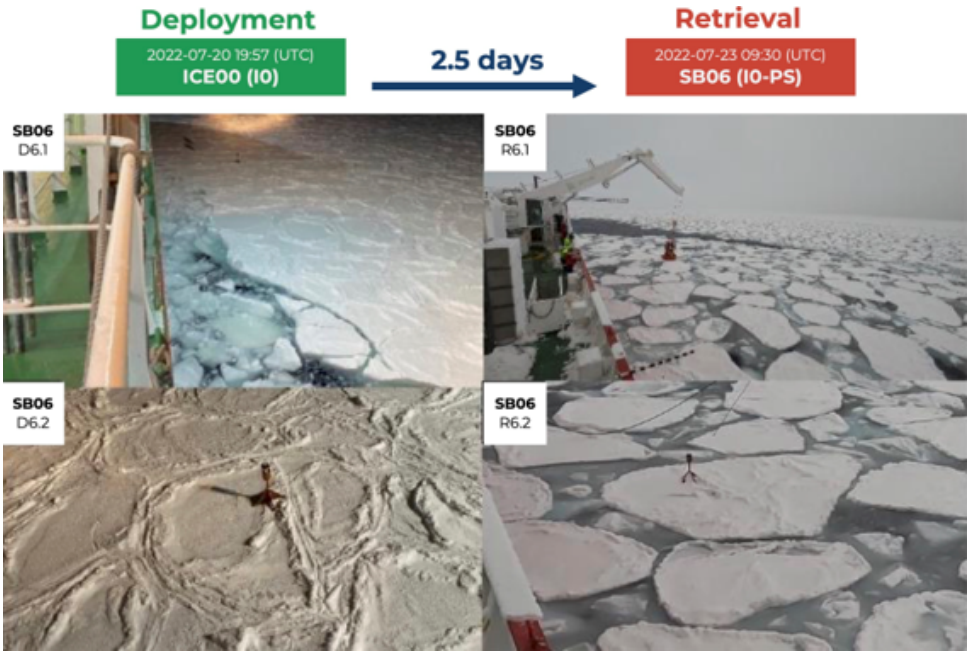

Figure 8.3: The conditions during the deployment and retrieval of SB06. Diagram credit: R. Verrinder, Photo credit: A. Spirakis

SB06 was deployed onto fully consolidated ice as shown in frame D4.1 (figure 8.3). The wave conditions were calm with movement being barely perceptible. Upon retrieval, SB06 was located on a large pancake, detached from the cemented floe, with noticeable wave activity. The consolidated sheet had been broken up into its constituting pancakes with brash and frazil ice in between. The

floes had points of contact as shown in frame R6.2.

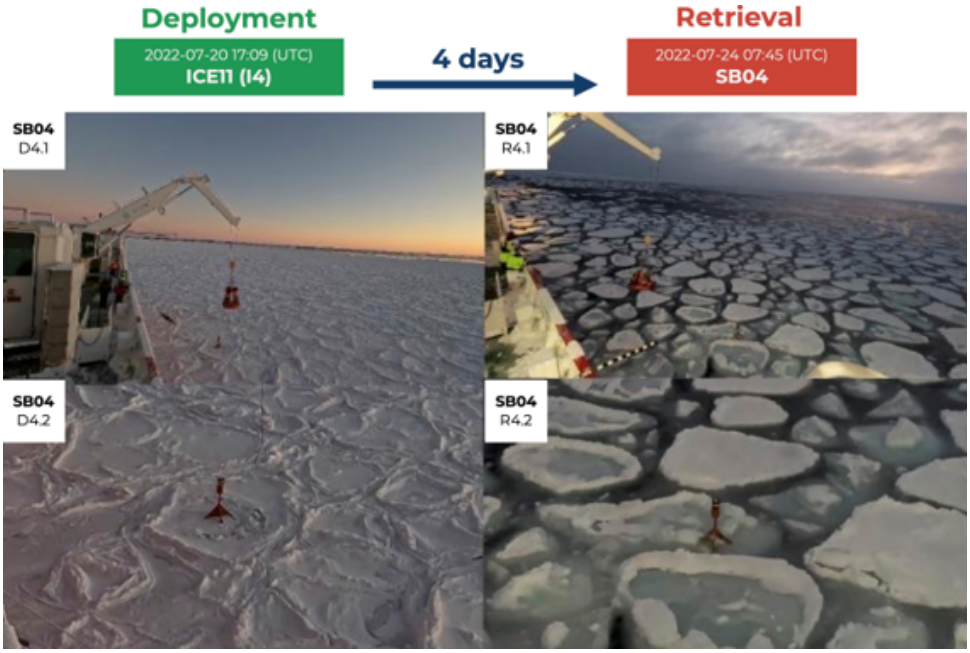

Figure 8.4: *SB*04

Figure 8.5: The conditions during the deployment and retrieval of SB04. Diagram credit: R. Verrinder, Photo credit: A. Spirakis

SB04 was deployed onto consolidated ice. The ice pancakes that made up the consolidated sheet in frame D4.2 were noticeably smaller than SB06. The ice sheet fractured into these smaller floes with the ice melt being more obvious (frame R4.2) than for the retrieval of SB06 (frame R6.2). The device had become closer to the edge of the pancake as a result of the melt. The size reduction resulted in an additional tilt and so this was investigated as a potential source of bias in the wave measurement in the results (chapter 9).

8.3 Retrieval description

To retrieve the devices it was first necessary to locate them. This was done by tracking the buoys using the regular location transmission from the devices. These transmissions occurred at approximately 40-minute intervals, allowing the devices to be tracked due to there regular transmissions (as opposed to a device which may have a longer sleep interval).

Retrieval consisted of removing the SHARC Buoy enclosure from the stand. There was initially concern that the high density polyurethane (HDPE) plastic enclosure would freeze into the inside of the stand's housing. Upon retrieval it was found that the mild steel cup did not freeze the plastic enclosure to the buoy stand allowing for easy retrieval using plastic handles which were attached to the enclosure. As the atmospheric conditions got warmer during the deployment it is possible that ice formation was not occurring during the retrieval period.

The retrieval process consisted of the *SA Agulhas II* maneuvering as close as possible to the buoy as possible. The personnel basket was lowered next to the device and collected by grabbing the buoy using the attached handle out of the stand housing.

The devices were then opened and the SD cards removed and the data backed up locally.

Chapter 9

Results and Discussion

9.1 Overview

The SHARC V3.0 was designed to collect waves-in-ice data. In this respect it has been successful, with four devices being retrieved with high frequency multi-day inertial measurements of the Antarctic MIZ which to the author's knowledge is the first occasion this has been done. Of these devices two had complete datasets with the remaining devices requiring additional post processing due to a firmware fault which fall beyond the scope of this thesis due to time constraints. These data can be used to develop more accurate models of the MIZ dynamics or be used as a reference for further research.

An analysis of the collected data shows that the device was able to capture the wave activity in the MIZ as the wave height and period showed similar results to the Finnish Meteorological Institute (FMI), which was used for validating the instruments.

As a polar cyclone occurred during the deployment (see figure 9.1) a clear distinction can be made for measurements that occurred before and after the storm passed through the area in which the devices were deployed. A comparison of the spectra shows the evolution of the cyclone during this period, showing the ability of the device to identify the different wave frequency components associated with the cyclone.

The collected IMU data has allowed the analysis of the data to determine the validity of the measurements of the devices in situ. This was done by analysing the time series data. Different methods of sensor fusion for the calculation of the vertical acceleration were investigated. It also allowed the investigation of the following sources of error:

1. The assumption that heave measurement is equivalent to the vertical acceleration
2. The dynamics introduced by using an elevated platform
3. Noise introduced to the measurement from the environment from other MIZ phenomena

In this data series, a series of spikes in the measured acceleration values were detected in both the vertical measurement (heave) and especially the sway and surge measurement.It is thought highly likely that these are the first inertial measurement of floe collisions by a device deployed onto the ice. This is due to the regularity of the impacts coinciding with the period of the measured waves. For ease of discussion and analysis the measured acceleration spikes will be referred to as collisions.

In addition to the wave data, location (and so ice drift) and environmental data (air temperature and atmospheric pressure) were collected. A comparison of these data to the onboard ship measurement was done for validation. It is found that the in situ air temperature measurements are valid. However, the atmospheric pressure measurement appears to require additional calibration.

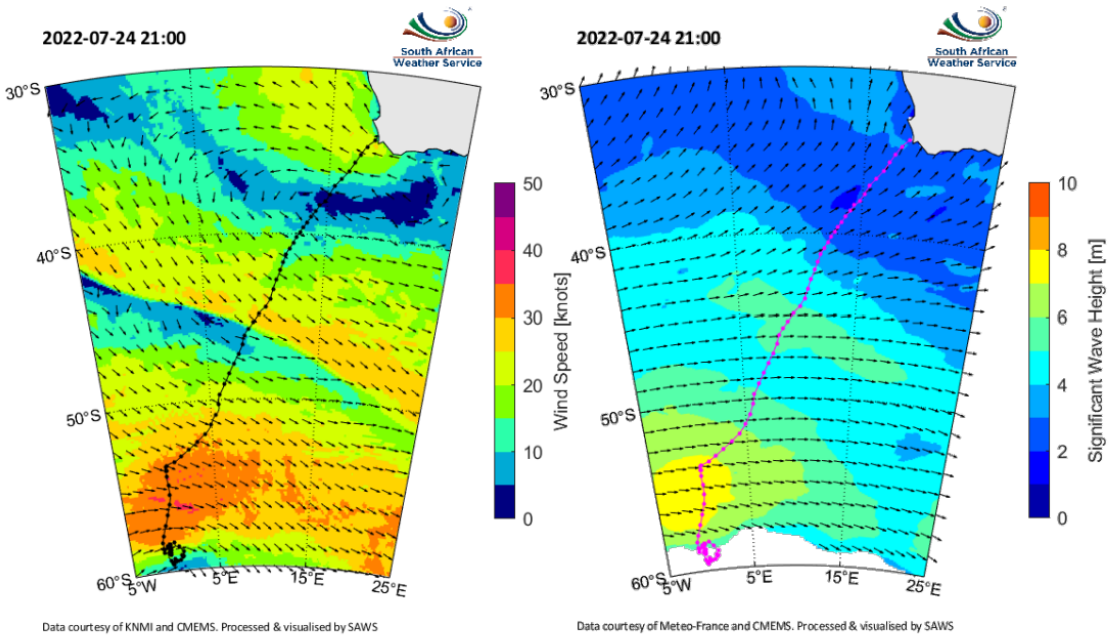

Figure 9.1: Mid-latitude cyclone which passed through the south-east Atlantic sector of the Antarctic MIZ during the cruise. Wind conditions (left) and wave conditions (right). Diagram credit: South African Weather Service (SAWS)

9.2 Wave Activity

9.2.1 Significant wave height

The significant wave height during the course of the deployment was a result of the swell waves generated by the polar cyclone in the area of deployment. There is a sharp increase in the wave height as a result of this well which is easily observed on the evening of the 22 July 2022. This was observed almost simultaneously (accounting for distance between the sensors). The development of significant wave height correlated to the measured wave height from the LainePoiss devices (Alari et al. 2022), known as LP Buoys. This correlation extended to the differences in measured wave height as the waves attenuated through the ice. For example when the polar storm waves propagated into the region, peaking locally on the evening of 22 July 2022, the LP Buoys measured a wave height in the range of $3-4$ m whilst the SHARC Buoys, which were deployed further into the ice cover measured a significant wave height of $2-3$ m. Following this the wave height increased steadily, which was captured by the SHARC Buoys, particularly SB04 which was deployed for a longer duration. Furthermore, LP4 and SB04 measured a wave height of approximately 4 m on the morning of the 24 July 2022 when SB04 was collected. The similar measurements are likely due to the fact that LP4 was drifting close to SB04 (see figure 8.2) with LP4 drifting onto the previous path of SB04.

The correlation between the measurements, accounting for the distance between the sensors and

attenuation of wave height under ice cover, strongly indicates that the SHARC V3.0 is capable of accurate wave height measurement.

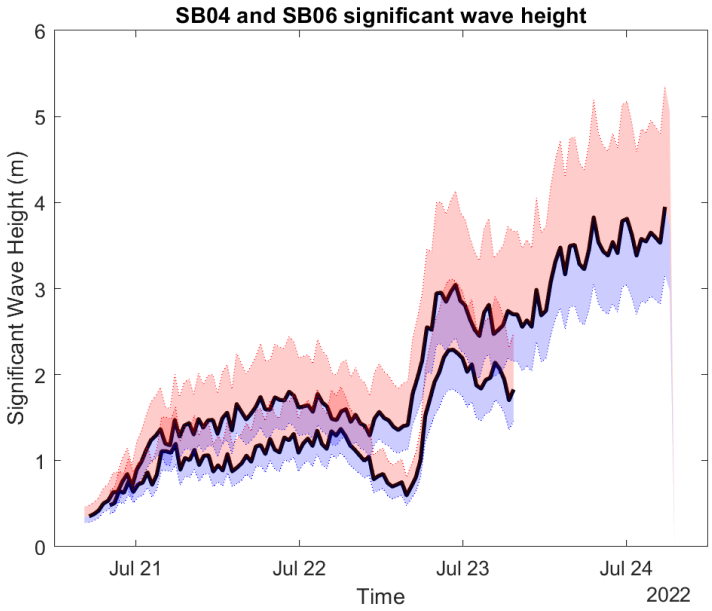

(a) Significant wave height (H_{m0}) of SB04 (top) and SB06 (bottom) including with a 90% certainty interval.

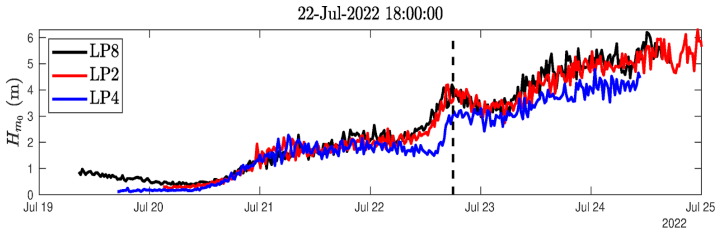

(b) FMI open water LainePoiss (LP) buoys. Diagram credit: Jan-Victor Björkqvist, FMI

Figure 9.2: Significant wave height during the course of the deployment

9.2.2 Mean wave period

The calculated mean wave period went from an initial 18 s to $15 - 17$ s on the start of the 21 July 2022, which corresponds closely to the value of the LainePoss buoys in the region (approximately 15 s). The mean wave period then drops to $10 - 11$ s for the SHARC Buoys and to $8 - 10$ s for the LainePoiss Buoys after the wave field from the polar storm reached the region. The longer wave period from the buoys in this case probably resulting from the attenuation of high frequency wave components (resulting in a longer mean wave period calculated from the wave spectra) from the storm in the ice as the LainePoss Buoys were deployed closer to the open ocean.

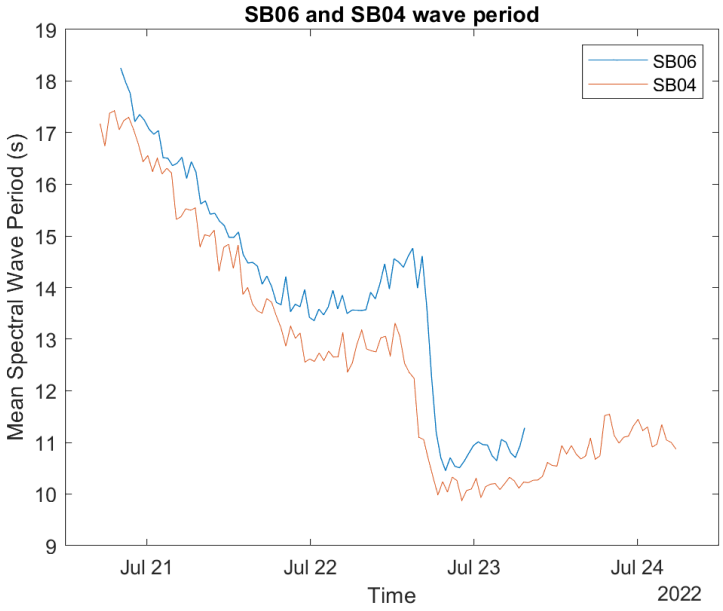

(a) The mean wave period (T_{m0}) of SB04 and SB06.

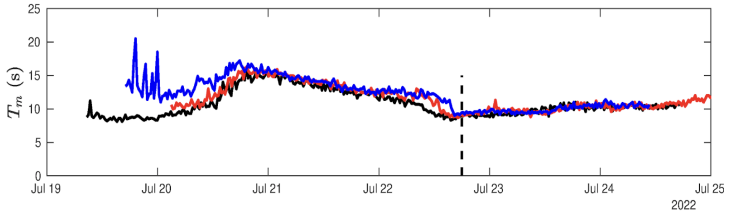

(b) FMI open water LainePoiss (LP) buoys mean wave period. Diagram credit: Jan-Victor Björkqvist, FMI

Figure 9.3: Mean wave period during the course of the deployment

9.2.3 Drift vs. Significant wave height

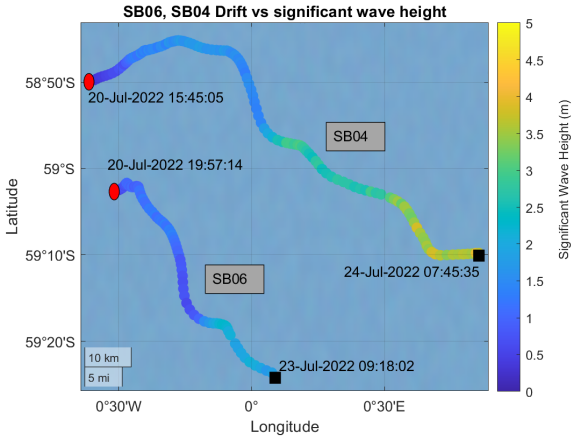

Figure 9.4: Mean wave height

Figure 9.5: Significant wave height and mean wave period during the deployment of the buoys compared to the drift.

The drift westwards corresponds to the increase in significant wave height. This corresponds to the arrival of a polar storm during this period, resulting in both increased drift and a larger wave height. This corresponds to the observations and measurements from the FMI instruments.

9.2.4 Wave spectra

During the deployment, a storm developed. To determine if the devices were able to measure the changes in conditions, a spectral analysis of the 30 minute data samples collected during the deployment was performed. This was done using the pipeline described in section 3.2. The shift from the low frequency smaller wave swell present in the region to the higher frequency wave generated by the recent storm is evident.

To emphasise the shift and show that the devices were capable of measuring accurate spectra, three spectra were calculated for SB04 and SB06. One spectrum for the period before the storm (20 - 21 July 2022), one during the storm (22 July 2022) and finally a spectrum after the storm waves had moved into the region (23 July 2022). The shift from a peak wave frequency at $\sim 0.06\ Hz$ to a peak wave frequency of $\sim 0.10\ Hz$ is clear.

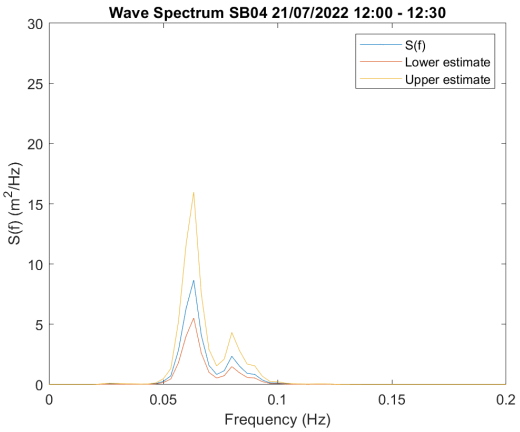

(a) SB04 before storm

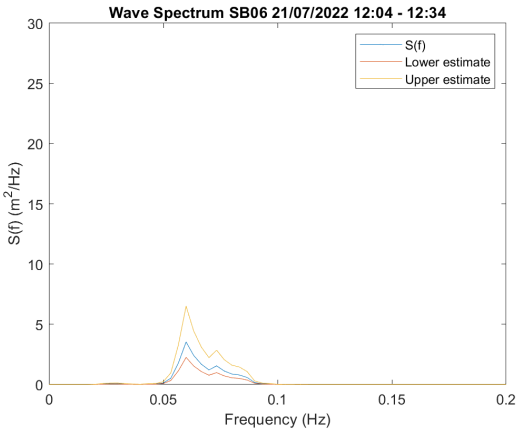

(b) SB06 before storm

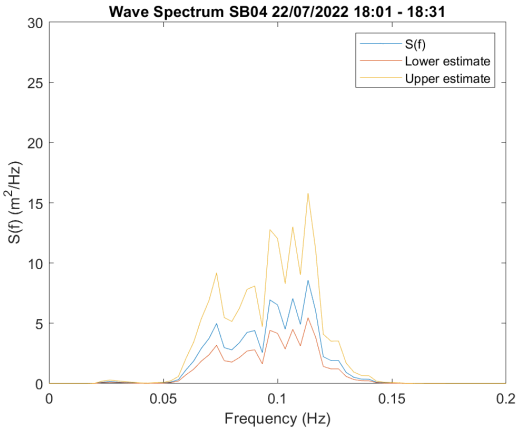

(c) SB04 during storm

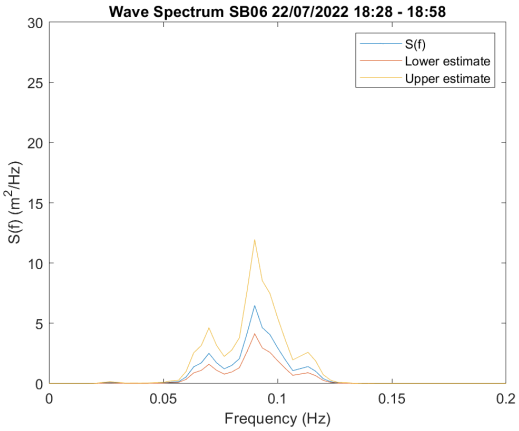

(d) SB06 during storm

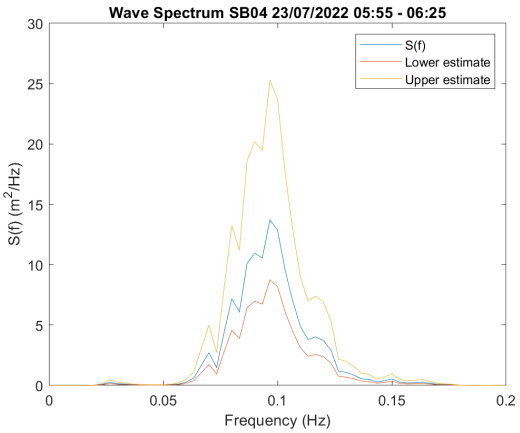

(e) SB04 after storm

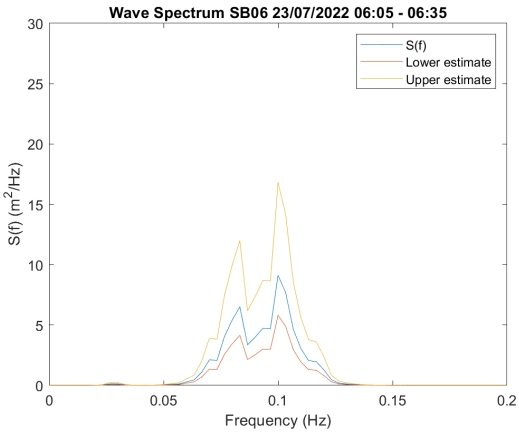

(f) SB06 after storm

Figure 9.6: Wave spectra to show the development of the storm as measured by the SHARC Buoy devices SB04 and SB06.

The wave spectra measured by the SHARC Buoy underwent a predictable development from the initial swell waves present to about 0.06 - 0.08 Hz to being dominated by the storm swell centered at 0.10 Hz.

9.2.5 Stand correction

The correction for the stand dynamics and vertical acceleration is compared to the estimation of wave height from the heave measurement only, which is used for the local calculation of wave parameters. The maximum error was approximately 0.3 m with the average error being less than 0.1 m. It is noted that the error incurred by using the heave measurement increases in high waves as the small angle assumption (i.e. the platforms tilt is ≤ 10 °) does not hold for all measurements (see section 3.4). The small angle assumption holds in condition with long wave periods and low significant wave height (resulting in low wave steepness). However, for wave height estimation in high waves with smaller wave period, the error became significant. Therefore, future development of the buoy should start with the integration of sensor fusion of multiple axes to reduce the underestimation of significant wave height for steeper waves. However, this sensor fusion should be designed so that floe collisions do not bias the vertical acceleration measurement (i.e. appropriate filtering is performed).

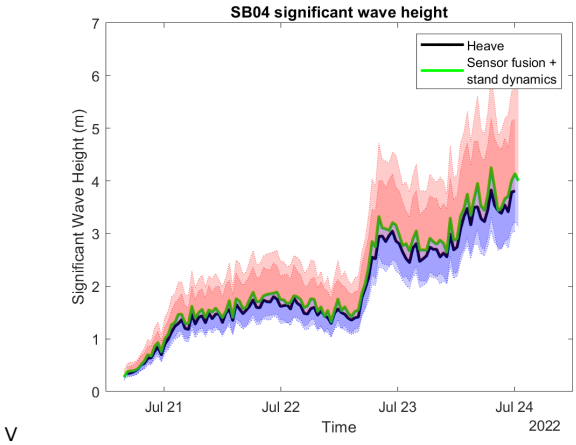

V

Figure 9.7: The difference in significant wave height calculated from heave only compared to the fusion of all axes using a Kalman filter and the introduction of the wave dynamics.

9.3 Drift Data

The platforms underwent significant drift, with the westward drift of some the devices being over 200 km for the maximum deployment period. The GPS data was accurate enough to enable the retrieval the devices. Further characterisation of the GPS error is a priority but has not been done for the SHARC Buoy beyond the collection of the standard dilution of precision (DOP) measurements. The GPS data allowed the identification of the Coriolis effect causing the spiral of SB02. SB01 may have undergone an *inertial oscillation* early in its drift which is of interest. However, this needs to be confirmed by further analysis. The drift was sufficiently rapid at points to cause a Doppler shift (see section 3.5). However, this shift was sufficiently small to be neglected in most cases (maximum measured shift 0.005 Hz, see figure 3.11).

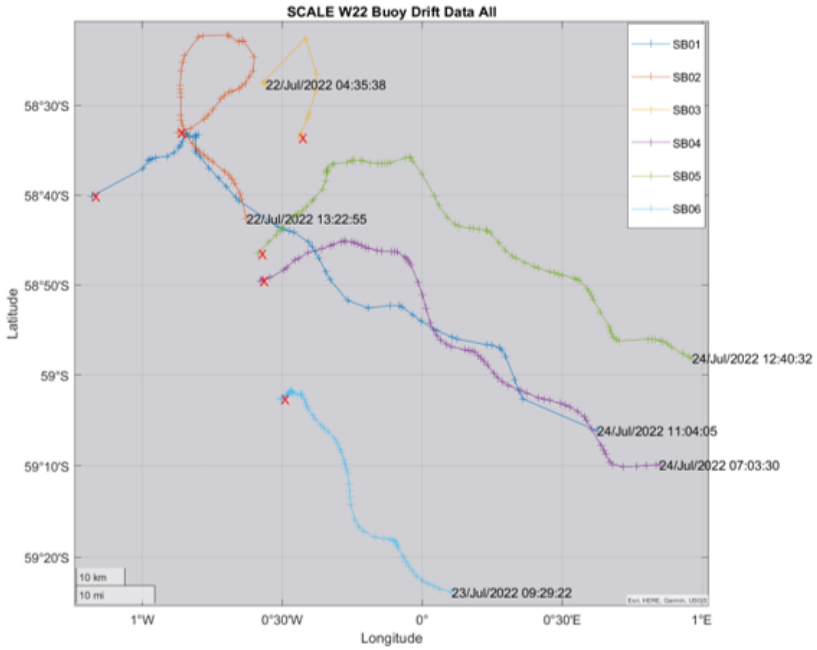

Figure 9.8: The drift pattern of the buoys during the SCALE 2022 mission

9.4 Environmental Data

The air temperature data collected corresponds to the data collected by the the *SA Agulhas II* by its scientific data system (SDS). The temperature induced melt from the ice was observed in thermal camera measurements from the *SA Agulhas II*'s deck and corresponds to the melt observed during the retrieval of the instruments (see figures 8.4, 8.3). The air temperature can be seen to be around 0 $^{\circ}C$ which is the air temperature range at which melt would occur. It should be noted that ice melt is more closely related to seawater temperature than air temperature.

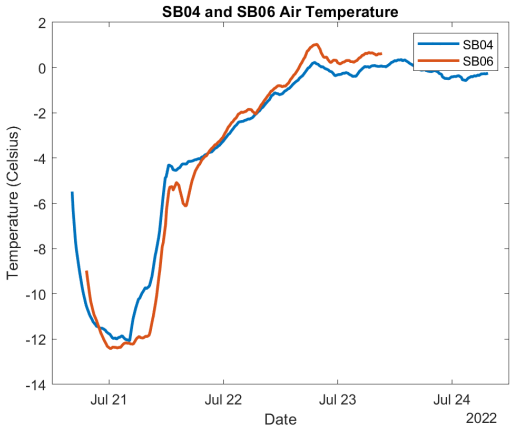

(a) Temperature graph of SB04 and SB06

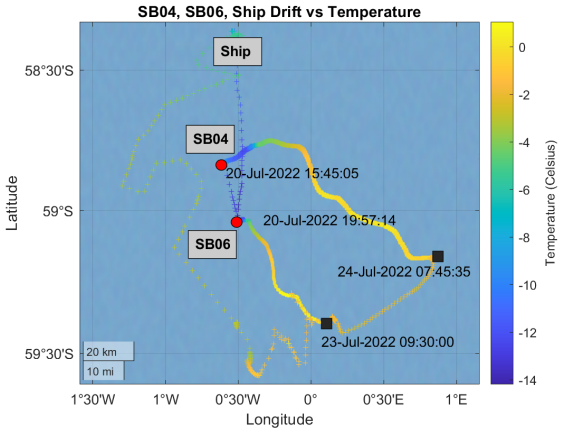

(b) Geoplot of the temperature of SB04 and SB06

Figure 9.9: Temperature data plotted of SB04 and SB06

9.5 Waves-in-ice phenomena

9.5.1 Floe-floe impacts

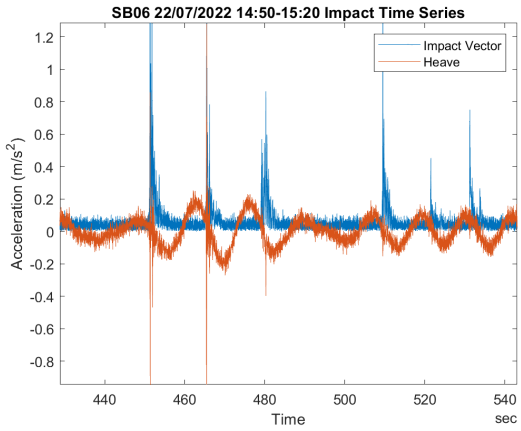

(a) Impacts in time series.

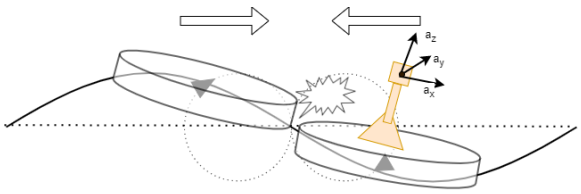

(b) IMU axes during impact

Figure 9.10: Acceleration spikes in time series hypothesised to be floe-floe impacts

The collisions between neighbouring ice floes were potentially observed in the collected data. This is the first time raw inertial data has been collected off an ice tethered instrument and so analysis is done to justify the hypothesis that the acceleration spikes observed are indeed ice floe collisions. Within the dataset, spikes in the acceleration were observed such as in figure 9.10a. These impacts are caused by wave orbitals (see section 2.3.3).

The analysis of collisions was performed by creating an impact vector of the acceleration parallel to the wave surface (a_z, a_y in figure 9.10b). This was then compared to acceleration in the heave axis (a_z). Visually, the regularity of the spikes can be seen to correspond to the wave period (figure 9.10a). In the wave tank experiments of Yiew et al. (2017) and Bennetts & Williams (2015), for large wavelengths relative to the floe diameter, collisions are observed approximately once per wave period. Thus, the frequency of the collisions is compared to the mean wave period (Tm_{01}) over the course of the deployment, and correlation between the wave period to the frequency of the collisions is used to strongly imply that the collected data includes high frequency information describing the collisions. As can be seen in figure 9.6, the dominant frequency before the storm consists of waves in the $0.06-0.08$ Hz frequency range. This then shifted to a dominant frequency of ~ 0.1 Hz due to the arrival of a wave field from the storm that occurred during the deployment. The previous swell waves are still present. Thus, it is expected that the collisions will occur at approximately $0.06-0.08$ Hz initially and then shift towards 0.10 Hz.

The frequency of collisions is then expressed as a ratio of collisions per mean wave period. The collisions occurred at a very low frequency initially, corresponding to wave tank testing results predicting impacts approximately once per period at low frequencies (≤ 0.5 Hz).

The number of impacts per period then increased exponentially as the higher frequency waves generated from the swell arrived. Following this, the number of collisions peaked and then dropped down to lower levels. It is hypothesised that the presence of multiple wave fields resulted in out of phase movement between the ice pancakes resulting in the large number of collisions. This could potentially mean that pancake collisions in certain conditions (i.e. the interaction between wave fields) are far more important than previously thought in the attenuation of wave height and the behaviour of the Antarctic MIZ. The measurements for SB04 continued further and displayed a

second increase in collisions on 23 July 2022.

A second potential effect could be that as more consolidated ice is closer together (i.e. location of SB06 deployment), more collisions occur relative to ice further apart (SB04 was deployed closer to the open ocean).

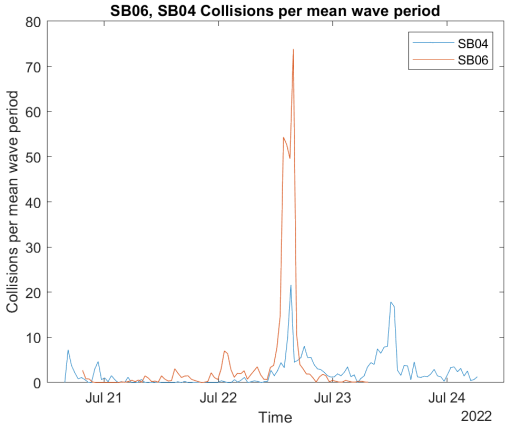

(a) The collisions between floes per mean wave period.

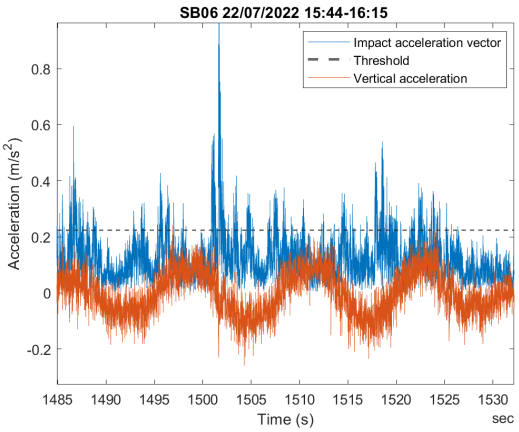

(b) High impact wave sample. Large number of acceleration spikes shown.

Figure 9.11: The number of collisions per mean wave period (left). The sample showing high number of collisions per period for SB06 (right).

9.5.2 Attenuation

The attenuation between the two devices included in the analysis (SB04 and SB06) can be determined using the approach of (Meylan et al. 2014) (see section 2.3.2). This approach assumes that the distance between the sensors calculated in terms of the distance between the sensors measured in terms of their distance into the ice. The ice is assumed to be homogeneous to simplify the analysis. This is not the case as can be observed in figure 8.2 with the tracks of SB04 and SB06 having some in-homogeneity with in-homogeneity across time also being a factor. However, the determination of attenuation of significant wave height as the waves propagate into the ice allows for the validation of the device as a waves-in-ice instrument, as this is a primary concern in the field. A simple observation of figure 9.2a showing the significant wave height shows clearly that SB04 (top line) has a greater significant wave height than SB06 (bottom line). This shows the attenuation of wave height between the devices. Additionally, it is clear that the attenuation increased as the distance between the devices became greater (see figure 8.2, 9.8 and 9.4).

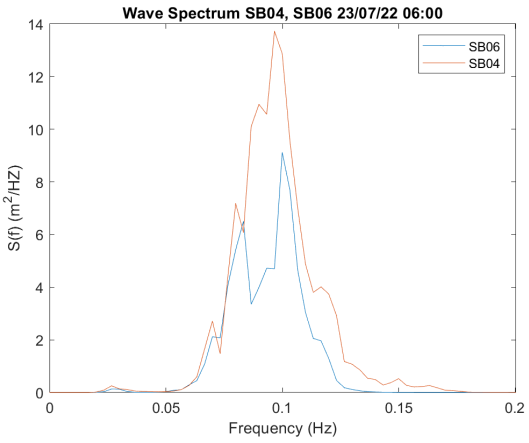

Figure 9.12: Attenuation between SB04 and SB06 after storm on 23/07/2023 at approximately 06:00

9.6 Evaluation of in situ wave parameter extraction

During the deployment, the wave parameter extraction pipeline did not function as intended. This was due to an array being overwritten in the pipeline. This produced unreliable results (which were transmitted via Iridium). This has been corrected in the firmware. A comparison of the spectrum and wave parameters calculated locally on the device to the spectrum and parameters calculated using the pipeline developed on MATLAB, using a retrieved dataset, is done (see description in section 3.2). The MATLAB signal processing pipeline functions as a golden standard for comparison. In particular, MATLAB's *pwelch* spectral estimate is compared to the estimator implemented on the SHARC V3.0. This is done for a 30 minute sample collected by SB04 on 20 July 2022.

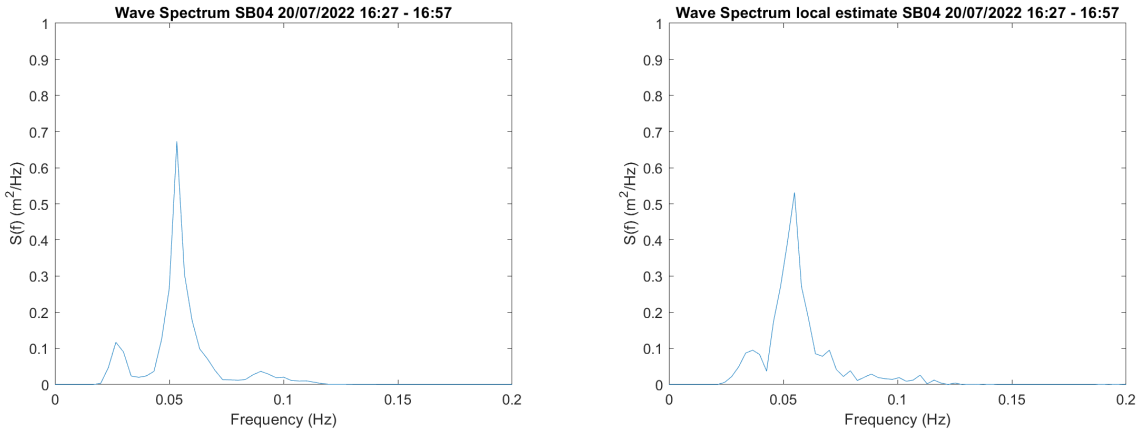

(a) Gold standard **(b)** Local

Figure 9.13: Comparison between local and gold standard wave spectrums.

It should be noted that the primary difference between the *gold standard* spectrum and the *locally* estimated spectrum is the broader spectrum around the spectral peak in the locally calculated spectrum. This is caused by the energy conservative (as opposed to amplitude conservative) windowing performed on the elevation time segments. A comparison of the calculated wave parameters shows the accuracy of the locally estimated spectrum:

Table 9.1: Wave parameters from golden measure vs. local pipeline

Parameter	Golden Measure	Local
Hm0 (m)	0.35	0.37
Tm01 (s)	18.18	17.67

The parameters calculated in table 9.1 show close correlation in wave height. There exists an estimation error of approximately ~ 0.5 *s* in the estimation of mean wave period, this is likely due to increased variation in the measurement of the *local* pipeline in comparison to the *golden measure* pipeline.

A final opportunistic note of the graphs shown (fig 9.13) is that there exists a second smaller spectral peak at $0.03 - 0.04$ *Hz*. It is possible that this is a result of the platform (i.e. ice pancake) that the device is deployed on. The phenomenon of spectral spreading due to platforms with strap down IMUs interacting with waves (subsection 2.5.2, 3.1.2, Lang (1987)) is well known. This has not been quantified in ice-tethered instruments (as the estimation of ice floe size and shape is difficult) and should be investigated further once pancake size data from the SCALE 2022 becomes available to complement the inertial time series data.

9.7 Comparison with contemporary waves-in-ice instruments

Several contemporary waves-in-ice devices exist. Highlighting the differences between the SHARC Buoy V3.0 and these instruments is done to emphasise the strengths of the device as well as highlight its limitations.

The device is able to collect and remotely transmit data that is equivalent in accuracy to the OpenMET Buoy (Rabault et al. 2022) the LainePoiss Buoy (Alari et al. 2022). Several key advantages are present for the SHARC Buoy. Firstly, the device stores data locally which allows for raw data to be collected. As there are several under-investigated inertial phenomena (ice floe impacts, rafting, hydrodynamic properties of the floes) that are neglected by spectral averaging this is very useful. Similar devices store wave data in RAM which is overwritten for the next sampling period as opposed to storing the data in external memory.

Secondly, the stand and enclosure in conjunction with the large power supplies used by the devices allows for increased survivability for longer deployments, setting it apart from the OpenMET Buoy (known as the "Box Buoy" during SCALE Winter Cruise 2022). The device is capable of measuring and transmitting wave measurements with the key feature of the system being that it is cost effective (∼R20 000) which is significantly better than older devices such as the Waves-in-ice Observation System (WIIOS) and comparable to the OpenMET Buoy. Thus, the SHARC Buoy fulfills a niche for an instrument intended to survive harsh Antarctic storm conditions whilst still being cost effective. Similar devices may be better deployed on more consolidated ice as they lack a protective stand and are vulnerable to wave overwash and ice production.

Chapter 10

Conclusion

10.1 Waves-in-ice Measurement

The UCT SHARC Buoy V3.0 was capable of measuring waves-in-ice phenomena. The main contribution of the device was the collection of high frequency raw inertial data off pancake ice floes. In addition to this, the collected data was used to validate the in situ measurement of the buoy. The collected data from SB04 and SB06 were the most complete, with SB01 and SB05 requiring post-processing as a result of a firmware fault (which caused the sampled data to be stored out of order).

This data correlated strongly to the measured data collected by the Finnish Meteorological Institute (FMI) devices for significant wave height and mean wave period. The collected data also showed clear attenuation between SB04 and SB06. The small angle assumption used for in-situ processing was tested using the data. It is shown that the assumption generally holds true for lower wave amplitudes but underestimates the waves at higher amplitudes.

The distance between the deployed SHARC Buoys and FMI instruments was too far to fully validate the measurements. As a result, it is recommended to perform tests in the open ocean next to a buoy platform for full validation of the measurements.

The collection of raw high frequency data also allowed the novel analysis phenomena such as the impacts between floes. These were shown to be far more prevalent than expected are present an interesting direction for analysis. These spikes also appear to occur often enough that the standard statistical checks to remove outliers may fail in this case.

10.2 System Validation

The SHARC V3.0 was deployed in the SCALE Winter Cruise 2022. Two devices were retrieved with full inertial datasets. Two devices malfunctioned causing the data to be stored out of order. Two further devices were deployed as ice-drifters whose primary purpose was to collect location data.

The upgraded SHARC V3.0 was able to function in extreme conditions. The updated power supply allowed continuous operation during the deployment and the collected data reflected the wave conditions of the region. The GPS and environmental data also correlated strongly to other sensors aboard the *SA Agulhas II*'s SDS.

Using the data from the SCALE 2022 deployment, along with the known performance of the

device, post-deployment firmware development (updating the local wave algorithm to produce more reliable results for transmission and improving reliability) was completed to reach the desired technology readiness level (TRL). This allowed SHARC V3.0 reached the technology readiness level (TRL) of 9 ("Actual system "Antarctic MIZ operation proven" through successful mission operations") for ice drift, environmental measurement and inertial measurement (stored locally) and a TRL of 8 ("Antarctic qualified" through test and demonstration") for in situ transmitted wave measurement .

Chapter 11

Recommendations

11.1 Sensor fusion

It is recommended to investigate the fusion of GNSS and IMU measurement to estimate heading the system to allow directional wave measurement. A higher frequency GNSS-IMU fusion will allow in situ directional wave measurements of the region to be taken. This is very important to the investigation of waves-in-ice (Alberello et al. 2022). A significant problem being the lack of reliability of magnetometers near the polar regions (Kohout et al. 2015). This means that either a calibration process for the magnetometers in the field with validation (such as the determination of heading from the solar azimuth using onboard cameras (Doble et al. 2017)).

Another approach would be the use of GNSS to determine heading (Herbers et al. 2012). Specifically, the velocity components on the GNSS measurements could be used to derive directional wave measurements. However, it would need to validated in the Antarctic region as the choice of GNSS satellites constellations, GNSS receiver and operating frequency could affect the measurements.

Considering the considerable drift experienced by the buoys, including changes in direction, heading estimation may be possible using the acceleration or velocity of the system in conjunction with high frequency GPS measurement to determine heading (Gade 2016).

These techniques have been investigated to determine the heading of AUVs (autonomous underwater vehicles) for navigation under ice-sheets (Lone 2020). Thus the application to Lagrangian (drifting) instruments is possible. Accurate in situ directional wave measurements would be a valuable addition to the SHARC Buoy system.

11.2 Real time operating system (RTOS)

The growing size of the SHARC Buoy codebase and the potential to increase the number of sensing systems and functionality of the devices strongly suggest that moving the firmware to a Real Time Operating System (RTOS) is desirable. Instability in the system is a concern with the growing size of the codebase (Lethaby 2013).

In particular, the need to record high frequency measurements in parallel to processing information and responding to interrupts. This multitasking paradigm is available using an RTOS middleware such as FreeRTOS.

Additional benefits of switching to an RTOS are introducing proper timing to tasks, improving portability between MCUs and a more efficient use of CPU resources (Lethaby 2013).

11.3 LoRa and data collection

High frequency data of the region is valuable as it allows the investigation of the dynamics of ice floes which are of interest.

This could be done with LoRa (long range) based communication systems. The integration of LoRa is a potential means by which instruments could communicate both with each other and with a retrieval device onboard a ship. The potential for easier data retrieval is important

LoRa performance in the field would need to be assessed. Additionally a protocol for buoy-buoy (allowing data transfer between buoys means that fewer buoys would have to be communicated with - reducing travel distance on a mission) and buoy ship communication would have to be developed.

11.4 IMU selection

The Invensense ICM20649 was appropriate for the 2022 SCALE cruise. However, it has since been deprecated. Additionally, development time was increased by the need to develop a driver for the device.

To reduce development time during future development it is recommended to use a low power high accuracy and stability (for reliability) IMU with existing drivers and filtering software that can be validated for wave applications such as the STM32 X-Cube-MEMS1-FX middleware with a supported device such as the LSM6DSL 6DOF IMU (ST Microelectronics, 2017). This would accelerate the speed of development for the given hardware on the buoy (STM32L4R5 MCU) for the implementation of onboard sensor fusion or the update of the communication interface to a DMA sampling approach with a FIFO buffer. The LSM6DSL has a smaller temperature variation, including additional temperature compensation.

If high accurate centimetre or even millimetre level measurements are desired (deployment on multi-year consolidated flows) a higher precision commercial IMU should be used from a manufacturer such as XSens or VectorNav.

11.5 Algorithm optimisation

The current wave parameter extraction pipeline takes approximately ∼18 minutes to run. This is due to the reading in of 180 000 values from an external SD card and processing the data in individual segments. The following approaches or updates will decrease the time taken to process the onboard data.

1. If a more accurate IMU is used with a Kalman filter, the use of the double integration with a high pass filter is unnecessary. The calculation of the spectra can be performed by integrating the acceleration spectra by multiplication by $2\pi f^{-4}$.

2. If the raw data from the devices is not retrieved, the decimated acceleration data can be stored incrementally in RAM or flash memory. When the pipeline is run, the data is already in RAM, allowing, removing the slow read in process.

3. Rewrite the SD drivers to use binary as opposed to ASCII data storage.

11.6 Onboard Kalman filtering

The buoy should run an onboard Kalman filter in order to perform a fusion of the sensor measurements. However, it is suggested that the retrieved raw time series be used as a reference dataset to evaluate the performance of the sensor fusion done onboard the buoy.

A tuning of the Kalman filter should be done in order to retrieve reasonable results that are not biased by the process noise created by measuring waves through an ice tethered instrument.

The measurement noise covariance matrix can be estimated by the error characteristics of the IMU. However, given the process noise introduced, such as the impacts between floes, the process noise covariance matrix would need to be tuned. This would reduce the contamination of wave measurement by other processes in the MIZ.

11.7 Pancake dynamics analysis

A concern is the presence of low frequency drift introduced by the ice platform into the IMU measurement.

The size and shape of the pancakes affect their response to waves. The general assumption made is that if the wavelength is sufficiently large that the pancake will move with the waves as it will have sufficient time to respond (Yiew et al. 2016) without adding an additional transient response.

However, given the experiences of the SCALE 2022 cruise, there was interaction between the pancakes floes in previously consolidated ice and the open ocean as a result of the collapse of an ice field. This resulted in floes potentially encountering high frequency wave excitation. Thus, the response of these pancakes in these unusual conditions is of interest, in particular how these conditions affect the measurement of waves.

The presence of low frequency components as a result of spectral spreading (Lang 1987) should also be analysed to see if information about the size and shape of the pancake can be extracted.

11.8 GNSS wave measurement

GNSS based wave measurement is rapidly becoming the standard wave measurement approach (Herbers et al. 2012, Raghukumar et al. 2019). Integrating this approach into future SHARC Buoys should be considered. In particular, this approach should be validated using inertial wave measurement, due to concerns about GNSS accuracy in the Southern Ocean.

11.9 Full validation of wave measurement

The SHARC Buoy deployed next to the OpenMET ("box") buoy was unfortunately lost. Additionally, the remaining instruments were too far to directly validate the measurements. It is highly recommended to perform open ocean tests with the platform for full validation next to a validated buoy platform.

Appendix A

Wave Tank Testing Setup

This is the initial experimental proposal, including experimental planning, for the wave tank testing for the IMUs used on the UCT SHARC Buoy.

A.0.1 Experimental Setup

The experimental setup consists of a pseudo-ice float with a IMU-microcontroller-RF transmitter setup deployed on top that communicates acceleration data to a host computer.

The pancake and electronics configuration will hereafter be refered to as the SHARC-i buoy (Southern Hemisphere Antarctic Research Collaborative Buoy - Ice).

Two IMUs will be deployed on the SHARC-i, a high cost factory calibrated IMU (VectorNav VN100) and a low cost IMU that has been calibrated using the method of Tedaldi et al. (2014). This will allow the comparison of data between the IMUs as well as to the wave data collected within the wave tank.

The SHARC-i will be deployed in a wave tank in the CSIR Coastal and Hydraulics Laboratory. The facility has the capacity to generate waves with significant wave height up to 0.25m.

Considering the 0.25m significant wave height limitation, a 1:5 scale will be used (allowing a 1.25m wave representation). This is preferable as it allows for a reasonable pancake size which is necessary to provide sufficient buoyancy for the electronics (and for the weight of the electronics to be reduced relative to the size of the pancake).

Table A.1: Scaling of experiment

Experiment Variable	Original Size Range (m)	1:5 Downscale
Ice Pancake Diameter	2.1-4.3	0.42-0.86
Ice Pancake Thickness	0.05-0.20	0.010-0.040
Significant Wave Height	1-3	0.2-0.6

The SHARC-i experimental setup is shown below. The pancake will be tethered in the wave tank to prevent significant drift. Preliminary tests can be done to determine whether the wave transport is sufficient to justify the tether as the forces of the tether will change the dynamics of the pancake. The electronics will be housed in a waterproof container in the centre of the pancake, with the IMUs as close to the centre of the pancake as possible.

The following preliminary experimental inputs are considered as a starting point for the experiment

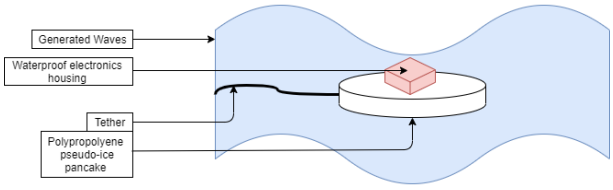

Figure A.1: The SHARC-i buoy in experimental configuration

in Table A.2. The use of multiple inputs will allow for a control analysis of the buoy and will provide a more comprehensive dataset for analysis. The inputs are based on the MIZ characteristics and the experiment outlined by Bennetts & Williams (2015).

The following assumptions are made:

1. The tank depth (1m in the CSIR Lab) is sufficient (i.e. $kd < 2$) to assume deep ocean assumptions (no refraction)

2. That scaling the waves relative to the size of the floe will yield result that can approximate real world conditions

3. That wave steepness, $ka < 0.08$, allows for linear wave theory (or an n^{th} order Stokes correction) to be used.

The Ursell number can be used to determine whether Linear Wave Theory (LWT) or a Stokes correction of linear wave theory is appropriate.

$$\begin{aligned} N_{Ursell} &= steepness/(relative\,depth)^3 \\ &= (H/L)/(d/L)^2 \\ &= HL^2/d^3 \end{aligned} \tag{A.1}$$

Values > 26 indicate that linear wave theory or a Stokes correction of linear wave theory is appropriate.

Table A.2 has the initial experimental values. Values were calculated to produce wavelengths less than and greater than the pancake sizes. Additionally, the wave steepness values used by (Bennetts & Williams 2015) were used as a guideline. Note: L = Wavelength, k = wavenumber, ka = wave steepness, T = wave period, a = wave amplitude). A deep water dispersion relation was used in the calculations as the relative depth: $kd > 2$. Steepness values$ka > 0.1$ should be considered to produce greater waveheights.

A.0.2 Platform Development

The platform will be built using a rigid plastic with a density similar to that of ice. The chosen plastic is polypropylene (PPL) which is a relatively low cost plastic with a density of $0.91g/cm^3$ which is comparable to the density of ice. A disk shape approximates the elliptical and irregular shapes found in pancake ice fields. The weight of the electronics relative to the buoyancy of the pancake platform is a key consideration.

Using the expression:

$$F_{buoyancy} = -\rho g V$$

Table A.2: Initial experimental inputs

Experiment No.	L(m)	k (1/m)	ka	T (s)	a (mm)
1	0.20	31.42	0.04	0.36	1.27
2	0.20	31.42	0.08	0.36	2.54
3	0.20	31.42	0.1	0.36	3.18
4	0.50	12.57	0.04	0.57	3.18
5	0.50	12.57	0.08	0.57	6.36
6	0.50	12.57	0.1	0.57	7.96
7	1.00	6.28	0.04	0.80	6.37
8	1.00	6.28	0.08	0.80	12.7
9	1.00	6.28	0.1	0.80	15.9
10	1.50	4.19	0.04	0.98	9.55
11	1.50	4.19	0.08	0.98	19.1
12	1.50	4.19	0.1	0.98	23.8
13	2.00	3.14	0.04	1.13	12.7
14	2.00	3.14	0.08	1.13	25.5
15	2.00	3.14	0.1	1.13	31.8

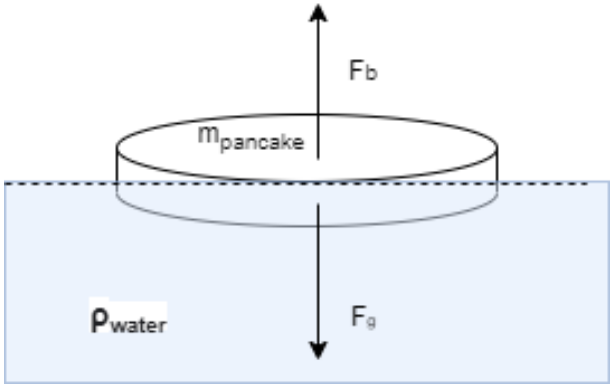

Figure A.2

Table III shows the buoyancy of each of the proposed platforms. Using table A.3 as a guide and assuming 0.5kg of electronics and housing (weight of approx. 5N), the possible platform sizes can be selected. Platforms witrh buoyancy less than 5N will be not be included or be revised to a thicker size.

A.0.3 Electronics Design

The SHARC-i buoy electronics include: Arduino Uno, Draguino LORA transmitter, Invensense ICM20689 6 axis IMU, VectorNav VN100 factory calibrated IMU and an SD CARD interface.

The SHARC-i Buoy has the following requirements:

1. Interface with the VectorNav VN100
2. Interface with the InvenSense ICM20689
3. Process the data on the Arduino locally to produce two acceleration and orientation time series with timestamps

Table A.3: Buoyancy of potential platform sizes

Diameter (m)	Thickness(m)	Volume (m^3)	Buoyancy(N)	Weight(N)
0.40	0.020	0.0025	24	23
0.40	0.040	0.0050	49	45
0.50	0.020	0.0039	38	35
0.50	0.040	0.0079	77	71
0.60	0.020	0.0057	56	51
0.60	0.040	0.011	108	99

4. The identification of local data corruption using checksums and other protocols
5. The generation of appropriate error codes for possible malfunctions
6. The storage of the time series onto a local SD card
7. The transmission of the time series using a Draguino LORA module in real time

Note that the VN100 was not used as results with low cost IMU were sufficient Further note that the LORA module was not used as it proved to be impractical for high frequency data transfer with the chosen MCU.

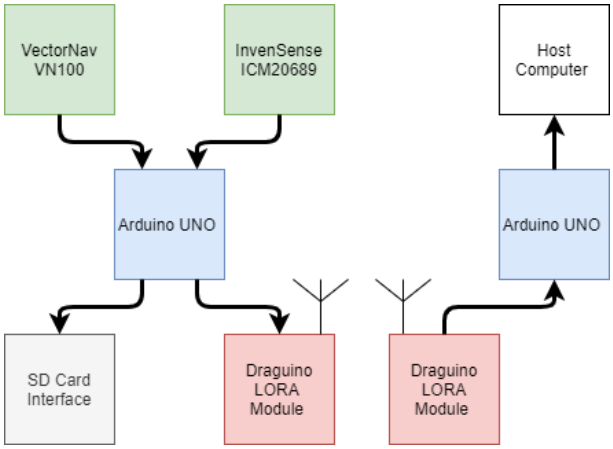

Figure A.3: Block diagram of electronics on SHARC-i Buoy. A local arduino interfaces with two IMUs. It processes the data locally into a timestamped time series format. It then both stores the data locally on an SD and transmits it via a LORA module.

A.0.4 Procedure

The procedure of the experiment will involve the experimental setup described in subsection A.0.1. Following that the wave inputs will be produced for a typical wave sampling period (20-30 minutes). The inputs will be taken from an updated table A.2. During the experiment, the IMU values will be recorded both locally and on a host computer as described in subsection A.0.3. Recording will start from the start of wave generation (so that an step input can be recorded for the control analysis). Additional testing will be done with the electronics removed so that the response of the pancake (measured using the onsite capacitive gauges) without the weight of the measurement equipment can be determined. Initial wave inputs (in the several millimetre range) will be used to determine the ability of the IMU to detect small amplitude range.

A.0.5 Further Development

Significant interest exists in determining the causes of the dissipation of wave energy in pancake ice fields. This leads to possible extensions to the experiments. Suggested mechanisms include: a rough underside causing friction with the water surface and collisions between adjacent pancake floes. Thus, two possible inclusions to the experimentation include:

- The collision of two pancakes to investigate collision events in an acceleration time series
- Comparing a pancake with a rough underside to a smooth underside in acceleration time series.
- The comparison of different ice floe shapes

Appendix B

Wave Tank Testing Results

B.1 ICM20689 validation

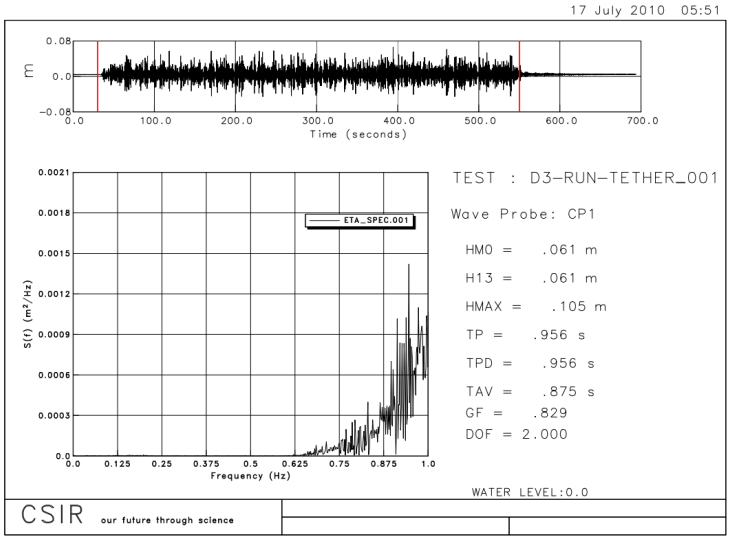

(a) JONSWAP spectrum

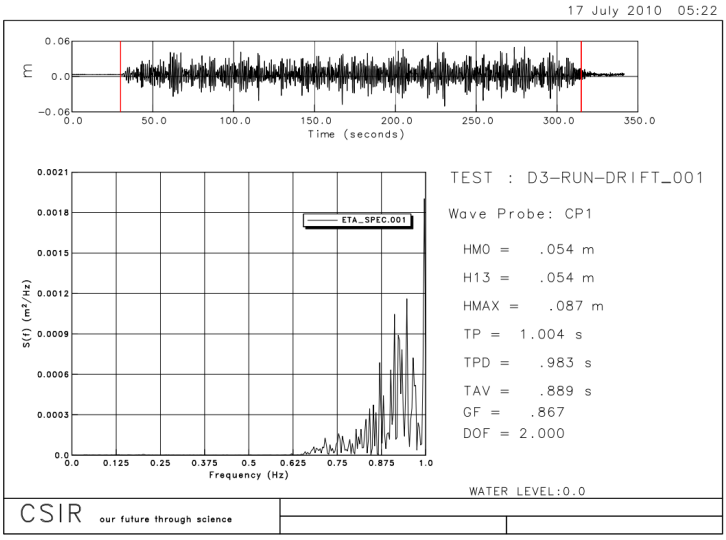

(b) Regular wave spectrum

Figure B.1: Validation datasets for the ICM20689

B.2 ICM20649 validation

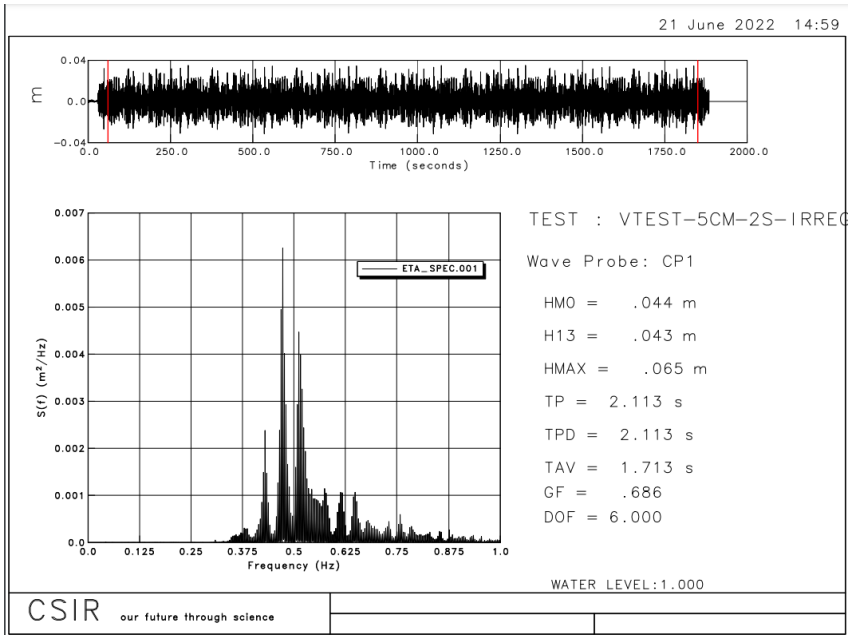

(a) JONSWAP spectrum

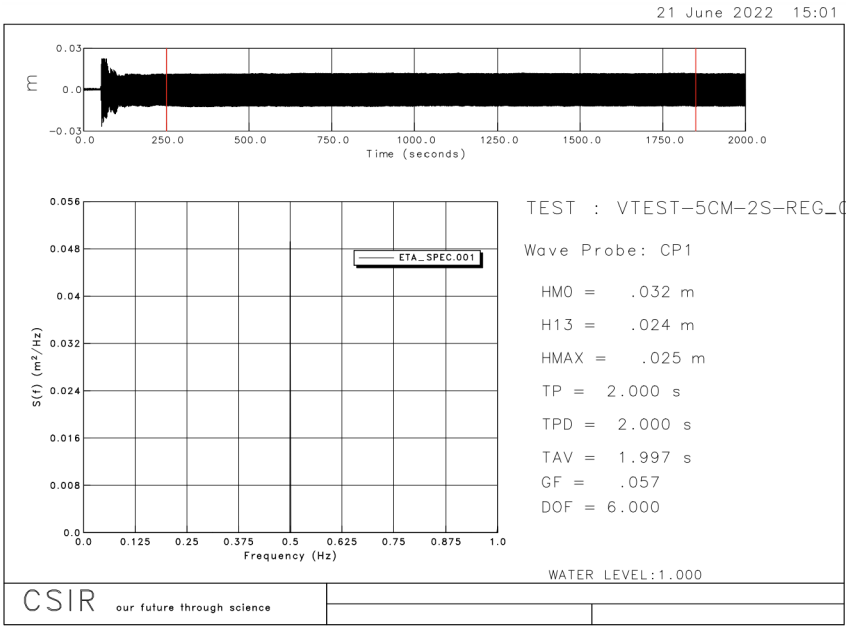

(b) Regular wave spectrum

Figure B.2: Validation datasets for the ICM20649

B.3 Frequency response

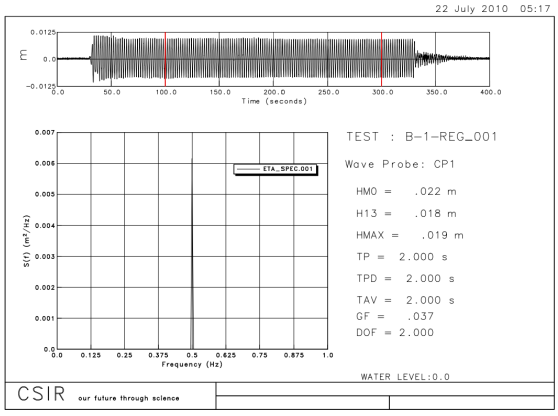

(a) 0.5 Hz

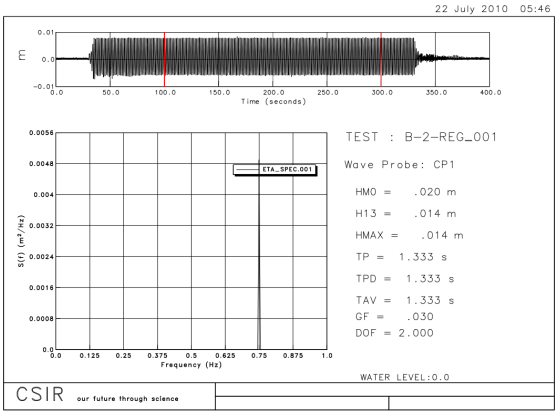

(b) 0.75 Hz

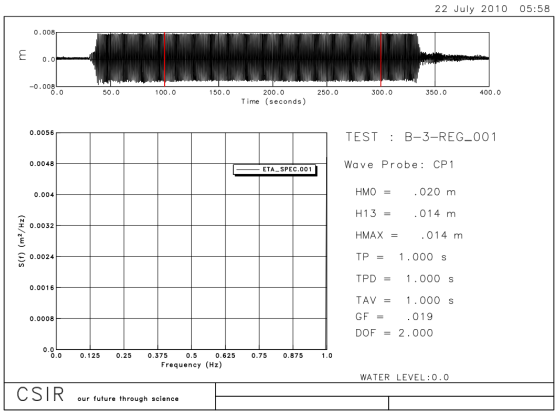

(c) 1.0 Hz

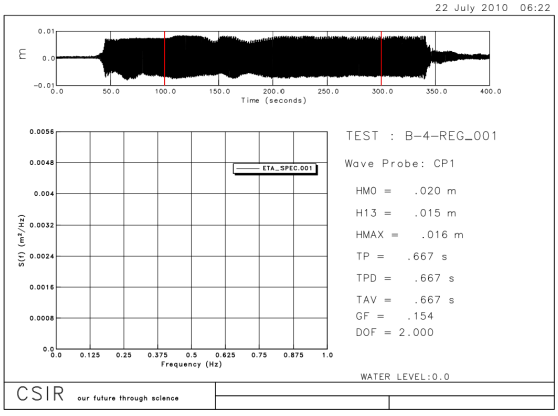

(d) 1.5 Hz

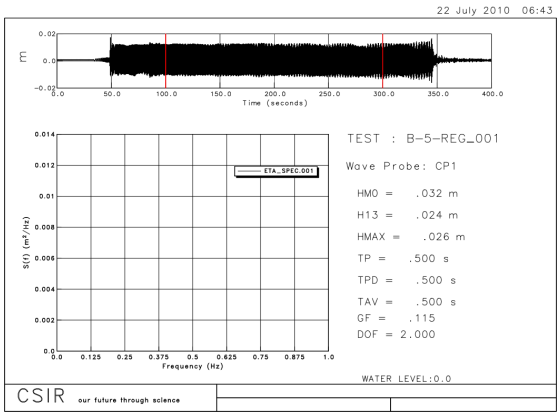

(e) 2.0 Hz

Figure B.3: The time series used to investigate the frequency response of the platform

Appendix C

SHARC buoy V3.0 Requirements and Specifications

C.1 SHARC V3.0 requirements and specifications

C.1.1 User Requirement

Table C.1: Updated user requirements for the SHARC Buoy V3.0

User Requirement	ID	Description
Reliability	UR01	The system shall function reliably over the duration of the deployment or, alternatively, continue operation after the failure of a subsystem
Operational duration	UR02	The system must operate over the full duration of a deployment
Wave measurement	UR03	The system must be able to measure waves and waves-in-ice
Memory storage	UR04	The system must include a memory management system capable of storing sampled data
Wave analysis	UR05	The device must be capable of producing producing summary wave statistics

C.1.2 Functional Requirements

Hardware

Table C.2: Hardware functional requirements for the SHARC V3.0

Functional Requirement ID	Description	User requirement addressed
FR01	The mechanical design of the system will be updated to remove points of failure identified during field testing of the previous system.	UR01
FR02	The system will be functional in extreme cold for extended periods	UR01
FR03	The battery capacity of the system will be sufficiently increased to last for the full operational duration.	UR02
FR04	The system will include an updated IMU able to measure waves-in-ice	UR03
FR05	The system will include sufficient memory to store sampled data.	UR04
FR06	The chosen MCU will have the ability to perform DSP operations on large datasets.	UR05

Firmware

Functional Requirement ID	Description	User requirement addressed
FR07	The system will retain data after a mode of failure	UR01
FR08	The system will be able to recover from a failure mode	UR01
FR09	The system will sample an IMU at a sufficient frequency to measure wave activity	UR03
FR10	The system will store sampled IMU data in an organised file system	UR04
FR11	The system will process stored IMU data in-situ to calculate wave statistics by estimating the PSD of a 30 minute time series	UR05

C.1.3 Specifications

Hardware specifications

Specification	Description	Functional Requirement
HS01	Accelerometer: Measurement range: 4g Sampling rate: >100Hz Operating temperature: [-40°C, 80°C]	FR04, FR02
HS02	Gyroscope: Measurement range: >500 DPS Sampling rate: >100Hz Operating temperature: [-40°C, 80°C]	FR04, FR02
HS03	Power supply: Peak current: >2A Voltage: >7.2 V Capacity: >50Ah Operating temperature: [-40°C, 80°C]	FR03, FR02
HS04	MCU: RAM: >150 kB Onboard FPU Flash: >1 MB Operating temperature: [-40°C, 80°C]	FR06, FR02
HS05	External Memory: Size: >16 GB Operating temperature: [-40°C, 80°C] Supports FATFS	FR05, FR02
HS06	PCB stack to be used in place of wire connectors	FR01

Firmware specifications

Specification	Description	Functional Requirement
FS01	Interface: Type: Inter-integrated circuit (I2C) Mode: Fast mode (400 kHz) Rise/fall time: 300 ns Address length: 7-bits I2C event interrupt enabled I2C error interrupt enabled	FR09
FS02	Interface: Type: SDMMC (SDIO) Clock speed: 32 MHz Bus width: 1 bit	FR09
FS03	Memory management: FATFS Character Encoding: UTF-8 Max filename length: 255 Sector size: 512 bytes	FR10
FS04	DSP Library: CMSIS DSP Software Library Data type: 32-bit floating point operations (float32_t) Target MCU core: M4	FR11
FS05	Hardfault interrupt response: NVIC_SystemReset()	FR08

C.2 Acceptance test protocols

Acceptance Test	Description
ATP01	The SHARC Buoy will log samples on the external memory at 100 Hz for a minimum 12 hour duration in a freezer at -20 Celsius without data corruption.
ATP02	The SHARC Buoy will send ∼100 Iridium packets without a brownout.
ATP03	The SHARC Buoy will retain data after powering off during a sampling interval.
ATP04	The SHARC Buoy will process previously collected IMU datasets locally and return accurate summary wave parameters.
ATP05	Each SHARC buoy will operate with fault for a minimum of 2 sampling sessions before deployment.
ATP06	The SHARC Buoy firmware will automatically reset after a hardfault is intentionally triggered.

Appendix D

Allan Variance Method

D.1 Allan variance testing

D.1.1 Background

The modern standard for IMU modeling is the Allan Variance method. The method is outlined in IEEE Std 952-2020(IEEE 2020). The method is a time series analysis that allows the identification of the source of various noise terms. The Allan Variance noise model is shown in figure D.2.

Allan Variance testing is a form of stochastic modeling. That is, modelling where a white-noise input to a LTI system is used to determine the transfer function from the power spectrum of the output (or alternatively output time series). An alternative to stochastic modelling is dynamic modelling which determines input-output relationship of a system by exciting it with known deterministic inputs. Dynamic gyro models only include scale factor, axis misalignment and bias. Thus the stochastic model allows for a better characterisation of the random drift behaviour of an IMU as the underlying noise processes are well understood, allowing a stochastic model to parameterize a series of canonical transfer functions(IEEE 2020).

The two standard methods for stochastic modelling are:

1. Power Spectral Density (PSD) Analysis (frequency domain)
2. Allan Variance Analysis (time domain)

The Allan Variance method is the most easy to implement of the two methods. It has the added benefit of being more easy for non-experts to understand (useful for in-field testing and deployments by non-experts)(El-Sheimy et al. 2008). It must be noted that the Allan Variance analysis does not allow for a unique characterisation of certain types of noise at the high and low ends of the frequency spectrum. Thus, an Allan Variance test will form a good initial analysis. For a more complete model, a PSD analysis should also be performed.

D.1.2 Theory

The Allan Variance is defined as (note that it can be defined by both angle/postion and rate)(IEEE 2020):

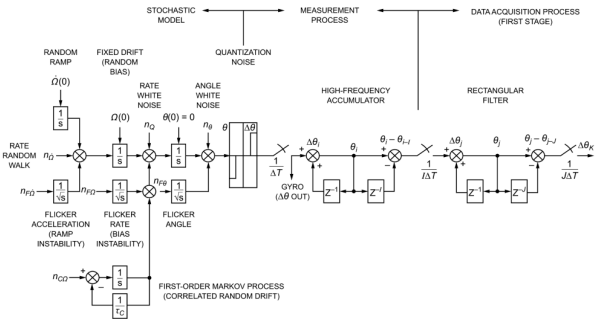

Figure D.1: Block diagram of the stochastic model characterising the random drift behavior of an instrument.

$$\begin{aligned}\sigma^2(\tau) &= \frac{1}{2} < (\bar{\Omega}_{k+m} - \bar{\Omega}_k)^2 > \\ &= \frac{1}{2\tau^2} < (\theta_{k+2m} - 2\theta_{k+m} + \theta_k)^2 >\end{aligned} \tag{D.1}$$

Where $\theta(t)$ is the angle/position, Ω_k is the angular rate/velocity and τ is the sample time. <> denotes the ensemble average.

The Allan Variance can now be estimated as:

$$\sigma^2(\tau) = \frac{1}{2\tau^2(N-2M)} \sum_{k=1}^{N-2M} (\theta_{k+2m} - 2\theta_{k+m} + \theta_k)^2 \tag{D.2}$$

Where N is the number of samples, m is the number samples in the average and k is the discrete time sampling instance.

For a full description of Allan Variance analysis see IEEE (2020) Annex C. For a description of the implementation of the method to create a plot and derive noise values see: Freescale Semiconductor (2015).

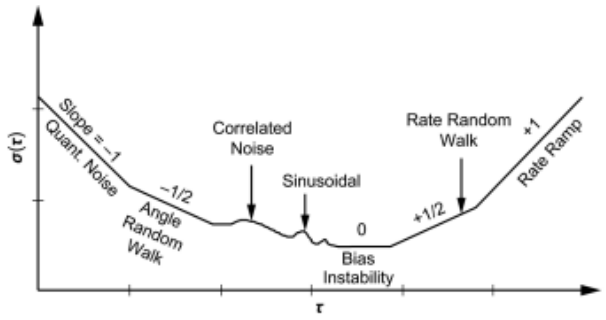

Figure D.2: The general form of the output of an Allan Variance time series. Different noise types have different slopes in the time series.

Appendix E

Deployment Procedure

The procedure for deployment of each buoy was as follows:

1. Before deployment, each buoy was assembled and tested on board the ship in the Electronics Laboratory to ensure correct operation. A new battery pack was fitted and a formatted SD-card was installed.

2. The buoy was placed in a stand on the deck 5 helideck for several hours to check the communication and GPS systems. This step was important for checking the functioning of the buoys prior to on-ice deployment.

3. All deployments were conducted from the personnel basket suspended from one of the starboard bow cranes. Three personnel were in the basket, with the buoy stand laid down in a horizontal position with the feet spikes facing outwards. The buoy itself was kept safely in the centre of the basket until deployment.

4. The buoy system was placed on ice by hand by first placing the stand as close to the centre of the selected pancake as possible.

5. The buoy enclosure was then lowered into the holder on the stand.

6. Finally, the personnel basket was lifted from the ice as soon as the buoy was deployed.

(a) Pre-deployment **(b)** Deployment **(c)** Deployed SHARC Buoy

Figure E.1: Deployment procedure for SHARC Buoys on SCALE Winter Cruise 2022.

Appendix F

Iridium Packet Structure

The following is the packet structure for the Iridium transmissions on the SHARC V3.0. For deployment there were two firmware versions deployed. V1.0 was a drifter that sent GPS coordinates via Iridium whilst logging high frequency IMU data locally for a potential retrieval. V2.0 sent both wave and GPS data. The structure of each of the transmissions is shown the tables below.

Table F.1: Structure of Iridium packet for wave drifter (V2)

Bit	0	1	2	3	4	5	6	7
Byte 0 Byte 1 Byte ... Byte 29	DRIFTBUFFER (V2)							
Byte 30	Empty Space							
Byte 31 Byte 32 Byte ... Byte 64	WAVEBUFFER (V2)							
Byte 65	Empty Space							
Byte 66 Byte 67 Byte ... Byte 94	DRIFTBUFFER (V1)							

Table F.2: Structure of Iridium packet for drifter (V1)

Bit	0	1	2	3	4	5	6	7
Byte 0 Byte 1 Byte ... Byte 38	DRIFTBUFFER (V1)							
Byte 39	Empty Space							
Byte 40 Byte 41 Byte ... Byte 77	DRIFTBUFFER (V1)							

Table F.3: Structure of Iridium packet for drift measurement (V2)

Bit	0	1	2	3	4	5	6	7
Byte 0	ID							
Byte 1 Byte 2 Byte 3 Byte 4	Epoch Time (uint32_t)							
Byte 5 Byte 6 Byte 7 Byte 8	Latitude (float)							
Byte 9 Byte 10 Byte 11 Byte 12	Longitude (float)							
Byte 13	HDOP Digit (int)							
Byte 14	HDOP Precision (int)							
Byte 15	VDOP Digit (int)							
Byte 16	VDOP Precision (int)							
Byte 17	PDOP Digit (int)							
Byte 18	PDOP Precision (int)							
Byte 19	No. Satellites (int)				Fix Type (int)			
Byte 20 Byte 21 Byte 22 Byte 23	Environmental Temperature (int_32)							
Byte 24 Byte 25 Byte 26 Byte 27 Byte 28	Atmospheric Pressure (int_32)							
Byte 29	0xd (End of packet character)							

Table F.4: Structure of Iridium packet for wave measurement (V2)

Bit	0	1	2	3	4	5	6	7
Byte 0	ID							
Byte 1 **Byte 2** **Byte 3** **Byte 4**	Hm0: Significant Wave Height (float32_t)							
Byte 5 **Byte 6** **Byte 7** **Byte 8**	Hrms: Root Mean Square Wave Height (float32_t)							
Byte 9 **Byte 10** **Byte 11** **Byte 12**	T0: Mean Zero Crossing Period (float32_t)							
Byte 13 **Byte 14** **Byte 15** **Byte 16**	Tm01: Mean Spectral Wave Period (float32_t)							
Byte 17 **Byte 18** **Byte 19** **Byte 20**	Tp: Peak Wave Period (float32_t)							
Byte 21 **Byte 22** **Byte 23** **Byte 24**	M0: 0th Spectral Moment (float32_t)							
Byte 25 **Byte 26** **Byte 27** **Byte 28**	M1: 1st Spectral Moment (float32_t)							
Byte 29 **Byte 30** **Byte 31** **Byte 32**	M2: 2nd Spectral Moment (float32_t)							
Byte 33	0xd (End of packet character)							

Table F.5: Structure of Iridium packet for drift measurement (V1)

Bit	0	1	2	3	4	5	6	7
Byte 0	ID							
Byte 1 Byte 2 Byte 3 Byte 4	Epoch Time (uint32_t)							
Byte 5 Byte 6 Byte 7 Byte 8	Latitude (float)							
Byte 9 Byte 10 Byte 11 Byte 12	Longitude (float)							
Byte 13	HDOP Digit (int)							
Byte 14	HDOP Precision (int)							
Byte 15	VDOP Digit (int)							
Byte 16	VDOP Precision (int)							
Byte 17	PDOP Digit (int)							
Byte 18	PDOP Precision (int)							
Byte 19	No. Satellites (int)				Fix Type (int)			
Byte 20 Byte 21 Byte 22 Byte 23	Environmental Temperature (int_32)							
Byte 24 Byte 25 Byte 26 Byte 27 Byte 28	Atmospheric Pressure (int_32)							
Byte 29	0xd (End of packet character)							

Bibliography

Alari, V., Björkqvist, J. V., Kaldvee, V., Mölder, K., Rikka, S., Kask-Korb, A., Vahter, K., Pärt, S., Vidjajev, N. & Tõnisson, H. (2022), 'LainePoiss®—A lightweight and ice-resistant wave buoy', *Journal of Atmospheric and Oceanic Technology* **39**, 573–594.

Alberello, A., Bennetts, L. G., Onorato, M., Vichi, M., MacHutchon, K., Eayrs, C., Ntamba, B. N., Benetazzo, A., Bergamasco, F., Nelli, F., Pattani, R., Clarke, H., Tersigni, I. & Toffoli, A. (2022), 'Three-dimensional imaging of waves and floes in the marginal ice zone during a cyclone', *Nature Communications* **13**.

Alberello, A., Onorato, M., Bennetts, L., Vichi, M., Eayrs, C., Machutchon, K. & Toffoli, A. (2019), 'Brief communication: Pancake ice floe size distribution during the winter expansion of the Antarctic marginal ice zone', *Cryosphere* **13**, 41–48.

Ardhuin, F., Otero, M., Merrifield, S., Grouazel, A. & Terrill, E. (2020), 'Ice breakup controls dissipation of wind waves across southern ocean sea ice', *Geophysical Research Letters* **47**.

Ardhuin, F., Stopa, J., Chapron, B., Collard, F., Smith, M., Thomson, J., Doble, M., Blomquist, B., Persson, O., Collins, C. O. & Wadhams, P. (2017), 'Measuring ocean waves in sea ice using SAR imagery: A quasi-deterministic approach evaluated with Sentinel-1 and in situ data', *Remote Sensing of Environment* **189**, 211–222.

ARM (2022), 'CMSIS DSP software library'.
URL: *https://www.keil.com/pack/doc/CMSIS/DSP/html/index.html*

ATP Electronics (2017), ATP SD/SDHC/SDXC card industrial grade, Technical Report v1.1 202206, ATP.

Barnes, D. K. (2015), 'Antarctic sea ice losses drive gains in benthic carbon drawdown', *Current Biology* **25**, R789–R790.

Bender, I. C., Guinasso, J. L., Walpert, J. N. & Howden, S. D. (2010), 'A comparison of methods for determining significant wave heights-applied to a 3-m discus buoy during hurricane katrina', *Journal of Atmospheric and Oceanic Technology* **27**, 1012–1028.

Bennetts, L. G. & Williams, T. D. (2015), 'Water wave transmission by an array of floating discs', *Proceedings of the Royal Society A: Mathematical, Physical and Engineering Sciences* **471**.

Bishop, G. & Welch, G. (2001), *An Introduction to the Kalman Filter*, Association for Computing Machinery.
URL: *http://www.cs.unc.edu/ {welch,gb}*

Brouwer, J., Fraser, A. D., Murphy, D. J., Wongpan, P., Alberello, A., Kohout, A., Horvat, C., Wotherspoon, S., Massom, R. A., Cartwright, J. & Williams, G. D. (2022), 'Altimetric observation of wave attenuation through the antarctic marginal ice zone using icesat-2', *Cryosphere* **16**, 2325–2353.

ChaN (2023), 'Fatfs - generic fat filesystem module'.
URL: *http://elm-chan.org/fsw/ff/00index_e.html*

Chao, H., Coopmans, C., Di, L. & Chen, Y. (2010), A comparative evaluation of low-cost imus for unmanned autonomous systems, *in* '2010 IEEE International Conference on Multisensor Fusion and Integration for Intelligent Systems', pp. 211–216.

Collins, C. O., Blomquist, B., Persson, O., Lund, B., Rogers, W. E., Thomson, J., Wang, D., Smith, M., Doble, M., Wadhams, P., Kohout, A., Fairall, C. & Graber, H. C. (2017), 'Doppler correction of wave frequency spectra measured by underway vessels', *Journal of Atmospheric and Oceanic Technology* **34**, 429–436.

Crocker, G. & Wadhams, P. (1989), 'Breakup of antarctic fast ice', *Cold Regions Science and Technology* **17**(1), 61–76.
URL: *https://www.sciencedirect.com/science/article/pii/S0165232X89800163*

Dai, M., Shen, H. H., Hopkins, M. A. & Ackley, S. F. (2004), 'Wave rafting and the equilibrium pancake ice cover thickness', *Journal of Geophysical Research: Oceans* **109**.

Doble, M. J. & Bidlot, J. R. (2013), 'Wave buoy measurements at the antarctic sea ice edge compared with an enhanced ecmwf wam: Progress towards global waves-in-ice modelling', *Ocean Modelling* **70**, 166–173.

Doble, M. J., Wilkinson, J. P., Valcic, L., Robst, J., Tait, A., Preston, M., Bidlot, J. R., Hwang, B., Maksym, T. & Wadhams, P. (2017), 'Robust wavebuoys for the marginal ice zone: Experiences from a large persistent array in the beaufort sea', *Elementa* **5**.

Earle, M. D. (1996), Nondirectional and directional wave data analysis procedures, Technical report, National Oceanic and Atmospheric Administration.

El-Sheimy, N., Hou, H. & Niu, X. (2008), 'Analysis and modeling of inertial sensors using allan variance', *IEEE Transactions on Instrumentation and Measurement* **57**, 140–149.

Evans, D. V. & Davies, T. V. (1968), Wave–ice interaction, Technical report, Davidson Laborartory, Stevenson Institute of Technology.

Falnes, J. (2002), *Ocean Waves and Oscillating Systems*, Cambridge University Press.

Fogg, G. E. (2000), 'The Royal Society and the Antarctic', *Notes and Records of the Royal Society* **54**, 85–98.

Fossen, T. I. (2011), *Handbook of marine craft hydrodynamics and motion control*, Wiley.

Freescale Semiconductor (2015), Allan variance: Noise analysis for gyroscopes, Technical Report AN5087 Rev. 0, Freescale Semiconductor.

Gade, K. (2016), 'The seven ways to find heading', *Journal of Navigation* **69**, 955–970.

Greenhill, A. G. (1887), 'Wave motion in hydrodynamics', *Source: American Journal of Mathematics* **9**, 97–112.

Grotmaack, R. & Meylan, M. H. (2006), 'Wave forcing of small floating bodies', *Journal of Waterway, Port, Coastal, and Ocean Engineering* **132**, 192–198.

Herbers, T. H., Jessen, P. F., Janssen, T. T., Colbert, D. B. & MacMahan, J. H. (2012), 'Observing ocean surface waves with gps-tracked buoys', *Journal of Atmospheric and Oceanic Technology* **29**, 944–959.

Holthuijsen, L. H. (2007), *Waves in oceanic and coastal waters*, Vol. 9780521860284, Cambridge University Press.

Hošeková, L., Malila, M. P., Rogers, W. E., Roach, L. A., Eidam, E., Rainville, L., Kumar, N. & Thomson, J. (2020), 'Attenuation of ocean surface waves in pancake and frazil sea ice along the coast of the chukchi sea', *Journal of Geophysical Research: Oceans* **125**.

IEEE (2020), IEEE Standard for Specifying and Testing Single-Axis Interferometric Fiber Optic Gyros, Standard, Institute of Electrical and Electronic Engineers, 3 Park Avenue, New York, NY 10016-5997, USA.

InvenSense (2021*a*), Icm-20649, Technical Report DS-000192, TDK. Rev 1.1.

InvenSense (2021*b*), Icm-20689, Technical Report DS-000143, TDK.

Iridium (2014), Isu at command reference, Technical Report MAN0009 Version 5, Iridium.

Jacobson, J. (2021), Robust firmware design for a novel, low-cost autonomous platform for the antarctic marginal ice zone in the southern ocean, Master's thesis, University of Cape Town. **URL:** *https://open.uct.ac.za/handle/11427/35788*

Journée, J. M. J. & Massie, W. W. (2001), *Offshore Hydromechanics First Edition*.

Kennicutt, M. C., Chown, S. L., Cassano, J. J., Liggett, D., Peck, L. S., Massom, R., Rintoul, S. R., Storey, J., Vaughan, D. G., Wilson, T. J., Allison, I., Ayton, J., Badhe, R., Baeseman, J., Barrett, P. J., Bell, R. E., Bertler, N., Bo, S., Brandt, A., Bromwich, D., Cary, S. C., Clark, M. S., Convey, P., Costa, E. S., Cowan, D., Deconto, R., Dunbar, R., Elfring, C., Escutia, C., Francis, J., Fricker, H. A., Fukuchi, M., Gilbert, N., Gutt, J., Havermans, C., Hik, D., Hosie, G., Jones, C., Kim, Y. D., Maho, Y. L., Lee, S. H., Leppe, M., Leitchenkov, G., Li, X., Lipenkov, V., Lochte, K., López-Martínez, J., Lüdecke, C., Lyons, W., Marenssi, S., Miller, H., Morozova, P., Naish, T., Nayak, S., Ravindra, R., Retamales, J., Ricci, C. A., Rogan-Finnemore, M., Ropert-Coudert, Y., Samah, A. A., Sanson, L., Scambos, T., Schloss, I. R., Shiraishi, K., Siegert, M. J., SimÃes, J. C., Storey, B., Sparrow, M. D., Wall, D. H., Walsh, J. C., Wilson, G., Winther, J. G., Xavier, J. C., Yang, H. & Sutherland, W. J. (2015), 'A roadmap for antarctic and southern ocean science for the next two decades and beyond', *Antarctic Science* **27**, 3–18.

Kennicutt, M. C., Kim, Y. D., Rogan-Finnemore, M., Anandakrishnan, S., Chown, S. L., Colwell, S., Cowan, D., Escutia, C., Frenot, Y., Hall, J., Liggett, D., McDonald, A. J., Nixdorf, U., Siegert, M. J., Storey, J., Wåhlin, A., Weatherwax, A., Wilson, G. S., Wilson, T., Wooding, R., Ackley, S., Biebow, N., Blankenship, D., Bo, S., Baeseman, J., Cárdenas, C. A., Cassano, J., Danhong, C., Dañobeitia, J., Francis, J., Guldahl, J., Hashida, G., Corbalán, L. J., Klepikov, A., Lee, J., Leppe, M., Lijun, F., López-Martinez, J., Memolli, M., Motoyoshi, Y., Bueno, R. M., Negrete, J., Cárdenes, M. A., Silva, M. P., Ramos-Garcia, S., Sala, H., Shin, H., Shijie, X., Shiraishi, K., Stockings, T., Trotter, S., Vaughan, D. G., Menezes, J. V. D. U. D., Vlasich, V., Weijia, Q., Winther, J. G., Miller, H., Rintoul, S. & Yang, H. (2016), 'Delivering 21st century antarctic and southern ocean science', *Antarctic Science* **28**, 407–423.

Kohout, A. L., Penrose, B., Penrose, S. & Williams, M. J. (2015), 'A device for measuring wave-induced motion of ice floes in the antarctic marginal ice zone', *Annals of Glaciology* **56**, 415–424.

Kohout, A. L., Smith, M., Roach, L. A., Williams, G., Montiel, F. & Williams, M. J. (2020), 'Observations of exponential wave attenuation in antarctic sea ice during the pipers campaign', *Annals of Glaciology* **61**, 196–209.

Kohout, A. L., Williams, M. J., Dean, S. M. & Meylan, M. H. (2014), 'Storm-induced sea-ice breakup and the implications for ice extent', *Nature* **509**, 604–607.

Lang, N. (1987), The empirical determination of a noise function for ndbc buoys with strapped-down accelerometers, *in* 'Oceans Conference Record (IEEE)', IEEE, pp. 225–228.

Lee, B. M. C. & Thomson, J. (2017), 'An autonomous approach to observing the seasonal ice zone in the western arctic', *Oceanography* **30**, 56–68.
URL: *http://apl.*

Lee, C. M., Cole, S., Doble, M., Freitag, L., Hwang, P., Jayne, S., Jeffries, M., Krishfield, R., Maksym, T., Maslowski, W., Owens, B., Posey, P., Rainville, L., Shaw, B., Stanton, T., Thomson, J., Timmermans, M.-L., Toole, J., Wadhams, P., Wilkinson, J. & Zhang, J. (2012), Marginal ice zone (miz) program: Science and experiment plan, Technical Report APL-UW 1201.

Lethaby, N. (2013), 'Why use a real-time operating system in mcu applications'.
URL: *www.ti.com/medical*

Lone, T. E. (2020), Navigation techniques for underwater vehicles in polar regions, Master's thesis, Norwegian University of Science and Technology.

Longuet-Higgins, M. S. (1986), 'Eulerian and lagrangian aspects of surface waves', *Journal of Fluid Mechanics* **173**, 683–707.

Ludescher, J., Yuan, N. & Bunde, A. (2019), 'Detecting the statistical significance of the trends in the antarctic sea ice extent: an indication for a turning point', *Climate Dynamics* **53**, 237–244.

Maksym, T. (2019), 'Arctic and antarctic sea ice change: Contrasts, commonalities, and causes', *Annu. Rev. Mar. Sci* **11**, 187–213.
URL: *https://doi.org/10.1146/annurev-marine-010816-*

Maksym, T., Stammerjohn, S. E., Ackley, S. & Massom, R. (2012), 'Antarctic sea ice: A polar opposite?', *Oceanography (Washington, D.C.)* **25**(3), 140–151.

Mankins, J. C. (1995), Technology readiness levels, Technical report, NASA.

Massom, R. A., Scambos, T. A., Bennetts, L. G., Reid, P., Squire, V. A. & Stammerjohn, S. E. (2018), 'Antarctic ice shelf disintegration triggered by sea ice loss and ocean swell', *Nature (London)* **558**(7710), 383–389.

Meylan, M. H., Bennetts, L. G. & Kohout, A. L. (2014), 'In situ measurements and analysis of ocean waves in the antarctic marginal ice zone', *Geophysical Research Letters* **41**, 5046–5051.

Meylan, M. H., Bennetts, L. G., Mosig, J. E., Rogers, W. E., Doble, M. J. & Peter, M. A. (2018), 'Dispersion relations, power laws, and energy loss for waves in the marginal ice zone', *Journal of Geophysical Research: Oceans* **123**, 3322–3335.

Minamoto (2022), Er34615m specification, Technical report, Minamoto.

Mosig, J. E., Montiel, F. & Squire, V. A. (2015), 'Comparison of viscoelastic-type models for ocean wave attenuation in ice-covered seas', *Journal of Geophysical Research: Oceans* **120**, 6072–6090.

NASA Jet Propulsion Laboratory (1997), 'South polar projection of earth'.
URL: *https://www.jpl.nasa.gov/images/pia00729-south-polar-projection-of-earth*

Newman, J. N. (1977), *Marine Hydrodynamics*, The MIT Press.

Pés, V. M. (2013), Applicability and limitations of the swash model to predict wave overtopping, Master's thesis, Barcelona School of Civil Engineering, Technical University of Delft.
URL: *https://upcommons.upc.edu/handle/2099.1/20373*

Rabault, J. (2022), 'Tracking arctic ice: An inexpensive sensor package gets data back despite harsh conditions; tracking arctic ice: An inexpensive sensor package gets data back despite harsh conditions', *IEEE Spectrum* **59**.

Rabault, J., Nose, T., Hope, G., Müller, M., Øyvind Breivik, Voermans, J., Hole, L. R., Bohlinger, P., Waseda, T., Kodaira, T., Katsuno, T., Johnson, M., Sutherland, G., Johanson, M., Christensen, K. H., Garbo, A., Jensen, A., Gundersen, O., Marchenko, A. & Babanin, A. (2022), 'Openmetbuoy-v2021: An easy-to-build, affordable, customizable, open-source instrument for oceanographic measurements of drift and waves in sea ice and the open ocean', *Geosciences (Switzerland)* **12**.

Rabault, J., Sutherland, G., Gundersen, O., Jensen, A., Marchenko, A. & Øyvind Breivik (2019), 'An open source, versatile, affordable waves in ice instrument for scientific measurements in the polar regions'.
URL: *http://arxiv.org/abs/1901.02410*

Rabault, J., Sutherland, G., Gundersen, O., Jensen, A., Marchenko, A. & Øyvind Breivik (2020), 'An open source, versatile, affordable waves in ice instrument for scientific measurements in the polar regions', *Cold Regions Science and Technology* **170**.

Rabault, J., Sutherland, G., Ward, B., Christensen, K. H., Halsne, T. & Jensen, A. (2016), 'Measurements of waves in landfast ice using inertial motion units', *IEEE Transactions on Geoscience and Remote Sensing* **54**, 6399–6408.

Raghukumar, K., Chang, G., Spada, F., Jones, C., Janssen, T. & Gans, A. (2019), 'Performance characteristics of "spotter,"' a newly developed real-time wave measurement buoy', *Journal of Atmospheric and Oceanic Technology* **36**, 1127–1141.

Roach, L. A., Bitz, C. M., Horvat, C. & Dean, S. M. (2019), 'Advances in modeling interactions between sea ice and ocean surface waves', *Journal of Advances in Modeling Earth Systems* **11**, 4167–4181.

Roach, L. A., Smith, M. M. & Dean, S. M. (2018), 'Quantifying growth of pancake sea ice floes using images from drifting buoys', *Journal of Geophysical Research: Oceans* **123**, 2851–2866.

Rochling (2021), Polystone® p homopolymer, Technical report, Röchling Industrial SE Co. KG.

Rogers, W. E., Thomson, J., Shen, H. H., Doble, M. J., Wadhams, P. & Cheng, S. (2016), 'Dissipation of wind waves by pancake and frazil ice in the autumn beaufort sea', *Journal of Geophysical Research: Oceans* **121**, 7991–8007.

Rottier, P. J. (1992), 'Floe pair interaction event rates in the marginal ice zone', *Journal of Geophysical Research: Oceans* **97**, 9391–9400.

Serreze, M. C. & Meier, W. N. (2019), 'The arctic's sea ice cover: trends, variability, predictability, and comparisons to the antarctic', *Annals of the New York Academy of Sciences* **1436**, 36–53.

Shen, H. H., Ackley, S. F. & Hopkins, M. A. (2001), 'A conceptual model for pancake-ice formation in a wave field', *Annals of Glaciology* **33**, 361–367.

Shen, H. H., Hibler, W. D. & Lepparanta, M. (1987), 'The role of floe collisions in sea ice rheology', *Journal of Geophysical Research* **92**, 7085–7096.

Smith, M. & Thomson, J. (2020), 'Pancake sea ice kinematics and dynamics using shipboard stereo video', *Annals of Glaciology* **61**, 1–11.

Solomon, M. O. (1991), Psd computations using welch's method, Technical Report SAND91-1533, Sandia National Laboratories.

Squire, V. A. (2018), 'A fresh look at how ocean waves and sea ice interact', *Philosophical Transactions of the Royal Society A: Mathematical, Physical and Engineering Sciences* **376**.

Squire, V. A. (2020), 'Ocean wave interactions with sea ice: A reappraisal', *Annual review of fluid mechanics* **52**(1), 37–60.

ST Microelectronics (2017), Lsm6dsl, Technical Report 028475, ST Microelectronics. Rev. 7.

STMicoelectronics (2020), Stm32l4r5xx stm32l4r7xx stm32l4r9xx, Technical Report DS12023 Rev 5, STMicoelectronics.

STMicoelectronics (2023), Stm32 nucleo-144 boards (mb1137), Technical Report UM1974 Rev 9, STMicoelectronics.

STMicroelectronics (2019), Stm32l476xx, Technical Report DS10198 Rev 8, STMicoelectronics.

Stopa, J. E., Ardhuin, F., Thomson, J., Smith, M. M., Kohout, A., Doble, M. & Wadhams, P. (2018), 'Wave attenuation through an arctic marginal ice Zone on 12 October 2015: 1. Measurement of wave spectra and ice features from Sentinel 1A', *Journal of Geophysical Research: Oceans* **123**, 3619–3634.

Strong, C., Foster, D., Cherkaev, E., Eisenman, I. & Golden, K. M. (2017), 'On the definition of marginal ice zone width', *Journal of Atmospheric and Oceanic Technology* **34**.

Tedaldi, D., Pretto, A. & Menegatti, E. (2014), A robust and easy to implement method for imu calibration without external equipments, *in* 'Proceedings - IEEE International Conference on Robotics and Automation', Institute of Electrical and Electronics Engineers Inc., pp. 3042–3049.

Thomas, D. N. & Dieckmann, G. S. (2003), *Sea Ice: An Introduction to its Physics, Chemistry, Biology and Geology*, Wiley-Blackwell.

Thomson, J. (2022), 'Wave propagation in the marginal ice zone: connections and feedback mechanisms within the air-ice-ocean system', *Philosophical Transactions of the Royal Society A: Mathematical, Physical and Engineering Sciences* **380**.

Thomson, J., Ackley, S., Girard-Ardhuin, F., Ardhuin, F., Babanin, A., Boutin, G., Brozena, J., Cheng, S., Collins, C., Doble, M., Fairall, C., Guest, P., Gebhardt, C., Gemmrich, J., Graber, H. C., Holt, B., Lehner, S., Lund, B., Meylan, M. H., Maksym, T., Montiel, F., Perrie, W., Persson, O., Rainville, L., Rogers, W. E., Shen, H., Shen, H., Squire, V., Stammerjohn, S., Stopa, J., Smith, M. M., Sutherland, P. & Wadhams, P. (2018), 'Overview of the arctic sea state and boundary layer physics program', *Journal of Geophysical Research: Oceans* **123**, 8674–8687.

Thomson, J., Hošeková, L., Meylan, M. H., Kohout, A. L. & Kumar, N. (2021), 'Spurious rollover of wave attenuation rates in sea ice caused by noise in field measurements', *Journal of Geophysical Research: Oceans* **126**.

Thomson, R. E. & William, E. J. (2014), *Data Analysis Methods in Physical Ocenaography*, 3 edn, Elsevier.

Timco, G. W. & Frederking, R. M. W. (1996), 'A review of sea ice density', *Cold Regions Science and Technology* **24**, 1–6.

Toffoli, A., Bennetts, L. G., Meylan, M. H., Cavaliere, C., Alberello, A., Elsnab, J. & Monty, J. P. (2015), 'Sea ice floes dissipate the energy of steep ocean waves', *Geophysical Research Letters* **42**, 8547–8554.

Topper, M. B. R. (2013), Semantics of spectral density for ocean waves, Technical report. Version 1b.
URL: *https://www.researchgate.net/publication/242337289*

Tucker, M. J. & Pitt, E. G. (2001), *Waves in Ocean Engineering*, Vol. 5, 1 edn, Elsevier.

Turner, J., Guarino, M. V., Arnatt, J., Jena, B., Marshall, G. J., Phillips, T., Bajish, C. C., Clem, K., Wang, Z., Andersson, T., Murphy, E. J. & Cavanagh, R. (2020), 'Recent decrease of summer sea ice in the weddell sea, antarctica', *Geophysical Research Letters* **47**.

ublox (2022), Neo-m9n-00b, Technical Report UBX-19014285 Rev 6, ublox.

VectorNav (2020), Vn-100 imu/ahrs, Technical report. Version 12-0016-R2.

Vichi, M. (2022), 'An indicator of sea ice variability for the antarctic marginal ice zone', *Cryosphere* **16**, 4087–4106.

Vichi, M., Eayrs, C., Alberello, A., Bekker, A., Bennetts, L., Holland, D., de Jong, E., Joubert, W., MacHutchon, K., Messori, G., Mojica, J. F., Onorato, M., Saunders, C., Skatulla, S. & Toffoli, A. (2019), 'Effects of an explosive polar cyclone crossing the antarctic marginal ice zone', *Geophysical Research Letters* **46**, 5948–5958.

Wadhams, P. (1986), The seasonal ice zone, *in* 'The Geophysics of Sea Ice', Springer, pp. 825–991.

Wadhams, P., Lange, M. A. & Ackley, S. F. (1987), 'The ice thickness distribution across the atlantic sector of the antarctic ocean in midwinter', *Journal of Geophysical Research: Oceans* **92**, 14535–14552.

Wadhams, P., Squire, V. A., Goodman, D. J., Cowan, A. M. & Moore, S. C. (1988), 'The attenuation rates of ocean waves in the marginal ice zone', *Journal of Geophysical Research* **93**, 6799.

Welch, P. D. (1967), 'The use of fast fourier transform for the estimation of power spectra: A method based on time averaging over short, modified periodograms', *IEEE Transactions on Audio and Electroacoustics* **15**, 70–73.

Williams, T. D., Bennetts, L. G., Squire, V. A., Dumont, D. & Bertino, L. (2013), 'Wave-ice interactions in the marginal ice zone. part 1: Theoretical foundations', *Ocean Modelling* **71**, 81–91.

Wright, C. S. & Priestley, R. E. (1922), *Glaciology*, Harrison and Sons.

XSens (2020), Mti user manual, Technical Report MT0605P, XSens. 2020. A.

Yiew, L. J., Bennetts, L. G., Meylan, M. H., French, B. J. & Thomas, G. A. (2016), 'Hydrodynamic responses of a thin floating disk to regular waves', *Ocean Modelling* **97**, 52–64.

Yiew, L. J., Bennetts, L. G., Meylan, M. H., Thomas, G. A. & French, B. J. (2017), 'Wave-induced collisions of thin floating disks', *Physics of Fluids* **29**.

Yue, C. & Shen, H. H. (2021), 'Wave-influenced formation of new ice: Model building and a test case', *Ocean Modelling* **167**.